Magneto-thermal conductivity of perovskite manganite films and exchange-spring coupled superlattices

Dissertation

for the award of the degree

"Doctor rerum naturalium" (Dr. rer. nat.)

of the Georg-August-Universität Göttingen

within the doctoral program for physics

of the Georg-August University School of Science (GAUSS)

submitted by

Vitaly Bruchmann-Bamberg

from Leningrad

Göttingen, 2023

Thesis Advisory Committee

apl. Prof. Dr. Vasily Moshnyaga, I. Physikalisches Institut

Prof. Dr. Christian Jooß, Institut für Materialphysik

Prof. Dr. Stefan Mathias, I. Physikalisches Institut

Examination Board

Reviewer: apl. Prof. Dr. Vasily Moshnyaga, I. Physikalisches Institut

2nd reviewer: Prof. Dr. Christian Jooß, Institut für Materialphysik

Further members of the Examination Board

Prof. Dr. Hans Christian Hofsäss, II. Physikalisches Institut

Prof. Dr. Jasnamol Pezhumkattil Palakkal, Institut für Materialphysik

apl. Prof. Dr. Michael Seibt, IV. Physikalisches Institut

Dr. Daniel Steil, I. Physikalisches Institut

Date of the oral examination: 12.01.2024

Contents

1 Introduction

Fig. 1: Photograph of a perovskite mineral "Dysanalyte" (Nb-bearing), 1.6 × 1.5 × 1.4 cm, Locality: Perovskite Hill, Magnet Cove, Hot Spring County, Arkansas, USA) by Kelly Nash, licensed under CC BY 3.0.

The discovery of the mineral perovskite ($CaTiO_3$, Fig. 1) in 1839 by the German mineralogist Gustav Rose who named it after the Russian count and mineralogist Lev Perovski [1] was the birth hour for a whole material class of fascinating crystals. Since then, any material with a chemical formula ABX_3 is named *perovskite*.

Despite the wide variety of perovskite minerals in natural deposits, a large amount of different synthetic perovskites has been successfully synthesized and even more are proposed to be synthesizable. These compounds possess a wide range of physical properties and intriguing multifunctional effects in fields such as magnetism, electrical conductivity, superconductivity, or optical phenomena like the photovoltaic effect. They also demonstrate promising capabilities for electro- and photocatalysis as well as have remarkable thermal, thermoelectric end mechanical properties [2, 3]. The practical applications of perovskites are

literally endless and versatile. They are used in electrochemical and mechanical sensors and actuators [2, 4], photo-detectors (including scintillators and X-ray detectors) [5] [6], light emitting diodes [7, 8], and lasers [9]. Perovskites can possess high-T_c superconductivity [2, 4] and play a huge role in green and renewable energy technologies within high-efficiency photovoltaics [10, 11], fuel cells [4], photocatalytic [12] or thermoelectric devices [13, 14] being (not always but often) environmentally friendly on top [4, 15].

One prominent family of perovskites are strongly correlated electron systems with interconnected degrees of freedom involving electrons, spins and the lattice. This means that a change in one subsystem induces changes in the others and vice versa. Perovskite manganites (general chemical formula $AMnO_3$, the A-site typically occupied by alkaline or rare earth metals) belong to such a family of strongly correlated oxides. They represent a class of materials which show very strong interconnections between for example magnetic and electronic properties like the so-called *colossal magnetoresistance effect* (CMR), where the electrical resistance can change by several orders of magnitude under an applied magnetic field due to a strong connection of the magnetization to the electron mobility, cf. [16].

Magnetic multilayers and in particular *perpendicular magnetic anisotropy* (PMA) are crucial components in skyrmion research [17] or modern applications such as high-capacity hard disc drives [18]. A magnetic multilayer structure of the so-called spin valve builds a simple magneto-electronic readout device capable of distinguishing between parallel or antiparallel magnetic alignment of a probed magnet[1]. In magnetic memory devices a nanoscopic magnetic domain within a thin film represents a single bit of information. The change of the magnetic easy axis from in-plane (IP) to out-of-plane (OOP) using materials with PMA, such as OOP exchange-spring magnet (ESM) heterostructures [21] allowed for a further increase of the areal density of magnetic recording media [22, 23]. Therefore, defining pathways for achieving PMA in magnetic nanomaterials and multilayer structures is an important field of research both for science and applications.

Another important aspect in various fields of research and applications involving electronics, photovoltaics, thermoelectric generators, engines and aircraft are

[1]The underlying physical principle of *giant magnetoresistance* (GMR) [19, 20] was awarded the Nobel Prize to Albert Fert and Peter Grünberg in 2007.

thermal management and thermal insulation. For example, thermal barrier coatings with ultralow thermal conductivity can be found in applications like car engines, aircraft turbines, spacecraft hulls or rocket exhaust systems involving the use of advanced materials like amorphous or multilayer thin films which allows both for increasing durability and enhancing efficiency [24, 25]. With that, fundamental research on the underlying principles for reducing or actively controlling of thermal conductivity is crucial for future improvement of functional thermal materials.

This work provides pathways of achieving both PMA and ultralow thermal conductivity (the latter additionally controllable by external magnetic fields) in magnetoresistive perovskite manganite thin films and superlattices prepared by the vacuum-free Metalorganic Aerosol Deposition (MAD) technique building a strong fundament for ongoing research and future applications.

Structure of the thesis

Part I deals with the theoretical background behind the physics of perovskites, exchange-spring magnets (ESMs) and thermal conductivity, especially the so-called 3ω thermal conductivity measurement technique for thin films. Chapter 2 introduces the perovskite crystal structure which dictates the electronic and magnetic properties emerging from the ligand crystal field coordination and the structure-related magnetic exchange mechanisms. In Chapter 3, thermal conductivity of solids is introduced with subsequent theoretical description of the 3ω technique.

In Part II, experimental techniques used in this work to prepare and to characterize the samples are introduced. Chapter 4 deals with the growth of oxide thin films by the MAD technique as well as with the microstructuring method of the lithography lift-off of metal line elements needed for the 3ω measurements. In Chapter 5, physical properties characterization methods are described, including the developed 3ω extension for the *Quantum Design Physical Properties Measurement System* for thermal conductivity measurements for a wide temperature range and using high magnetic fields as well as methods for characterization of crystal structure, electrical resistivity and magnetization.

Part III presents the results on (magneto-)thermal conductivity of substrates, capping layers (Chapter 6) and functional thin films and superlattices (Chapter 7 and 8). In Chapter 7, measurements of the strongly interconnected magnetism, electrical resistance and magneto-thermal conductivity of the perovskite lanthanum praseodymium calcium manganite $(La_{0.6}Pr_{0.4})_{0.7}Ca_{0.3}MnO_3$ thin films on different substrates are discussed within the framework of crystal structure distortions. In Chapter 8, the results on perovskite/double perovskite superlattices of lanthanum strontium/lanthanum cobalt manganite $La_{2/3}Sr_{1/3}MnO_3/La_2MnCoO_6$ are presented revealing a PMA spin reorientation and having ultralow thermal conductivity dependent on magnetic spin order/disorder controllable by external magnetic fields. At the end, Chapter 9 summarizes the results along with giving concluding remarks and an outlook.

Part I

Theoretical background

2 Physics of perovskites

As introduced earlier, perovskites are all-round materials that have drawn an enormous scientific interest due to their application versatility and their outstanding physical properties. In this work, the main focus lies on perovskite oxides, especially on perovskite manganite oxides. Manganites belong to a family of strongly correlated electron systems with manganese at the B-cite of the crystal. This chapter deals with the physical properties and consequences resulting from the chemistry and the crystal structure of perovskite manganites as well as the emerging strong and interconnected electronic and magnetic interactions.

2.1 Crystal structure

A scheme of the crystal structure of a perovskite oxide ABO_3 is shown in Fig. 2.1.1 of an exemplary cubic representative: The B-site ion is octahedrally coordinated by six oxygen face centered ligands whereas the A-site ions surround the oxygen octahedron in a body-centered manner. The crystal symmetry of this material

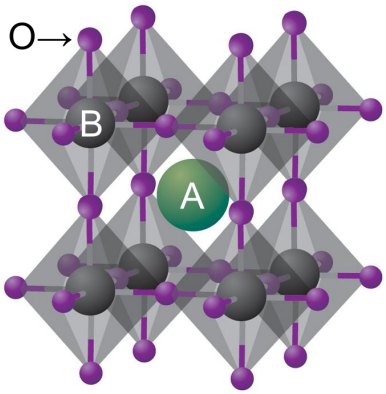

Fig. 2.1.1: Schematic representation of the crystal structure of a cubic perovskite oxide ABO_3. Adapted from [26] with kind permission © 2014 Springer Nature.

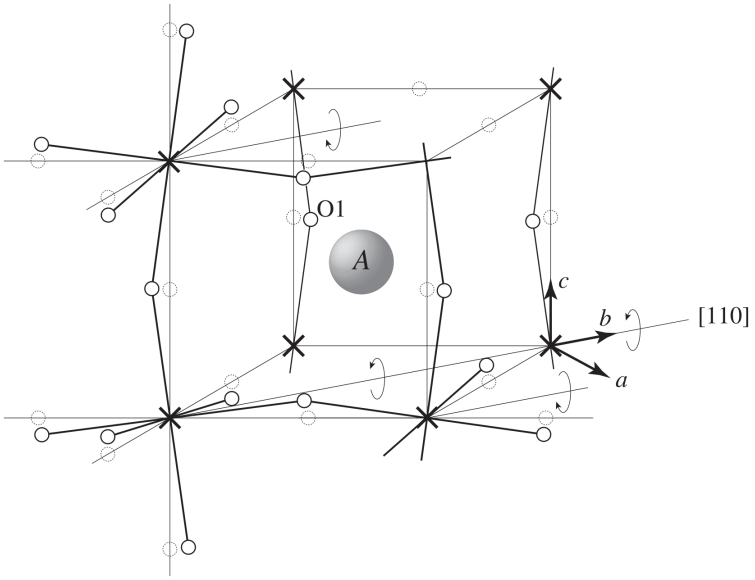

Fig. 2.1.2: Schematic illustration of the BO_6 oxygen octahedral tilting within a perovskite unit cell (oxygen: ○; B-site ion: ×). Here the rotation is performed around the [110] axis. Taken from [16] with kind permission © 2015 The Materials Research Society.

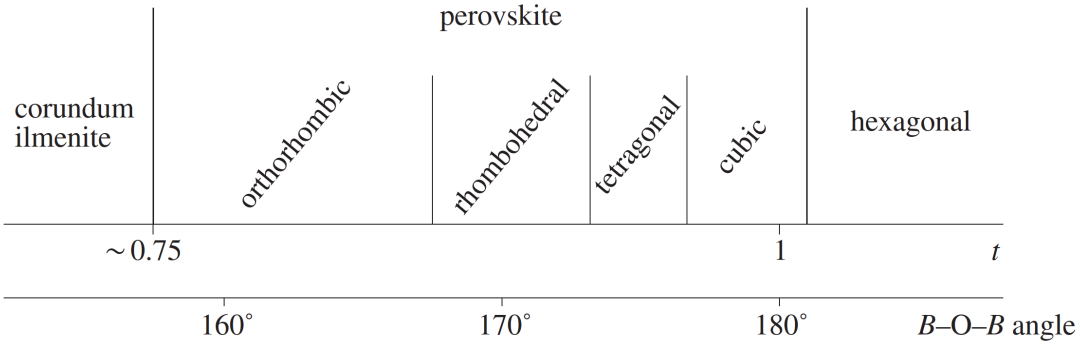

Fig. 2.1.3: Approximate empirical correlation between the crystal structure and the Goldschmidt tolerance factor t and the B-O-B angle according to the oxygen octahedral tilt. Adapted from [16] with kind permission © 2015 The Materials Research Society.

class varies from cubic over rhombohedral to orthorhombic structures, mainly depending on the ratio of ionic radii between the A and B sites and is quantitatively represented by the Goldschmidt tolerance factor t [16, 27]:

$$t = \frac{R_A + R_O}{\sqrt{2}(R_B + R_O)}, \tag{2.1.1}$$

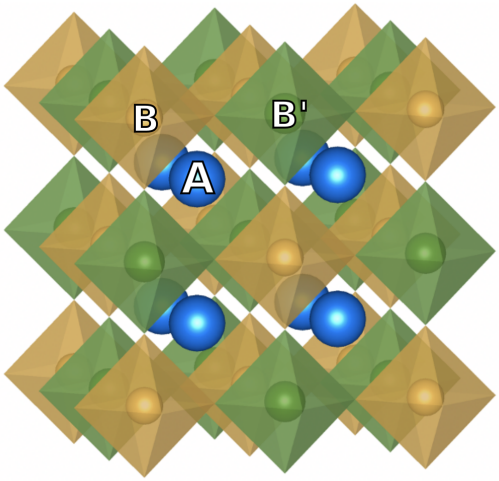

Fig. 2.1.4: Schematic crystal structure of an ordered double perovskite $A_2BB'O_6$, oxygen anions are located at the corners of the octahedra. Adapted with kind permission from [28], by P. Ksoll, licensed under CC BY-NC-ND 4.0.

with the ionic radii R. The perovskite structure is found to form within the range $0.7 \lesssim t \lesssim 1$ with cubic symmetry at $t \approx 1$ and continuously reducing the crystal symmetry at decreasing tolerance factor $t < 1$ [16]. The reduction of crystal symmetry to rhombohedral or orthorhombic structure is usually accompanied by the BO_6 oxygen octahedral tilting as exemplarily shown in the schematic Fig. 2.1.2. The empirical correlation between the crystal structure, tolerance factor and B-O-B tilt angle is sketched in Fig. 2.1.3.

Double perovskites

Another interesting subclass of perovskites, known as *double perovskites* $A_2BB'O_6$, arises from substitutions of the B-site to an equal amount of B' ions, essentially combining two "single" perovskite unit cells with different B-cite ions together, cf. [16]. Typically, the B-cite ions order in a NaCl manner as schematically shown in Fig. 2.1.4. While A-site substitutions often act as dopants and change the B-site valency creating a mixed-valence state that will be discussed later, the B-site substitution in double perovskites intrinsically creates an ordering of cations with different valence states. The latter can further lead to additional and unique functionality.

Double perovskites have been attracting a lot of scientific attention because of a range of superior properties compared to that of single perovskites. These

include low-field magnetoresistance [29], insulating ferromagnetism [30], high-T_C ferromagnetism [31], strong spin-polarization above room temperature [32] and unusual magnetic anisotropy [33].

2.2 Electronic and magnetic properties of perovskite manganites

2.2.1 Crystal field splitting and Jahn-Teller effect

Typically, strongly correlated perovskite oxides consist of rare earth or alkaline earth metals on the A-cite with a transition metal on the B-site [16]. When substituting the A-site ions by an ion A' of another valence, the so-called mixed valence perovskites $A_{1-x}A'_xBO_3$ emerge. In this material class, the valence of the B-site transition metal is then dictated by the fixed A-site valencies Y and Z, creating a mixed valence state $A^Y_{1-x}A'^Z_xB^{6-Y}_{1-x}B^{6-Z}_xO^{2-}_3$.

In order to understand the magnetic exchange mechanisms in manganites described in the next section as well as to elaborate the origin of itinerant electron mobility or charge ordered insulating behavior, the orbital chemistry and the consequences of the orbital overlap of the B-site ion (here manganese) within the octahedral oxygen ligand coordination is a good starting point.

Fig. 2.2.1 presents the break of degeneracy of the energy states within the 3d orbitals and the resulting Jahn-Teller distortion due to octahedral coordination and orbital filling on an exemplary $Mn^{3+}O_6$ octahedron [35]. The octahedral oxygen ligand 2p orbital coordination induces a splitting of the manganese 3d orbitals (right panel of Fig. 2.2.1) into e_g and t_{2g} groups by the crystal field splitting energy Δ_{CF} due to Coulomb repulsion in the range of $\Delta_{CF} \approx 1$ eV for manganites [36][37]. Considering the strong Hund's coupling (typically $J_H \approx 0.8$–0.9 eV per electron resulting in $\Delta E_H \approx 2.4$–2.7 eV for the fourth electron of Mn^{3+}, cf. [16]) and the Pauli principle, the four 3d electrons of the Mn^{3+} distribute with parallel spin alignment to half-filled t_{2g} levels and one high-spin e_g electron. The latter further breaks both e_g and t_{2g} degeneracies through a balance between the elastic and the electrostatic energies driven by the Coulomb repulsion from the ligands stabilizing the elongation of the octahedron in the z-axis accompanied by

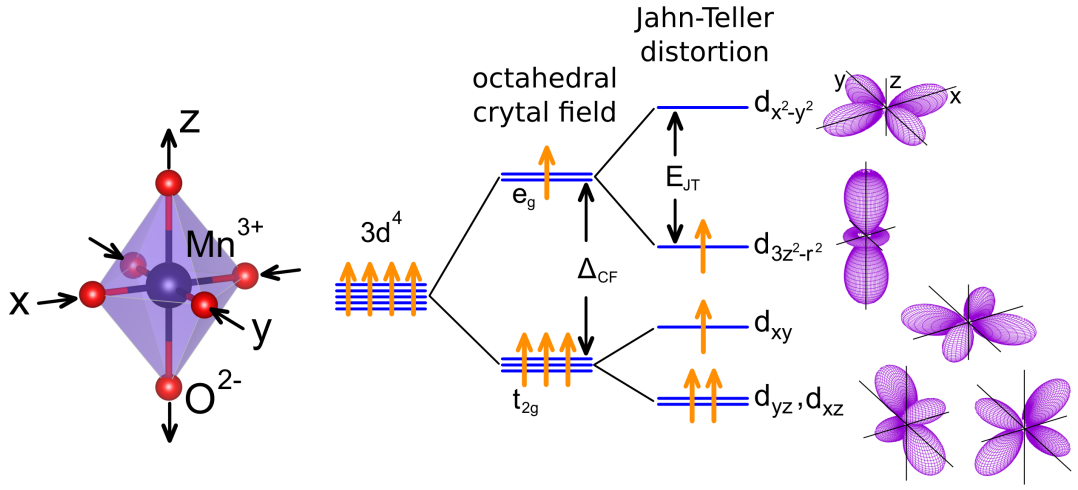

Fig. 2.2.1: Scheme of the Jahn-Teller distortion (left panel, arrows denote the crystal deformation) of a single $Mn^{3+}O_6$ octahedron (Mn: blue sphere, O: red spheres) with a schematic representation of the break of energy level degeneracy (middle panel) of 3d orbitals (right panel) with $3d^4$ occupation which is first lifted by octahedral crystal field splitting Δ_{CF} and further splitted by the Jahn-Teller effect by E_{JT}. The energy axis is not to scale. Taken from [34], by M. Jungbauer, licensed under CC BY-NC-ND 4.0.

the contraction in the x-y-plane when occupying the energetically favorable $d_{3z^2-r^2}$ level. This so-called "Jahn-Teller" distortion of the octahedron is schematically shown in the left panel of Fig. 2.2.1, cf. [16].

2.2.2 Magnetic exchange mechanisms in manganites

Perovskite oxides in general and manganites in specific possess very rich phase diagrams of electronic and magnetic correlations [16]. Depending on doping and temperature, various orbital interactions lead to different electronic and magnetic ground states. In the previous section an orbital interplay was used to explain structural changes, e.g., originating from the Goldschmidt tolerance factor or by the Jahn-Teller effect. In the following, the orbital overlap driven exchange mechanisms which lead to different electron bandwidths and magnetic orders in perovskites are elaborated.

Superexchange

Spontaneous ferromagnetic ordering or the antiferromagnetic spin alignment of a multi-electron solid state system can be explained by quantum mechanical princi-

ples, which include electron-electron Coulomb repulsion, the Pauli principle, and the symmetry of wavefunctions, cf. [38]. Thereby, an electron orbital overlap leads to (direct) exchange interactions breaking the spin degeneracy and determining the magnetic ground state of the system which also can be described by the effective Heisenberg Hamiltonian (cf. [16]):

$$\mathcal{H} = J \sum_{\langle i,j \rangle} \mathbf{S}_i \cdot \mathbf{S}_j, \tag{2.2.1}$$

with the exchange coupling constant J and spin operators $\mathbf{S}_{i,j}$ of the i and j sites (nearest neighbors). The corresponding nature of the interaction is determined by the sign of the coupling constant ($J > 0$ antiferromagnetic, $J < 0$ ferromagnetic interaction; mind the varying definition in literature with a possibility of confusion regarding the sign of J).

The pioneering work on the magnetism of transition metal oxides (TMO) was done by Kramers, Goodenough, Kanamori and Anderson [39–43], who established models for the electronic and magnetic ground states by examining the orbital exchange interactions leading to the (anti-)ferromagnetic spin arrangement in correlated TMO systems like perovskite manganites. The key feature of such indirect magnetic exchange mechanisms is the long-range exchange of the B-cite magnetic ions mediated via the ligand p-orbitals, thus naming it *superexchange* [40].

Let us consider an exemplary case of a TMO with a half-filled conduction band. According to simple band theory (neglecting electron-electron interactions) this system should be metallic. However, if e-e interactions are strong, the on-site Coulomb repulsion U hinders the free movement of electrons and splits the band into Hubbard subbands creating an insulator. Within the Hubbard model (or similar also for charge-transfer systems), the exchange interaction constant J can be expressed in terms of kinetic energy gain of electrons (described by the kinetic energy matrix element t), the on-site Coulomb repulsion U and the charge-transfer energy Δ_{CT}, cf. [16] (minor typing errors in the reference were corrected):

$$J \sim \frac{t_{pd}^4}{\Delta_{\mathrm{CT}}^2 U} = \frac{(t_{dd}^{\mathrm{eff}})^2}{U} \quad \text{(for Mott-Hubbard insulators, } U < \Delta_{\mathrm{CT}}\text{)}, \tag{2.2.2}$$

$$J \sim \frac{t_{pd}^4}{\Delta_{\mathrm{CT}}^2(\Delta_{\mathrm{CT}} + \frac{1}{2}U_{pp})} = \frac{(t_{dd}^{\mathrm{eff}})^2}{\Delta_{\mathrm{CT}} + \frac{1}{2}U_{pp}} \quad \text{(charge-transfer insulators, } U > \Delta_{\mathrm{CT}}\text{)}, \tag{2.2.3}$$

with the effective d-d hopping mediated via p-orbitals denoted as $t_{dd}^{\mathrm{eff}} = t_{pd}^2/\Delta_{\mathrm{CT}}$.[1] Indeed, the resulting exchange constants are in any case positive leading to an antiferromagnetic alignment.

Considering other orbital filling possibilities and taking into account the fundamental phenomena of the Pauli principle, the Coulomb repulsion, and the Hund's coupling, the intrinsic orbital spin distribution within a B_i-O-B_j perovskite oxide chain at a given electronic configuration is dictated by the electronic configuration itself and the orbital polarizations of the B-cite orbitals, cf. [16]. Allowing a "virtual hopping" of the electrons within occupied orbitals to neighboring sites and back, only a specific spin alignment becomes energetically favorable. These circumstances lead to a formation of the following rules also known as Goodenough-Kanamori-Anderson (GKA) rules (here only the case of indirect exchange over the p-orbitals of the ligands is considered, for direct exchange or for further information please refer to the original publications [40–43]), cf. [16]:

1st GKA rule: In a 180° B_i-O-B_j chain, when both cation orbitals overlapping with the same ligand are either empty or occupied (see illustrations in Fig. 2.2.2(a),(b)), the coupling is (strongly) antiferromagnetic. The coupling constant has the form

$$J \sim \frac{t_{pd}^4}{\Delta_{\mathrm{CT}}}\left(\frac{1}{U} + \frac{1}{\Delta_{\mathrm{CT}} + \frac{1}{2}U_{pp}}\right) = (t_{dd}^{\mathrm{eff}})^2\left(\frac{1}{U} + \frac{1}{\Delta_{\mathrm{CT}} + \frac{1}{2}U_{pp}}\right) > 0. \tag{2.2.4}$$

2nd GKA rule: In a 180° B_i-O-B_j chain, when both cation orbitals overlapping with the same ligand are both occupied and empty, the coupling is (weakly) ferromagnetic (Fig. 2.2.2(c)), with

$$J \sim \begin{cases} -\dfrac{(t_{dd}^{\mathrm{eff}})^2}{U} \cdot \dfrac{J_H}{U} < 0 & \text{if } U < \Delta_{\mathrm{CT}}, \\ -\dfrac{(t_{dd}^{\mathrm{eff}})^2}{\Delta_{\mathrm{CT}} + \frac{1}{2}U_{pp}} \cdot \dfrac{J_H}{\Delta_{\mathrm{CT}}} < 0 & \text{if } U > \Delta_{\mathrm{CT}}, \end{cases} \tag{2.2.5}$$

[1] This is exactly the key element of the superexchange.

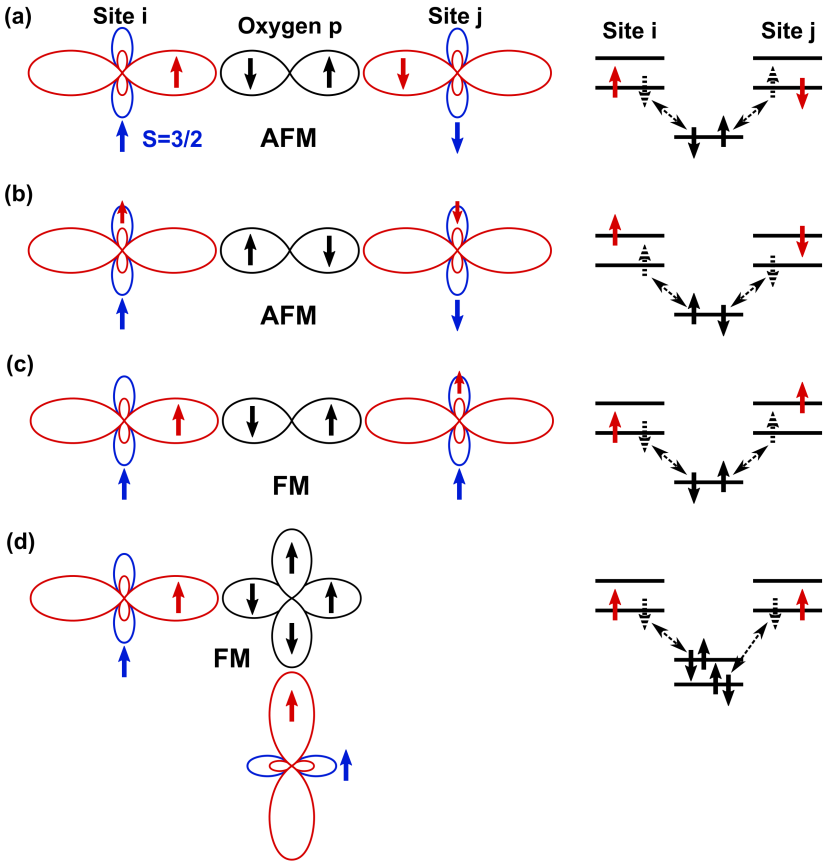

Fig. 2.2.2: Schematic illustration of the Goodenough-Kanamori-Anderson rules. Displayed are the overlapping orbitals within B_i-O-B_j chains of a magnetic transition metal perovskite oxide (left side) and the corresponding electron energy states (right side). The bold arrows represent electron spins, the electron virtual hopping is denoted as dashed black arrows, the dahed red arrows stand for a momentary virtual occupation without charge transfer. Redrawn after [44].

with the Hund's coupling energy J_H of the exchange with localized t_{2g} electrons.

3rd GKA rule: In a 90° B_i-O-B_j chain, if both cation orbitals overlapping with the same ligand are occupied, the coupling is (weakly) ferromagnetic (Fig. 2.2.2(d)), with

$$J \sim -\frac{(t_{dd}^{\text{eff}})^2}{\Delta_{\text{CT}} + \frac{1}{2}U_{pp}} \cdot \frac{J_H^p}{\Delta_{\text{CT}}} < 0, \tag{2.2.6}$$

with the p-site Hund's coupling energy J_H^p.

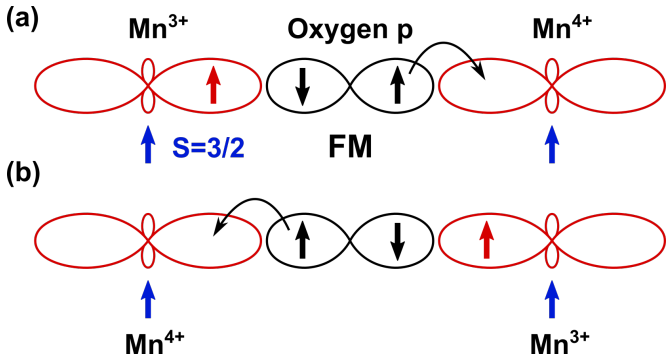

Fig. 2.2.3: Schematic illustration of the double exchange mechanism on the example of the Mn^{3+}-O-Mn^{4+} chain of a mixed-valence perovskite manganite. The charge carrier mobility is possible if the t_{2g} spins (blue arrows) are aligned ferromagnetically. Redrawn after [44].

These rules allow for a fast determination of the magnetic ground state of a magnetic perovskite system according to its electronic occupation and orbital polarization. Still, real systems which can be further affected by structural distortions, strain or other effects that are not included in the model, may deviate from these rules, which are based on assumptions and simplifications like describing only a 1-dimensional behavior.

Double exchange

Similar to superexchange, the so-called *double exchange* (DE) mechanism introduced by Zener [45, 46] and further extended by Anderson and de Gennes [47, 48] involves the same orbital exchange interaction mechanisms with the only difference of the hopping of electrons which becomes non-virtual and allows for charge carrier mobility between the cations. This is only possible if the total energy of the system after the charge transfer remains the same as well as the energy barrier (like the Hund's coupling energy or the Coulomb repulsion in case of superexchange) becomes small compared to the kinetic energy gain, cf. [16, 44]. One possibility to obtain such behavior is to dope a Mott insulator like $La^{3+}Mn^{3+}O_3$ with 3d holes, that is, to create empty Mn e_g states by substituting some of the A-site ions by lower valenced dopants like Sr^{2+}. This leads to the formation of a mixed-valence manganite, here lanthanum strontium manganite $La^{3+}_{(1-x)}Sr^{2+}_{(x)}Mn^{3+}_{(1-x)}Mn^{4+}_{(x)}O_3$ (LSMO).

Fig. 2.2.3 shows the DE mechanism schematically on an example of the Mn^{3+}-O-Mn^{4+} chain as it can be found in LSMO. Due to a strong Hund's coupling, the e_g electron of the Mn^{3+} cation only becomes itinerant if the localized spins of both B-cite ions are ordered ferromagnetically which explains the strong coupling of the ferromagnetism and electron mobility. In addition, this model provides a better understanding of several phenomena of mixed-valence manganites, like magnetoresistance or metal-insulator transitions. Still, in this simple description some open questions remain, for example about the angle dependence of the coupling or phase separation, for which again the Hamiltonian can help. Adding energy terms for itinerant electrons to Eq. (2.2.1) leads to a description of the DE Hamiltonian, cf. [16]:

$$\mathcal{H}_{\mathrm{DE}} = -t \sum_{\langle i,j\rangle,\sigma} c_{i\sigma}^{\dagger} c_{j\sigma} - J_H \sum_i \mathbf{S}_i \cdot c_{i\sigma}^{\dagger} \hat{\boldsymbol{\sigma}} c_{i\sigma} + J \sum_{\langle i,j\rangle} \mathbf{S}_i \cdot \mathbf{S}_j, \tag{2.2.7}$$

with creation and annihilation operators $c_{i\sigma}^{\dagger}$, $c_{i\sigma}$ of itinerant electrons with the intersite hopping element t (kinetic energy gain). The most important term for DE is the middle term of Hund's coupling energy J_H: it describes the energy gain (or loss) of the exchange between the spin $\boldsymbol{\sigma}_i$ of the itinerant e_g electron and the t_{2g} total spin $\mathbf{S}_i$. The last competing term for the (anti-) ferromagnetic interaction of the localized t_{2g} spins was already introduced in the previous section.

One can see that if the Hund's coupling is strong compared to the kinetic energy of the itinerant electron of the bandwidth $W \sim 2zt$ (with the number of next neighbors z), the total energy is minimal if the spin of the itinerant electron $\boldsymbol{\sigma}_i$ is aligned parallel to the spin $\mathbf{S}_i$ of the localized site, cf. [16] (Fig. 2.2.4(a)). However, if the spin of the site to which the itinerant electron is hopping is antiparallel (Fig. 2.2.4(c)), the strong Hund's coupling forbids the transition (or at least strongly reduces its probability). Still, a kinetic energy gain is not only restricted to ferromagnetic arrangement and the nature of the scalar product allows itinerant electrons with a canted (non-collinear) magnetic alignment at some angle θ for a delocalization, but with a reduced bandwidth (Fig. 2.2.4(b)). The angle dependence can be described by an effective hopping constant [47, 48]:

$$t_{\mathrm{eff}} = t \cos\frac{\theta}{2}. \tag{2.2.8}$$

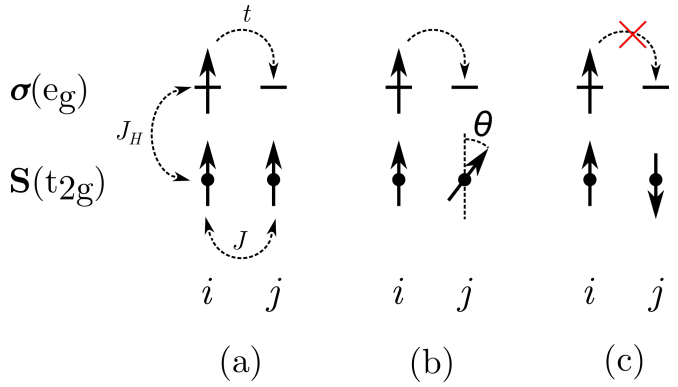

Fig. 2.2.4: Schematic representation of the spin arrangement in a B-O-B chain and the corresponding electron hopping within the double exchange mechanism (Eq. (2.2.7)). The B site orbitals are represented as dots (t_{2g}) and dashes (e_g), the average spin components are represented as arrows. The itinerant e_g electron has a maximum bandwidth (can move freely from site i to j) only if the localized t_{2g} spins are aligned parallel. For a canted state (b) the bandwidth (mobility) is reduced. Large Hund's coupling energy $J_H \gtrapprox t$ prohibits conduction (strongly reduced probability of the transition from i to j) if the alignment is antiparallel (c). Based on [16].

However, such a canted state is usually unstable so that a phase separation sets in with a formation of ferromagnetic and antiferromagnetic domains. This behavior is usually found in colossal magnetoresistive manganites (cf. [16, 49]).

In general, both B-O distances d_{BO} and B-O-B angles $(180° - \theta)$ can affect the bandwidth W due to the change of the orbital overlap, approximated by, cf. [50, 51]:

$$W \approx \frac{\cos(\theta/2)}{d_{\mathrm{BO}}^{3.5}}. \tag{2.2.9}$$

The main outcome of the DE model is the strong interconnection of ferromagnetic alignment and electron mobility in specific mixed-valence manganites like LSMO. The parallel alignment of magnetic moments can be achieved either by undergoing the paramagnetic-ferromagnetic transition below the Curie temperature T_{C} or by applying external magnetic fields that mediates mobility of itinerant electrons within a strongly spin-polarized conduction band.

2.2.3 Metal-insulator transitions

Generally, metal-insulator transitions can occur in various types of materials when varying temperature, pressure or doping, cf. [16]. The underlying principles of localization or mobility of free electrons (or holes) can be characterized in three different ways: using the band theory (when e-e interactions are negligible), through Anderson transitions (in disordered systems) and through Mott transitions (in the case of strong correlations), cf. ibid. The latter was already extensively discussed in the previous sections dealing with orbital-selective description of narrow band localization of t_{2g} electrons providing antiferromagnetic coupling (superexchange) and itinerant e_g electrons mediating ferromagnetic coupling within the DE mechanism. This also leads to the explanation of the magnetic field-induced insulator-metal transition found for example in magnetoresistive mixed-valence manganites.

Colossal magnetoresistance

Since the magnetization of DE manganites is strongly coupled to the electrical conductivity, the latter can be controlled in the paramagnetic state by an external magnetic field due to Zeeman interaction which can align the paramagnetic spins. The latter is facilitated in the vicinity of paramagnetic to ferromagnetic phase transition at the Curie temperature leading to magnetoresistance (MR) values in in the order of $MR = 100\% \cdot [\rho(H) - \rho(0)]/\rho(0) \sim -100\%$ when comparing electrical resistivity ρ with and without applied field H for example of LSMO, $La_{(1-x)}Ca_{(x)}MnO_3$ or $La_{(1-x)}Ba_{(x)}MnO_3$ [52–54].

Phase separated manganites like $(La_{1-y}Pr_y)_{0.67}Ca_{0.33}MnO_3$ (LPCMO) where correlated polarons (a lattice distortion or polarization coupled to a charge) give rise to an additional antiferromagnetic coupling of ferromagnetic domains lead to even larger (thus named "colossal" magnetoresistance CMR) resistivity changes with CMR values of $CMR \sim 10^4 - 10^6\,\%$ [49, 55].

Due to different notations of the CMR/MR with a normalization either to a field-free or an applied-field resistance value and using different sign in literature, here the CMR value shall be denoted as defined in [55]:

$$CMR = -100\% \cdot [\rho(H) - \rho(0)]/\rho(H). \tag{2.2.10}$$

In order to prevent confusion (e.g., a negative magnetoresistance leads to a positive CMR value), when generally speaking about magnetoresistance MR the following standard definition shall be used:

$$MR = 100\% \cdot [\rho(H) - \rho(0)]/\rho(0). \tag{2.2.11}$$

2.2.4 Magnetic anisotropy and orbital polarization

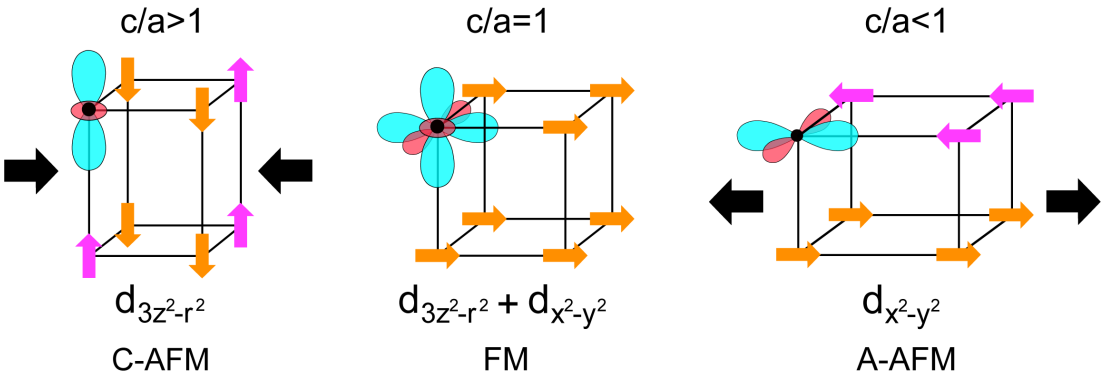

Fig. 2.2.5: Orbital polarization of the e_g orbitals on the example of a $LaMnO_3/SrMnO_3$ system. Compressive strain (left panel) stabilizes the $d_{3z^2\text{-}r^2}$ orbital, whereas tensile strain (right panel) lowers the energy for the $d_{x^2\text{-}y^2}$ orbital. In the unstrained state (middle panel), a linear combination of e_g orbitals (or orbital degeneracy) is stable. Different orbital polarization further leads to a different magnetic ground state (FM/AFM). After [56] [57], taken from [34] by M. Jungbauer, licensed under CC BY-NC-ND 4.0.

Another aspect that needs to be addressed in this thesis is the magnetic, especially perpendicular magnetic anisotropy (PMA).

One of the ways to achieve PMA in manganites is by tuning orbital polarization via epitaxial strain, cf. [56, 57]. Using substrates of a different in-plane lattice constant a_{sub} compared to an epitaxially grown film (a_{film}), either a compressive ($a_{\text{sub}} < a_{\text{film}}$) or tensile ($a_{\text{sub}} > a_{\text{film}}$) strain can be achieved (unstrained configuration is unusual, but still achievable with appropriate buffer layers). Fig. 2.2.5 shows this circumstance of the strain effect on orbital polarization on the example of a $LaMnO_3/SrMnO_3$ system.

Strain dependence of the magnetization anisotropy for LSMO behaves similarly, i.e, a compressive strain (e.g., using $LaAlO_3(100)$ substrates) stabilizes the $d_{3z^2\text{-}r^2}$ orbitals leading to a ferromagnetic PMA [58–60], whereas tensile strain ($SrTiO_3(100)$

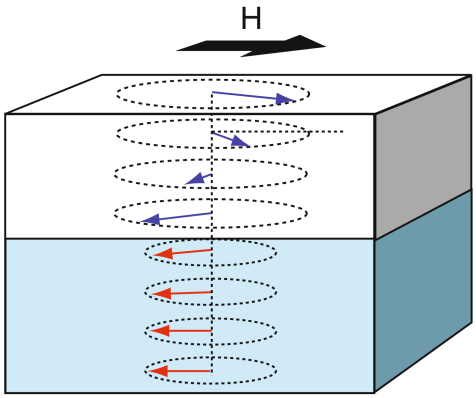

Fig. 2.2.6: Schematic representation of an exchange-spring magnet with bottom hard ferromagnetic layer, top soft layer. The distribution of magnetic moments is represented as arrows. An external magnetic field H creates a twist of the spins within the soft magnetic constituent. Reproduced from [66] with kind permission © 2009 Springer Nature.

substrates) forms an in-plane ferromagnetic anisotropy which also usually follows the direction of the miscut angle terraces of the substrate [61]. Other effects like interfacial charge transfer, superlattice strain or the use of buffer layers can also lead to orbital reconstruction towards preferred occupation of the $d_{3z^2\text{-}r^2}$ orbitals of LSMO enabling PMA [62–64].

In contrast, the double perovskite La_2CoMnO_6 (LMCO) exhibits ferromagnetic PMA when tensile strained (for example on $SrTiO_3(100)$ substrates) due to spin-orbit coupling of Co^{2+} in octahedral environment [33].

Another possibility to obtain PMA in a soft ferromagnet not intrinsically as discussed above but extrinsically is by using magnetic proximity [65] incorporating the material in another magnet exhibiting PMA with a high coercive field. Such composites (either domain/matrix alloy or a superlattice) of soft/hard ferromagnets that are also called *exchange-spring magnets*.

2.2.5 Exchange-spring magnets

Combining materials in a superlattice, that is an alternating array of the constituent thin films, often allows for novel functionality that is not present in the individual materials [67–69]. Magnetic superlattices serve as functional materials with applications in sensing or magnetic storage devises [18]. In this thesis the focus lies on magnetic multilayer systems of the exchange-spring magnets

(ESM). An ESM is formed within a magnetic heterostructure consisting of a soft and a hard magnetic material which are directly magnetically exchange coupled [21, 66, 70, 71]. Such materials usually combine the high coercivity of hard magnets with the high saturation magnetization of soft magnets, an important criterion for permanent magnets. Further, the interplay of different coercive fields and the magnetic coupling at the interfaces allows for a gradual rotation/torsion of the magnetic moments within the soft ferromagnetic constituent towards external fields when not exceeding the coercivity of the hard magnetic counterpart (Fig. 2.2.6), cf. [66].

Further, it is indeed possible to achieve PMA in an ESM system due to the direct exchange of the consisting layers if the hard magnetic counterpart exhibits PMA, cf. [72].

As one of the main objectives of this thesis is the study of thermal conductivity within manganite-based MES, the next chapter deals with the theoretical description of thermal conductivity and its measurement techniques.

3 Thermal conductivity

In this section, an appropriate thermal conductivity measurement technique for thin films in a wide temperature range and allowing the use of high external magnetic fields shall be elaborated. First, a brief theoretical background for thermal conductivity is given. At the end, various techniques for measuring thin film thermal conductivity are briefly introduced and the appropriate technique for use in this work is chosen.

3.1 Theory of thermal conductivity

Thermal conductivity is a fundamental physical property of materials to transport heat from a hot region towards a colder sink until the temperature difference equilibrate. This nature of heat transport is dictated by the fundamental laws of thermodynamics (cf. [73]), with a mathematical description of the macroscopic heat flow that was first introduced by Fourier in far 1822 in his *Théorie Analytique de la Chaleur* (the analytical theory of heat) [74] using observations made earlier by Biot which was groundbreaking for that time giving not only a quantitative mathematical framework for understanding how heat flows through materials (cf. [75, 76]) but also providing a powerful mathematical tool of an approximation of periodic functions to an expansion of infinite superpositions of trigonometric functions originally used in his work for finding solution to the heat equation, but which is today known as the *Fourier series* widely used in nearly every field of science, e.g., in analyzing, processing and modeling of signals (further insights can be found in topical literature, e.g., [77]).

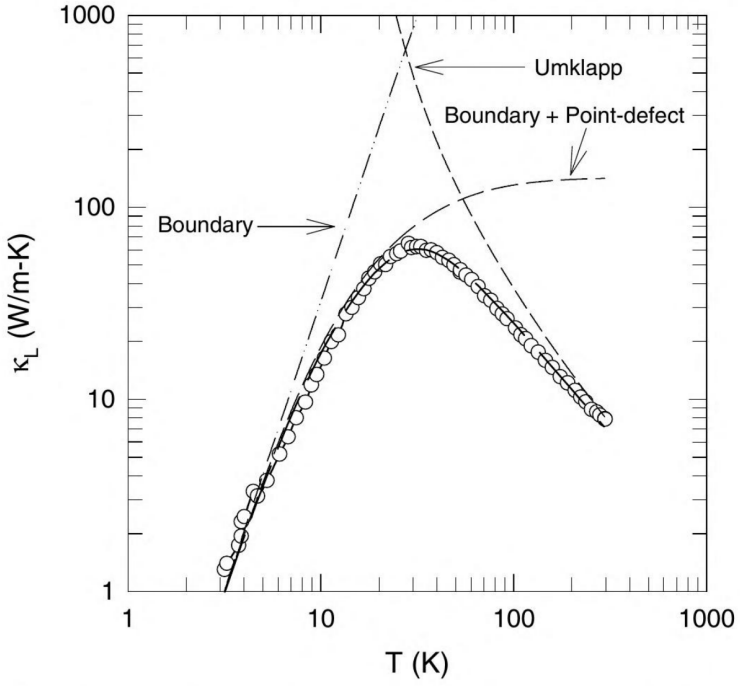

Fig. 3.1.1: Literature data on the temperature dependence of the lattice thermal conductivity κ_{L} of a typical crystalline solid on an example of $CoSb_3$ (points) along with theoretical fits (lines) for different scattering mechanisms. Reproduced from [75] with kind permission © 2004 Springer Nature.

The steady-state heat flow in an isotropic medium can be expressed by the Fourier-Biot equation (cf. [75, 78]):

$$\boldsymbol{q} = -\kappa\vec{\nabla}T, \quad \text{or} \tag{3.1.1}$$

$$\frac{Q}{A} = -\kappa\frac{\partial T}{\partial x} \quad \text{(unidirectional heat flow)}, \tag{3.1.2}$$

with the heat flux $\boldsymbol{q}$, or heat Q per area A, thermal conductivity coefficient κ and temperature field T. The corresponding diffusion equation for the time evolution of the temperature profile is given by the Fourier equation (simplified in 1D):

$$\frac{\partial T}{\partial t} = D\frac{\partial^2 T}{\partial x^2}, \tag{3.1.3}$$

with diffusivity (also called thermometric conductivity) $D = \kappa/(\rho c_p)$, density ρ and specific heat capacity c_p.

In dielectric solids, the heat flow is realized by elastic vibrations of the lattice, which can be described by emerging quanta of the vibrational field called “phonons”.

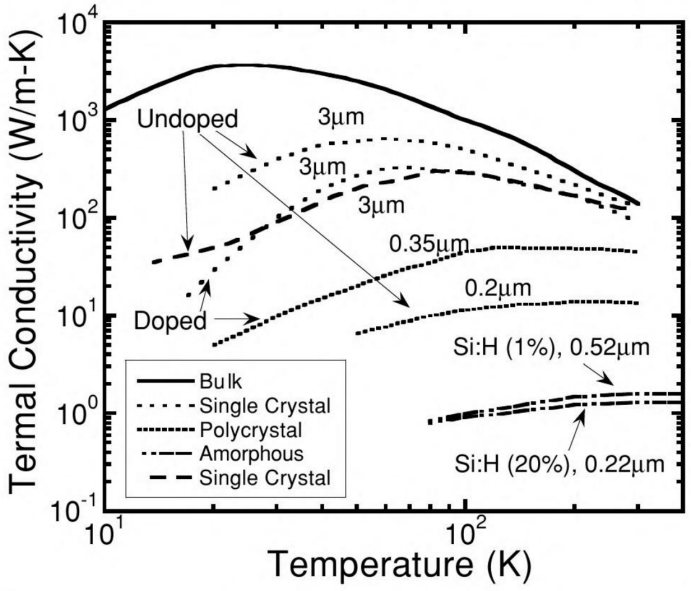

Fig. 3.1.2: Literature data on the impact of the material morphology (denoted in the legend) on the temperature dependence of the lattice thermal conductivity of a solid on an example of silicon. The labels represent the film thicknesses. Reproduced from [75] with kind permission © 2004 Springer Nature.

The lattice vibration waves transporting heat suffer scattering of different types mainly originating from the self-scattering (multi-phonon processes like normal process or Umklapp scattering), crystal non-idealities like impurities or crystal defects as well as boundary scattering given by the dimensions of the material altogether defining a typical temperature dependence of crystalline materials shown in Fig 3.1.1, cf. [75]. The thermal conductivity can be expressed within a kinetic model as a function of total heat capacity C, sound velocity v and phonon mean free path $l = v\tau$ with relaxation time τ (cf. [75]):

$$\kappa = \frac{1}{3} C v l. \tag{3.1.4}$$

Decreasing film thickness, introducing polycrystallinity, doping or amorphization drastically decrease the lattice thermal conductivity κ_{L} by increasing the scattering rates of phonons as exemplarily shown in Fig. 3.1.2, such that the typical thermal conductivity maximum at low temperatures as well as the decrease at high temperatures for crystalline bulk materials vanishes and the dependence becomes monotonically increasing with temperature, cf. [75]. Additional thermal boundary (also known as “Kapitza”) resistances between different materials or

grain boundaries that further decrease thermal conductivity must also be taken into account, especially when reducing dimensions of the sample or dealing with superlattices.

Itinerant electrons additionally contribute to thermal conductivity ($\kappa_{\text{total}} = \kappa_{\text{L}} + \kappa_{\text{e}}$), cf. [75]. The ratio of the electronic thermal conductivity κ_{e} to the electrical conductivity σ is given by the Wiedemann-Franz (WF) law [79]:

$$L_0 = \frac{\kappa_{\text{e}}}{\sigma T}, \tag{3.1.5}$$

with the Lorenz number $L_0 = \pi^2 k_B^2 / 3e^2 \approx 2.4453 \cdot 10^{-8}$ V^2/K^2, Boltzmann constant k_B and electron charge e. This law is typically valid at very high and very low temperatures for a degenerate electron gas, i.e., a metal. At moderate temperatures, the Lorenz number is typically reduced and is additionally affected by defects and impurities, cf. [75].

3.2 Measuring thermal conductivity

The measurement of thermal conductivity of bulk materials is typically done by measuring the temperature gradient within the material at a known heating power and a constant temperature sink, that is, essentially measuring the steady heat flow (known as the steady-state or absolute method, cf. [75]). However, this method gets to its limits when dealing with thin films. The accurate measurement of temperature gradients within several nanometers spatial resolution is challenging. Therefore, other techniques (both using optical or electrical heating/sensing) were established for thermal conductivity measurements of thin films. They typically investigate the dynamic response of the sample to a given amount of applied heat involving either time-domain or frequency-domain responses related to the heat dissipation like temporal temperature equilibration or reflectivity changes (the latter utilizing the temperature dependence of optical constants), cf. [75].

Since optical pump-probe measurement techniques like time-domain thermoreflectance (TTR) usually only use the time evolution of the temporal response without knowing the exact amount of absorbed heat, only the measurement of

the thermal diffusivity D is possible, cf. [75]. The thermal conductivity is then calculated via $\kappa = D\rho c_p$ ex-situ which requires knowledge of parameters for the density ρ and the specific heat capacity c_p. In contrary, electrical techniques like the 3ω method can provide direct measurements of the diffusivity and the thermal conductivity for bulk samples simultaneously and can measure the thermal conductance of nanometer-scale thin films, or even liquids, gases or powders cf. [80–83]. Additionally, the technical aspect of the simplified use of cryostats and superconducting magnets when using electrical measurements instead of implementing them to an optical setup speaks for the use of 3ω method for measurements of thermal conductivity of thin films in a wide temperature range and strong external magnetic fields. Therefore, in this work the implementation of the 3ω method to the cryostat of the commercial setup *Quantum Design Physical Properties Measurement System* (PPMS) armed with a 9T superconducting magnet was elaborated.

3.2.1 The 3ω method

The 3ω method is an electrical technique for measuring thermal conductivity of either bulk or thin films as well as multilayers on a substrate. The technique was originally developed by Cahill [81] and established nowadays to a widely used method for measuring thermal conductivity, especially of nanoscale thin films [80, 82, 84–88] and which can further be used as a sensor in various thermal conductivity or diffusivity related measurements like biofouling thicknesses, flow rates of liquids or surface contacts [89].

The underlying principle of this method is the frequency-domain heat dissipation measurement (via the temperature oscillation) of a patterned heater element on top of a specimen after applying an AC Joule heating current through it (see schematic Fig. 3.2.1). Usually, a metal like Au or Pt is used as a heater due to their linear temperature dependence of electrical resistance in a wide temperature range. The following theoretical description and the setup design are based on topical reviews of the 3ω method [88, 90], and the Cahill's original publication [81].

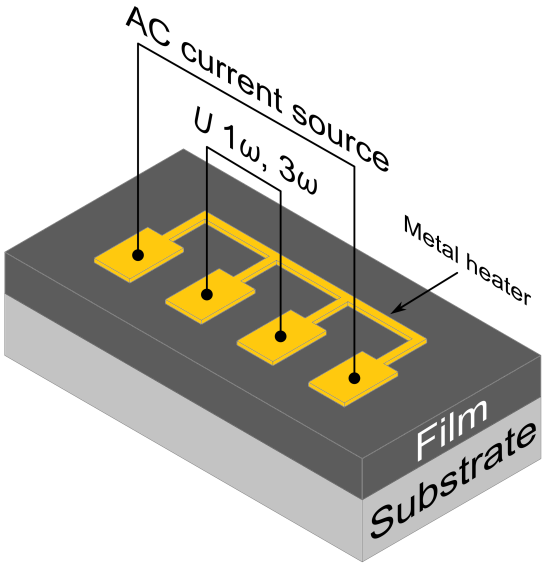

Fig. 3.2.1: Schematic of a patterned metal heater on a specimen for 3ω measurement of thermal conductivity (e.g., of a film on a substrate). Driving an AC heating current creates an Ohmic voltage drop $U_{1\omega}$ along with an additional $U_{3\omega}$ signal due to heat dissipation which are dependent on thermal properties of the sample. Based on [81].

Theoretical description

In the following, complex values are denoted using the underscore " _ ", and expressions of oscillating values are given as RMS values.[1]

The current source $I_{1\omega}$ of angular frequency $\omega = 2\pi f$ creates Joule heating of the metal element (with a linear temperature dependence of resistance) leading to a constant temperature rise along with a temperature oscillation $T(t) = T_{\mathrm{DC}} + T_{2\omega}(t)$, the latter at the doubled (2ω) frequency since the heating is independent of the sign of the current ($P \sim I^2$). Along with the fundamental Ohmic voltage $\underline{U}_{1\omega}$ and the resistance oscillation at 2ω proportional to the temperature oscillation, an additional 3rd harmonic voltage $\underline{U}_{3\omega}$ of the heater line element emerges[2], giving this method the name 3ω. The connection of the 3ω voltage to the temperature oscillation is done using the calibrated value for the temperature coefficient of electrical resistance $\alpha = (1/R_{\mathrm{el}})(\mathrm{d}R_{\mathrm{el}}/\mathrm{d}T)$ of the metal line, altogether leading to:

[1] For example the AC voltage $\underline{U} = U_X + iU_Y$ is expressed as the in-phase $\mathfrak{Re}(\underline{U}) = U_X$ and the out-of-phase $\mathfrak{Im}(\underline{U}) = U_Y$ component with respect to the current oscillation phase.
[2] Due to $\sin(\omega) \cdot \sin(2\omega) \sim \cos(\omega) - \cos(3\omega)$

$$\underline{T} = \frac{2\underline{U}_{3\omega}}{U_{1\omega}\alpha} = \frac{2\underline{U}_{3\omega}}{I_{1\omega}\frac{\mathrm{d}R_{\mathrm{el}}}{\mathrm{d}T}}. \tag{3.2.1}$$

This thermal wave oscillation exponentially decays within the specimen with a thermal penetration depth d_{tpd}:

$$d_{\mathrm{tpd}} = |q|^{-1} = \sqrt{\frac{D}{2\omega}}, \tag{3.2.2}$$

with the thermal wavenumber $q = \sqrt{\frac{i2\omega}{D}}$, thermal diffusivity $D = \kappa/(\varrho c_p)$, density ϱ and specific heat capacity c_p, cf [88].

Both analytical and approximated expressions for the measured complex temperature oscillation $\underline{T}$ of the heater line at a given AC current source can be used for calculating thermal conductivity [81, 91]. The definition of the temperature oscillation as a complex value is due to the fact that the heat oscillation can be phase shifted in relation to the heating current oscillation. This leads to the in-phase and out-of-phase components of temperature oscillation in respect to the AC current phase.

A suitable expression for thin multilayer films used in this thesis is the solution derived by Borca-Tasciuc, Kumar and Chen which is capable of modeling a multilayer system on a finite thickness substrate taking into account the thermal anisotropy of each layer using a two-dimensional heat conduction model, a uniform heat flux boundary condition between the heater and the top layer and neglecting the thermal mass of the heater [91]:

$$\underline{T} = \frac{-p}{\pi l \kappa_{y_1}} \int_0^\infty \frac{1}{A_1 B_1} \frac{\sin^2(b\lambda)}{b^2\lambda^2} \mathrm{d}\lambda, \tag{3.2.3}$$

with the RMS electrical power p, length l and half-width b of the heater element and parameters of a recursive layer definition counting from the top ($i = 1$) to

the bottom layer (substrate, $i = n$):

$$A_{i-1} = \frac{A_i \frac{\kappa_{y_i} B_i}{\kappa_{y_{i-1}} B_{i-1}} - \tanh(\varphi_{i-1})}{1 - A_i \frac{\kappa_{y_i} B_i}{\kappa_{y_{i-1}} B_{i-1}} \tanh(\varphi_{i-1})}, \quad i = 2...n, \tag{3.2.4}$$

$$B_i = \sqrt{\kappa_{xy} \lambda^2 + \frac{i2\omega}{D_{y_i}}}, \tag{3.2.5}$$

$$\varphi = B_i d_i, \quad \kappa_{xy} = \frac{k_x}{k_y}, \tag{3.2.6}$$

with superscripts x (y) defining the in-plane (out-of plane) direction, κ the thermal conductivity, d thickness of the layer, and $\kappa_{xy} = \kappa_x/\kappa_y$ thermal conductivity anisotropy.

The starting parameter for the recursive definition, A_n is chosen according to the substrate thickness and its boundary conditions [91]:

$$A_n = \begin{cases} -\tanh(B_n d_n) & \text{adiabatic} \\ -\frac{1}{\tanh(B_n d_n)} & \text{isothermal,} \end{cases} \tag{3.2.7}$$

which becomes $A_n \approx -1$ for thick enough substrates (semi-infinite approximation $A_n = -1$).

Any additional thermal resistance R_{th}, especially thermal boundary (Kapitza) resistances R_{tbr} and the intrinsic thermal resistance of an isotropic film R_f can be expressed as an additive frequency independent real part term to the total measured temperature oscillation $\underline{T}_{\text{tot}}$ with a normalizing prefactor of the electrical power per heater area [91][87]:

$$\underline{T}_{\text{tot}} = \underline{T} + \frac{p}{2bl} R_{\text{th}}, \tag{3.2.8}$$

$$R_{\text{th}} = R_f(d_f) + R_{\text{tbr}} = \frac{d_f}{\kappa_f} + R_{\text{tbr}}, \tag{3.2.9}$$

with the film thickness d_f and intrinsic thermal conductivity κ_f. This thermal series resistance model is sketched in Fig. 3.2.2 for a thin film on a substrate constellation.

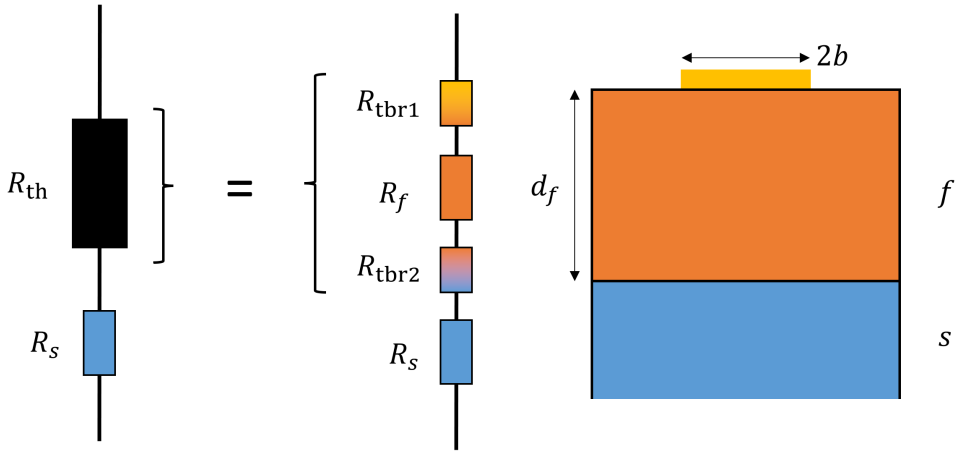

Fig. 3.2.2: Schematic of the series thermal resistance model of a film (f) of thickness d_f on a substrate (s), $2b$ is the metal heater width. The total thermal resistance of the film R_{th} can be expressed as the sum of the thermal boundary resistances $R_{\mathrm{tbr}} = \sum R_{\mathrm{tbr},i}$ as well as the intrinsic thermal resistance of the film $R_f = d_f/\kappa_f$.

Thermal impedance model

Following the analytic solution for the heater line temperature oscillation $\underline{T}$ (Eq. (3.2.3)), Olson, Graham and Chen have derived a slight improvement of the analytical expression for the thermal oscillation $\underline{T}$ connecting it with the thermal impedance $\underline{Z}$ [92]:

$$\underline{T} = \underline{q}\underline{Z}, \tag{3.2.10}$$

with the heat flux $\underline{q}$.

The connection of the surface thermal impedance $\underline{Z}$ to measurable quantities is given by [92]:

$$\underline{Z}(\omega) = -\frac{4R^2bl}{U_{1\omega}^3 \frac{\mathrm{d}R}{\mathrm{d}T}} \underline{U}_{3\omega}(\omega), \tag{3.2.11}$$

with electrical resistance R, the Ohmic voltage drop $U_{1\omega}$, and the temperature dependence of the resistance $\mathrm{d}R/\mathrm{d}T$ of the heater element.

One can extract from Eq. (3.2.11) the proportionality

$$\underline{U}_{3\omega} \propto U_{1\omega}^3 \propto I_{1\omega}^3, \tag{3.2.12}$$

which can be used as a quick benchmark of the setup by measuring the 3ω signal at different driving currents, that should give a linear proportionality when plotting both the real $\mathfrak{Re}(\underline{U}_{3\omega})$ and the imaginary part $\mathfrak{Im}(\underline{U}_{3\omega})$ as a function of the 3$^{\text{rd}}$ power of excitation current $I_{1\omega}^3$, indicating the pure thermal origin of the 3ω signal, cf. [82]. Otherwise, there could be some error in the setup or the used parameters like a too strong current source that adds a non-negligible DC heating, inductive or capacitive coupling within the setup, a power dependent harmonic distortion of the current source, or other issues, cf. [82, 87].

If appropriate (e.g. at high driving frequencies), also the thermal mass of the heater element can be included as additional source of impedance to correct its contribution [92]:

$$\underline{Z}^*(\omega) = \frac{1}{\frac{1}{\underline{Z}(\omega)} + i2\omega d_e \varrho C_e}, \tag{3.2.13}$$

with d_e the heater element thickness and ϱC_e its thermal capacity.

In terms of thermal impedance, the analytical expression of temperature oscillation (3.2.3) becomes a surface impedance $\tilde{\underline{Z}}$ (here the tilde " ˜ " denotes the analytical surface value) as a function of driving frequency ω, which also allows for a better comparison of raw data between different specimens due to included heater geometry and being independent of driving power [92]:

$$\tilde{\underline{Z}}(\omega) = \frac{1}{\pi}\int_{-\infty}^{\infty} \frac{\sin^2\chi}{\chi^2}\tilde{\underline{z}}_N(\chi,\omega)\mathrm{d}\chi. \tag{3.2.14}$$

The analytical expression of the surface impedance $\tilde{\underline{Z}}$ is obtained via integration of the layer transform impedance $\tilde{\underline{z}}$ over the dimensionless transform variable χ with [92]:

$$\tilde{\underline{z}}_n(\chi,\omega) = \frac{b}{\kappa_{y_n}\Phi_n(\chi,\omega)} \frac{\frac{k_{y_n}\Phi_n(\chi,\omega)}{b}\tilde{\underline{z}}_{n-1}(\omega) - \tanh\left(\Phi_n(\chi,\omega)\frac{d_n}{b}\right)}{1 - \frac{k_{y_n}\Phi_n(\chi,\omega)}{b}\tilde{\underline{z}}_{n-1}(\omega)\tanh\left(\Phi_n(\chi,\omega)\frac{d_n}{b}\right)}, \tag{3.2.15}$$

$$\Phi_n(\chi,\omega) = \sqrt{\kappa_{xy}\chi^2 + \frac{i2\omega b^2}{D_{y_n}}},$$

$$n = 2,3,...,N \text{ (layer number)}.$$

Here, the impedance of the bottom (substrate) layer $n = 1$ (mind the reversed iteration compared to the expression (3.2.3) by Borca-Tasciuc et al.) is given by the semi-infinite approximation [92]:

$$\tilde{\underline{z}}_1(\chi,\omega) = \frac{-b}{\kappa_{y_1}\Phi_n(\chi,\omega)}, \tag{3.2.16}$$

but can analogously be extended to an adiabatic or isothermal condition according to Eq. (3.2.7) if needed.

The use of thermal impedance (Eq. (3.2.14)), which is essentially a frequency dependent thermal resistance, also allows for a simple addition of the interfacial thermal boundary resistance $R_{\mathrm{tbr},n}$ as an additive term to the layer impedance [92]:

$$\tilde{\underline{z}}_{n,\mathrm{total}}(\chi,\omega) = \tilde{\underline{z}}_n(\chi,\omega) + R_{\mathrm{tbr},n}. \tag{3.2.17}$$

Part II

Experimental techniques

4 Sample preparation

The following section describes the techniques used to prepare the thin amorphous or crystalline oxide films by the Metalorganic Aerosol Deposition (MAD) technique as well as the microstructuring of metal heater/thermometer structures on top of the samples by optical lithography lift-off.

4.1 Metalorganic Aerosol Deposition

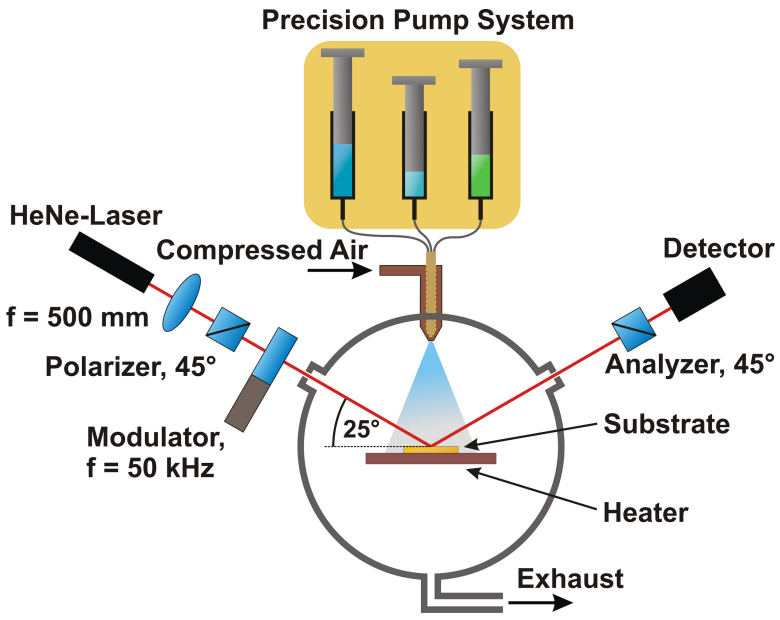

Fig. 4.1.1: Schematic of the metalorganic aerosol deposition technique. The setup consists of a precise syringe pump system feeding a pneumatic nozzle with solved metalorganic precursors which produces an aerosol jet by compressed air. The subsequent thin film growth after a pyrolysis reaction on the heated substrate is monitored by in-situ optical ellipsometry setup using a HeNe-Laser. Taken from [93] with kind permission © 2014 AIP Publishing.

The Metalorganic Aerosol Deposition (MAD) technique is a method for growing thin oxide films or metallic nanoparticles [93–95]. The schematic of the *MAD3* setup used in this work is sketched in Fig. 4.1.1: An aerosol of metalorganic precursors (acetylacetonate metalorganic compounds solved in N,N-dimethylformamide with a concentration of $c = 0.02$ mol/l) is sprayed through a pneumatic nozzle with compressed air on top of a heated substrate (on a doped SiC resistive heater) where after a pyrolysis reaction the metal or the metal oxide is deposited on the substrate surface. The precise dosing of the precursor solution by the precision syringe system *Hi-Tec Zang SyrDos 2* enables accuracy of sub-unit-cell thickness with in-situ growth monitoring by optical ellipsometry. Standard deposition temperature for growth of crystalline films was used in the range of $T_{\mathrm{dep}}^{\mathrm{crystal}} = 900° - 950°\,\mathrm{C}$, whereas a strong reduction of the substrate temperature down to $T_{\mathrm{dep}}^{\mathrm{amorphous}} = 360°\,\mathrm{C}$ leads to a formation of an amorphous phase. The temperature monitoring is done using a two-color pyrometer *METIS M322* by *Sensortherm*. Deposition rate for crystalline films amounted to $v_{\mathrm{dep}}^{\mathrm{crystal}} = 0.1$ nm/s whereas it was $v_{\mathrm{dep}}^{\mathrm{amorphous}} = 0.05$ nm/s for amorphous films.

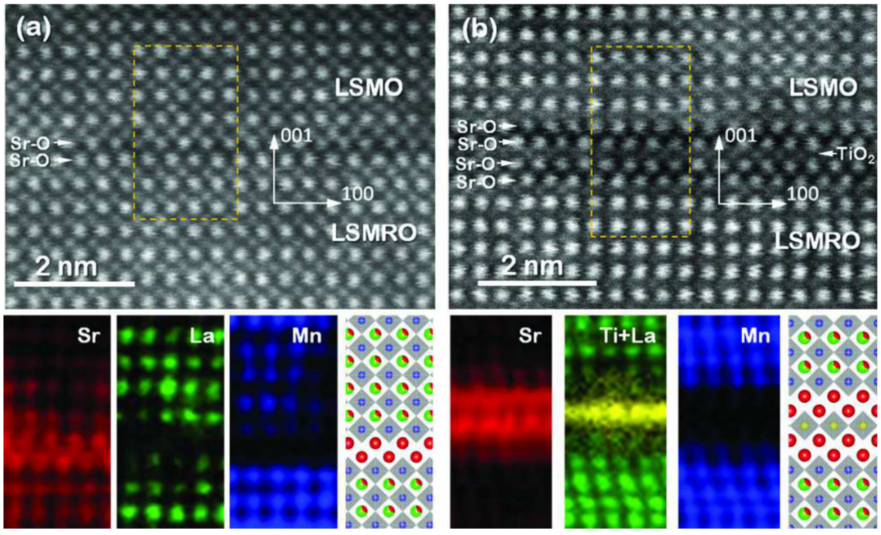

Fig. 4.1.2: A high-resolution scanning transmission electron microscope images of two sample examples grown by MAD demonstrating atomic layer deposition precision of this technique: (a) Top panel shows the high-angle annular dark-field image of the LSMO/RP/LSMRO trilayer on STO(100) substrate, RP being the $(SrO)_2$ Ruddlesden-Popper layer, and LSMRO the Ru-doped LSMO. Bottom panel shows the electron energy loss elemental maps along with a crystal structure model. (b) Figure similar to (a) but with an additional TiO_2 monolayer of the RP-STO barrier between LSMO and LSMRO. Taken from [96] with kind permission © 2016 AIP Publishing.

Figure 4.1.2 demonstrates the capability of the MAD setup for deposition of complex oxides with atomic layer precision allowing epitaxial growth of complex multilayer systems on single crystalline substrates on an example of a spin-valve structure of ferromagnetic metallic LSMO and LSMRO (Ru-doped for higher coercivity) separated by a layer-by-layer grown Ruddlesden-Popper STO grown on STO(100) [96].

4.2 Microstructuring by optical lithography

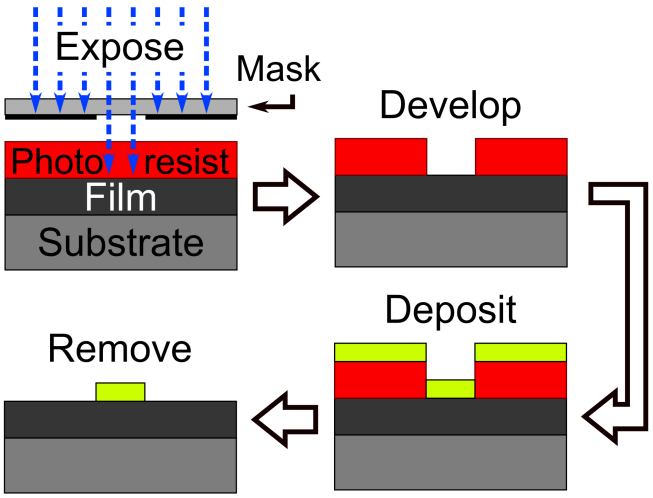

Fig. 4.2.1: A schematic sequence of the positive lift-off process using optical lithography. A positive photoresist on a sample is exposed to (typically UV) light through a mask. The develop step etches the exposed regions of the (here positive) photoresist. After deposition of the desired material the remove step etches the residual photoresist leaving only the structure dictated by the photomask on the sample.

In order to prepare the desired structure of the 3ω heater/thermometer on the samples, a microstructuring by a standard optical lithography lift-off process was used (Fig. 4.2.1), cf. [97]: After spin-coating a (here positive) photoresist on the sample, an exposure by a UV light source is done through an appropriate mask. The exposed regions are then etched during the develop step. After an aereal deposition of the desired metal, the lift-off removal step etches the residual unexposed photoresist such that a microstructure dictated by the photomask remains.

The lithography processing was carried out within the class 100 (ISO 14644-1-5) lithography cleanroom of the Physical Faculty of Georg-August-University of Goettingen. As an exposure unit the mask aligner *Karl SÜSS MJB4* was used. To achieve a good lift-off process, the *Allresist AR-P 5350* positive photoresist was chosen with a critical dimension specification of up to CD = 0.5 µm. The following recipe was found to achieve best results leaned on the datasheet of the resist:

- Resist spincoating at 4000 rpm for 60 s (800 rpm/s ramp).
- Resist drying on 105℃ hotplate for 4 min.
- Exposure for 2 s using a Hg lamp at a constant power of 200 W achieving $E \approx 20$ mW/cm^2 irradiance.
- Develop step in an *Allresist AR 300-35* developer with 1:3 dilution in deionized water for 60 s without ultrasonic bath.
- Rinsing in deionized water in 3 different beakers without ultrasonic bath.
- Thermal evaporation of a chromium adhesion layer and magnetron sputtering of gold for the 3ω metal heater element with *Balzers BAE 250 Coating System* evaporation setup. The growth is controlled by a quartz microbalance with growth parameters listed in Tab. 4.2.1.
- Lift-off using *Allresist AR 300-76* remover in an ultrasonic bath at the lowest rinsing power in 3 different beakers for 30 s each.

Tab. 4.2.1: Growth parameters for Au/Cr deposition for the lithography microstructuring.

	Dep. rate [nm/s]	Thickness [nm]
Cr	0.10(0.02)	5(0.5)
Au	0.25(0.02)	150(5) - 200(5)

5 Physical properties measurement techniques

In this section, the measurement techniques of the physical properties of the used materials are introduced. The techniques cover the measurement techniques of thermal conductivity, structural properties like surface morphology, film thicknesses, lattice parameters, as well as electrical, and magnetic properties.

5.1 The developed 3ω-PPMS setup for thermal conductivity measurements

Figure 5.1.1 presents a scheme of the electronics of the 3ω setup used in this work which is based on the original setup by Cahill [81]. As a current source the sine waveform generator *Keithley 6221* is placed in series with a resistor $R_1 = 36.59\,\Omega$ (*Vishay Precision Group Z201 Series Z-Foil Resistor*, having a low temperature coefficient of resistance $TCR = \pm 0.2$ ppm/K in order to suppress any spurious 3ω generation) and the heater element R_{Au}. The sample is mounted inside the PPMS cryostat ($T = 2 - 400$ K) such that magnetic fields (up to $B \leq 9$ T) can be applied in-plane.

In order to obtain a pure 3ω signal from the sample ($U_{\mathrm{Au},3\omega} = U_{\mathrm{Au}} - U_{\mathrm{Au},1\omega}$), the first harmonic voltage must be subtracted. Here it is established by voltage division of U_{R1} with the same Ohmic drop as of the gold element ($U_{\mathrm{R2}} \stackrel{!}{=} U_{\mathrm{Au},1\omega}$) by matching R_{var} according to

$$U_{\mathrm{Au},1\omega} \stackrel{!}{=} U_{R2} = U_{R1}\frac{R_2}{R_2 + R_{\mathrm{var}}}. \tag{5.1.1}$$

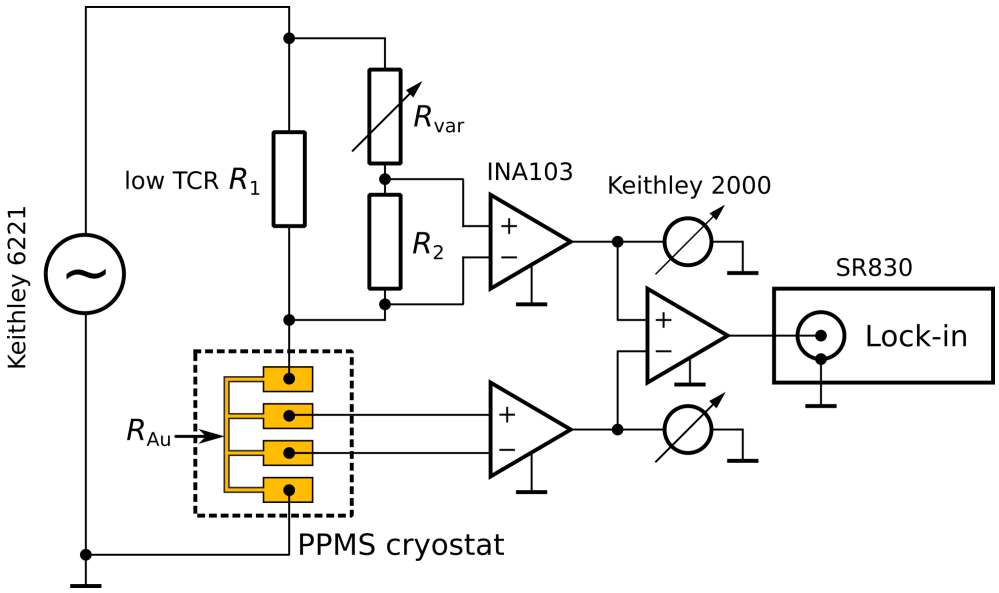

Fig. 5.1.1: Schematics of the 3ω setup used in this work based on the setup by Cahill [81]. The sample (gold pattern of resistance R_{Au}) is placed within the PPMS cryostat. The current leads are connected in series with an AC current source and a precision resistance R_1. The 3ω voltage of R_{Au} is detected by a lock-in using instrumentation amplification after subtracting the pure 1ω Ohmic contribution obtained by appropriate voltage division (R_2/R_{var}) of the precision resistance R_1. The balancing is done by matching the output RMS voltages of the two multimeters before subtraction.

The voltage divider is realized with the high precision resistance decade *burster 1423-IEC* ($R_{\mathrm{var}} = 0.0 - 99{,}999.9\,\Omega$) and a *Vishay Z201* resistor $R_2 = 500\,\Omega$. The division itself is done by instrumentation amplifiers (*Texas Instruments INA103* with amplification factor $\times 1$). The 3ω voltage of the sample with strongly reduced first harmonic signal is then measured by a lock-in amplifier (*Stanford Research Systems SR830*), which further attenuates the residual first harmonic voltage. The balancing of the subtraction can be done in-situ by matching the overall RMS voltage drop of the sample U_{Au} and the precision resistor after voltage division U_{R2} monitored by two *Keithley 2000* multimeters. The precision resistance must be chosen such that $R_1 > R_{\mathrm{Au}}$. The setup control, i.e., temperature, magnetic field, variable resistor controls and data acquisition are realized over the GPIB interface via a simple C# automation script using the GPIB library *NI-VISA* provided by *National Instruments* using commands described in manuals of used instruments.

Sources of systematic errors and errors from approximations including the electronic instrumentation, assumptions for the substrate being isothermal and semi-infinite, one-dimensional quasistatic heat flow from an infinitely long massless and uniform heater line, as well as neglecting convection and radiation typically result in a $\sigma \leq 5\%$ error for 3ω measurements which is ensured by thermal design rules given in the reference [82].

5.2 X-ray techniques

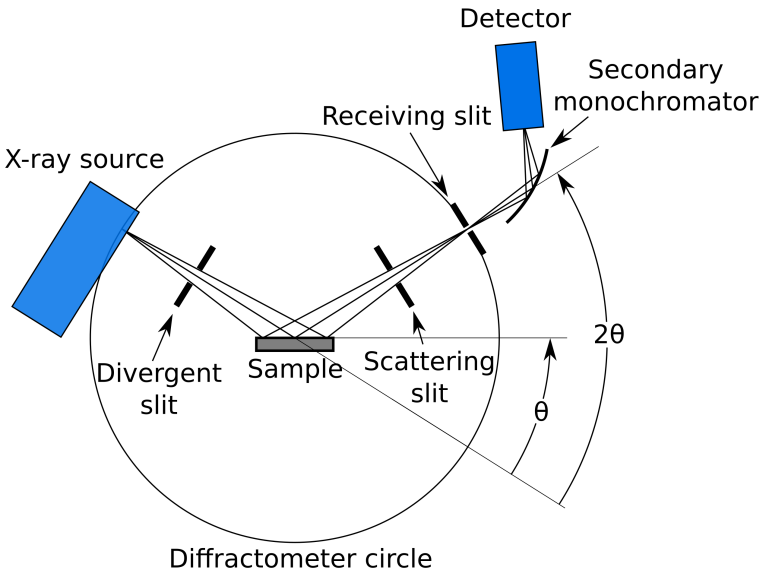

Fig. 5.2.1: Schematic of the *Bruker Advance D8* diffractometer Bragg-Brentano geometry. Redrawn from the manual.

X-ray reflectometry and diffraction were carried out with the *Bruker Advance D8* diffractometer armed with a Cu-anode (with corresponding Cu-$K_{\alpha 1,2}$ wavelengths $\lambda_{K\alpha 1,2} = 1.540593\,\text{Å}$ and $\lambda_{K\alpha 1,2} = 1.544427\,\text{Å}$ according to the manual) and using a classical Bragg-Brentano geometry ($\theta - 2\theta$ measurements, Fig. 5.2.1) [98].

5.2.1 X-ray reflectometry

X-ray reflectometry (XRR) is a technique for characterization of layer thicknesses, density and roughness (surface and/or interface) of thin films and multilayer systems. At grazing incidence angles in the vicinity of the total reflection and up to several angles ($2\theta \approx 0.6° - 10°$) it comes to constructive/destructive interference

due to reflection on the surface/interfaces of a thin film or multilayer system on a substrate. The theoretical background for the quantitative analysis of the emerging angle-dependent oscillating intensity behavior was developed by Kiessing [99] and involves the utilization of the optical parameters and with it the refraction index of the media. The positions of the local extrema for a simple film of thickness d and a refractive index $\underline{n} = 1 - \delta + i\beta$ follow the relation:

$$m\lambda = 2d\sqrt{\theta^2 - 2\delta}, \quad m = 0, 1/2, 1, 3/2, 2, ... \tag{5.2.1}$$

with minima for whole numbers m and maxima else, here the approximation $\sin\theta \approx \theta$ for small angles is used.

Further utilization of surface/interface roughness and modeling a multilayer structure results in a more complex reflectivity angle dependence for which a straightforward analytical analysis as it is done for the case of a single film (Eq. (5.2.1)) is no more possible. For such complex systems, simulations are conducted and fitting algorithms are used in order to extract the material parameters. In this work the freely available, open source computer program for evaluating X-ray reflectivity data *GenX 3* is used [100]. It implements the iterative Parratt formalism [101] for modeling reflectivity of a multilayer system and allows for fitting surface/interface roughness and densities of the materials. The fitting is done using the *Differential Evolution* algorithm [102, 103] with a logarithmic residuals cost function.

5.2.2 X-ray diffraction

The X-ray diffraction (XRD) is used for estimation of the crystal structure, epitaxy or strain state of a sample and allows for obtaining chemical as well as structural information and calculation of lattice parameters of crystals, to name a few possibilities. A comprehensive description of this standard technique can be found in relevant reviewing textbooks [104, 105], here only a small excerpt is given for the standard lattice parameter calculation used in this work.

The reflection at high angles ($\theta \gtrapprox 10°$) occurs due to coherent scattering on the electrons (structure factor) of the specimen which constructively interfere to a characteristic angle dependent reflection pattern. The angles for constructive

interference are given according to the Bragg-law:

$$2d_{hkl} \sin\theta = m\lambda, \tag{5.2.2}$$

with the interplanar spacing $d_{hkl} = c/\sqrt{h^2 + k^2 + l^2}$ of planes with Miller indices h, k, l and the out-of-plane lattice constant c, the Bragg order m and the X-ray wavelength λ.

5.3 Electrical resistivity

The electrical resistivity of the samples was measured by an in-line uniformly spaced (spacing distance $s \approx 2$ mm) four-point probe technique either by using the *Resistivity* option of the *Quantum Design PPMS* or by *Keithley 6221* as a constant DC current source paired with a *Keithley 2000* voltmeter. The four-point probe method allows for elimination of spurious voltage drops of contact and lead resistances, cf. [106]. The contacting was established by copper wires and a silver paste. For the sheet resistance R_s and resistivity ρ calculation the standard formula for thin films was used [106, p. 28-3]:

$$\rho = R_s d \approx \frac{\pi}{\ln 2} R d = \frac{\pi}{\ln 2} \frac{U}{I} d, \tag{5.3.1}$$

with thickness d, electrical resistance R, current I and voltage drop U. The approximation requirement $d \leq s/2$ is easily satisfied when dealing with nanoscale thin films.

5.4 Magnetization measurements

Magnetization measurements were carried out by the *Magnetic Properties Measurement System Quantum Design MPMS XL* and *MPMS3* superconducting quantum interference devices (SQUID). The former provided in-plane magnetic measurements using a straw/gelatine capsule holder. The latter was used either with the *Standard* rotator option for angle dependent measurements or with the

brass/quartz holder for in-plane and out-of-plane measurements. The samples for the *MPMS3* were mounted with Kapton tape.

Conversion of the measured electromagnetic units of magnetic moment m [emu] to magnetization M [μ_B/u.c.] in units of Bohr's magnetons per unit cell are carried out using the formula:

$$M = \frac{m \cdot V_\mathrm{u.c.}}{V} \frac{10^{-3}\,\frac{\mathrm{J}}{\mathrm{T}}}{\mathrm{emu}} \frac{\mu_\mathrm{B}}{\frac{e\hbar}{2m_e}} \approx \frac{m \cdot V_\mathrm{u.c.} \cdot 1.0782823 \cdot 10^{-20}\,\frac{\mu_\mathrm{B}}{\mathrm{emu}}}{V}, \tag{5.4.1}$$

with the unit cell volume $V_\mathrm{u.c.}$ and the volume of the measured sample V.

The Curie temperature is measured here as the minimum of the temperature coefficient of magnetization (a logarithmic derivative):

$$T_\mathrm{C} = \min\left(\frac{\mathrm{d}\ln(m)}{\mathrm{d}T}\right) = \min\left(\frac{1}{m}\frac{\mathrm{d}(m)}{\mathrm{d}T}\right). \tag{5.4.2}$$

For that, a constant diamagnetic contribution is subtracted and assumed to be temperature independent.

Part III

Results and discussion

6 Thermal conductivity of substrates and capping layers

6.1 Introduction and motivation

In order to measure thermal conductivity of a thin film on a substrate, the precise knowledge of the thermal properties of the used substrates and capping layers is crucial. Therefore, the MAD-grown amorphous alumina am-Al_2O_3 thin films used in this thesis as an insulating capping layer on electrically conducting films, as well as bulk MgO(100) and STO(100) substrates (dimensions: $10\times5\times0.5$ mm^3) were analyzed. This is additionally useful for testing and benchmarking of the developed 3ω-PPMS setup since the thermal properties of the mentioned materials are well known in literature.

The estimation of thermal conductivity values is done using the *differential evolution* fitting algorithm [102, 103] in analogy to the GenX program [100] for fitting X-ray data but here with a least squares cost function. Numerically calculated temperature oscillation of the heater or the surface thermal impedance (according to the analytical expressions given in Section 3.2.1) are fitted to the obtained 3ω data such that thermal conductivity and diffusivity of substrates or thermal resistances of thin films are estimated from the best fit.

6.2 Substrate measurements

Metal heater lines built of of 200 nm Au on 5 nm adhesive Cr were prepared by optical lithography lift-off using thermal evaporation of Cr and subsequent magnetron sputtering of Au as described in section 4.2. Optical microscopy

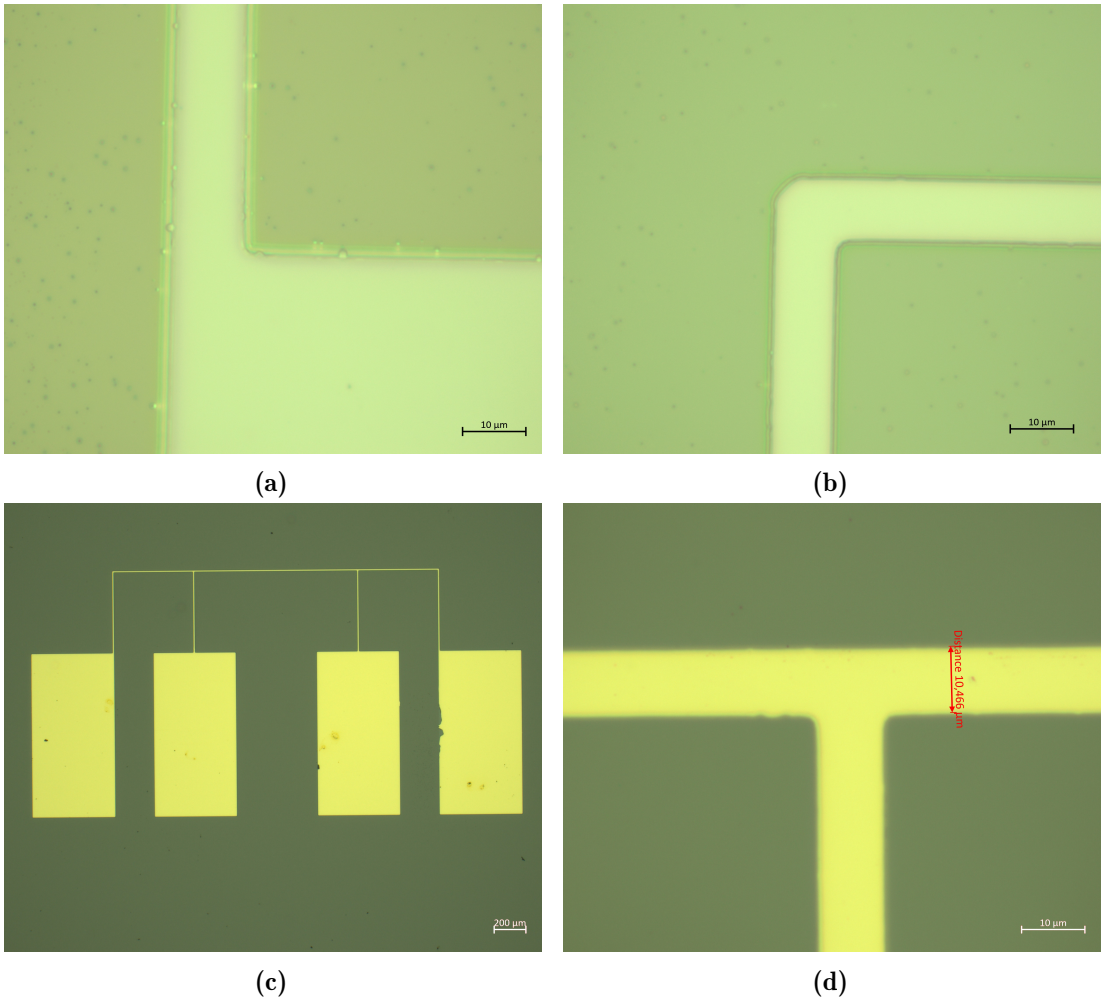

(a) **(b)**

(c) **(d)**

Fig. 6.2.1: Optical microscope pictures of the lithography lift-off patterning of Au/Cr metal element on the STO(100) substrate sample: (a)-(b) Structure after exposure and development step, darker regions correspond to the photoresist layer. (c)-(d) Ready metal element structure after deposition and lift-off. Structure width $2b$=10.5(1) µm.

pictures of the structure after the lithography development step and after the lift-off for the exemplary STO(100) substrate are shown in Fig. 6.2.1 confirming the integrity of the heater element.

The electrical resistance of the gold line element behaves linearly as a function of temperature within the measured range (50 K $< T <$ 370 K) as expected (see Fig. A.1.2 in Appendix on p. 104), the linear regression has a correlation coefficient of $R^2 = 0.99987$ indicating a good fit. Further, from the linearity of the 3ω voltage signal as a function of the cube excitation current according to Eq. (3.2.12) (see

Fig. A.1.1 in Appendix on p. 103) it can be assumed that the 3ω signal has a purely thermal origin and is not affected by spurious contributions, cf. Sec. 3.2.1.

6.2.1 The STO(100) substrate

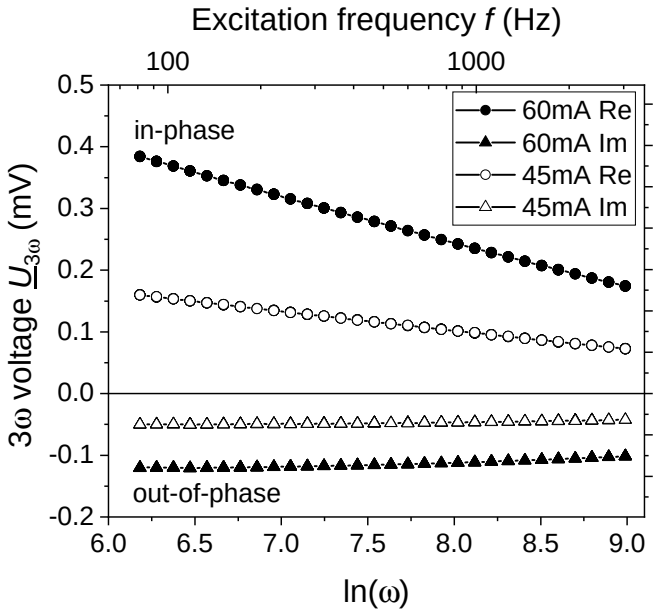

Fig. 6.2.2: Raw signal of the complex 3ω voltage $\underline{U}_{3\omega}$ of the heater element on the STO(100) substrate at different excitation currents and frequencies at $T = 300$ K.

Fig. 6.2.2 presents the raw 3ω signal of the heater element on the STO(100) substrate in a frequency range 77 Hz $< f <$ 1277 Hz (corresponding to 6.18 $< \ln(\omega) <$ 9) at two different excitation currents $I_{1\omega,\mathrm{rms}} = 45$ and 60 mA near room temperature ($T = 300$ K). Using Eq. (3.2.1), the raw signal can be converted to a more intuitive temperature oscillation of the heater element $\underline{T}$ as shown in Fig. 6.2.3a. The red curves are the fits of the analytical Eq. (3.2.3) to the data assuming isotropic thermal conductivity $\kappa_{xy} = 1$ and semi-infinite substrate approximation $A_n = -1$.

Using different excitation currents and thus varying heating power obviously leads to different temperature oscillations, which can also depend on heater dimensions when using different samples. The concept of thermal impedance as introduced in the theory section 3.2.1 can thus be applied making measurements independent of the current source power or heater dimensions. Using Eq. (3.2.11) the thermal impedance can be calculated from the 3ω signal and is shown in Fig. 6.2.3b for

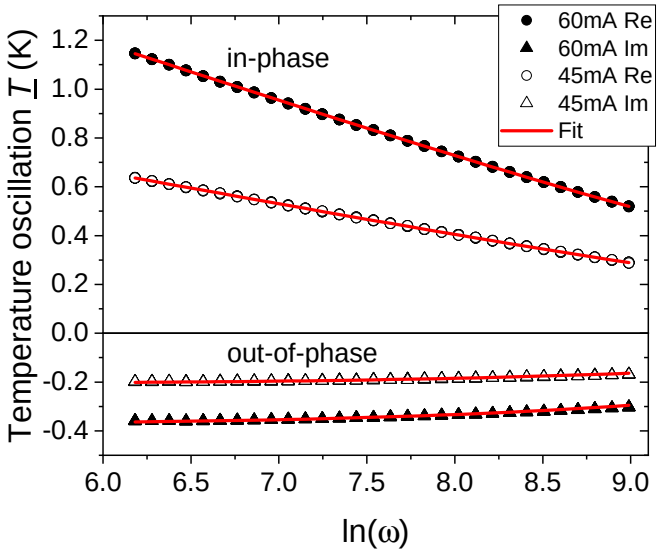

(a) Temperature oscillation $\underline{T}$ notation.

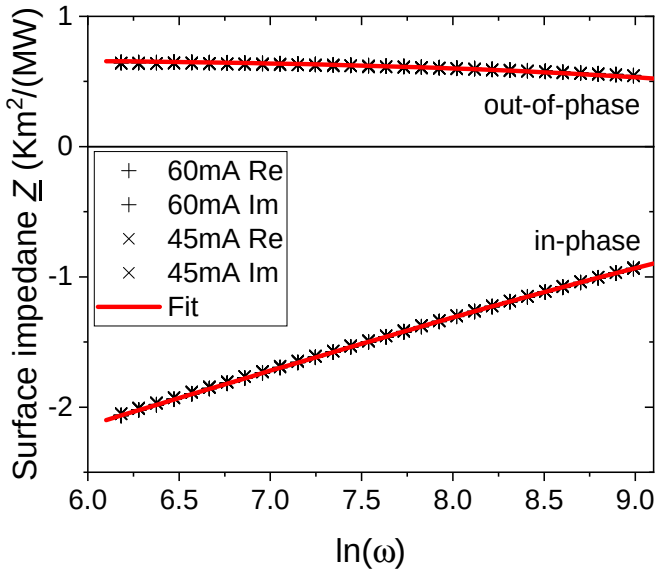

(b) Surface thermal impedance $\underline{Z}$ notation.

Fig. 6.2.3: Frequency dependent 3ω signal of the heater element of the STO(100) substrate at $T = 300$ K converted to different notations.

the STO(100) substrate measurement. One can clearly see the setup-independent character of thermal impedance as the measurements at different excitation currents now lie on top of each other. Here, the fits are done according to Eq. (3.2.14).

In order to obtain the temperature dependence of thermal conductivity, the data reduction procedure using a continuous temperature sweep as described in

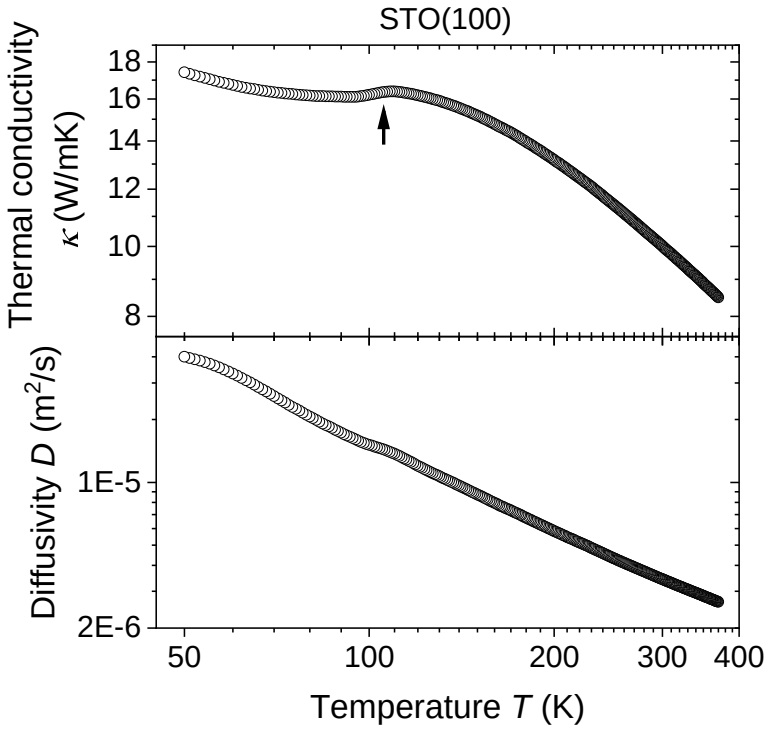

Fig. 6.2.4: Thermal conductivity κ and Diffusivity D values from the 3ω fits for the STO(100) substrate. The arrow indicates the cubic-tetragonal antiferrodistortive structural transition temperature of STO at $T_{\mathrm{STO}} = 105$ K.

Appendix Sec. A.2 (p. 105) was used to measure the 3ω signal of the STO(100) substrate at $f \approx 41$ Hz and 62 Hz current excitation frequencies. The resulting fit parameters for the thermal conductivity κ and diffusivity D are shown in Fig. 6.2.4 which fit well to literature values for STO [107]. The slight decrease of the thermal conductivity (and a slight kink in diffusivity) below $T_{\mathrm{STO}} = 105$ K is accounted to the cubic-tetragonal structural transition of STO which is accompanied by the oxygen octahedral rotation along the z-axis also known as antiferrodistortive transition [107] [108]. Room temperature values of κ and D of the STO substrate are summed up in the overview Tab. 6.3.1 (p. 59).

6.2.2 The MgO(100) substrate

A similar evaluation for the MgO(100) substrate provides the corresponding thermal conductivity and diffusivity values as shown in Fig. 6.2.5 that also fit well to literature values [109, 110]. Here, the change in slope $\mathrm{d}\kappa/\mathrm{d}T > 0$ below ≈ 60 K is most likely due to the crossover from boundary/defect scattering and increasing heat capacity leading to $\mathrm{d}\kappa/\mathrm{d}T > 0$ at low temperatures to the dominant Umklapp

scattering resulting in $\mathrm{d}\kappa/\mathrm{d}T < 0$ at high temperatures typical for crystalline materials, cf. [75].

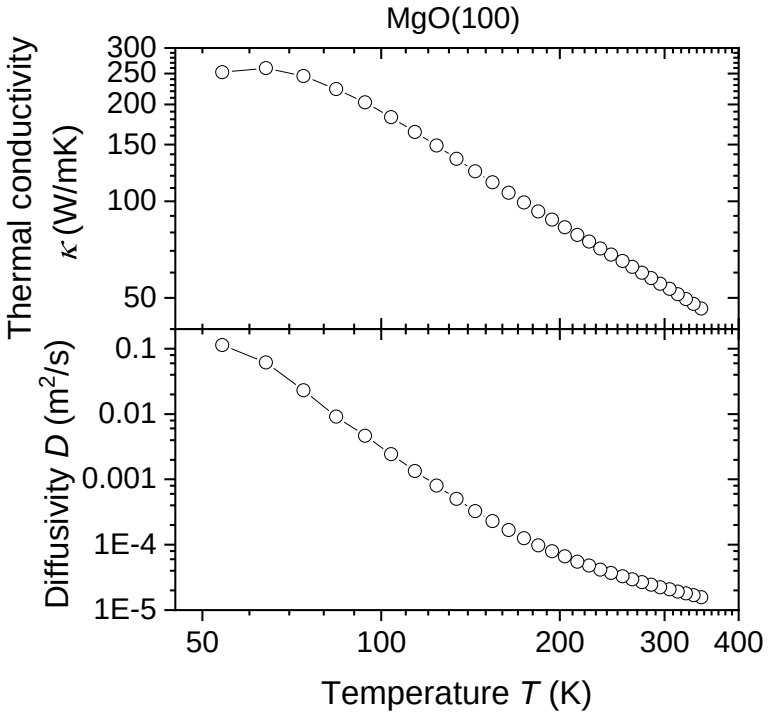

Fig. 6.2.5: Thermal conductivity κ and diffusivity D values from the 3ω fit for the MgO(100) substrate.

6.3 Amorphous alumina thin films

Thin films of amorphous alumina am-Al_2O_3 were grown with the MAD technique on STO(100) substrates and patterned analogously to previous samples with lithography lift-off (Fig. 6.3.1 shows the scanning electron microscopy images of the metal element structure on the alumina sample). Fig. 6.3.2 presents X-ray reflectivity measurements of the films along with the fits done by the GenX fitting program [100] estimating the film thicknesses of $d_{\mathrm{fit}} = 19.9(2)$ nm, 39.8(2) nm and 58.1(2) nm respectively. The fitting additionally provides the density of the films of $\varrho = 3.3(2)$ g/cm^3 which is comparable to literature values of similar am-Al_2O_3 films on silicon or sapphire substrates grown by atomic layer deposition or sputtering [111].

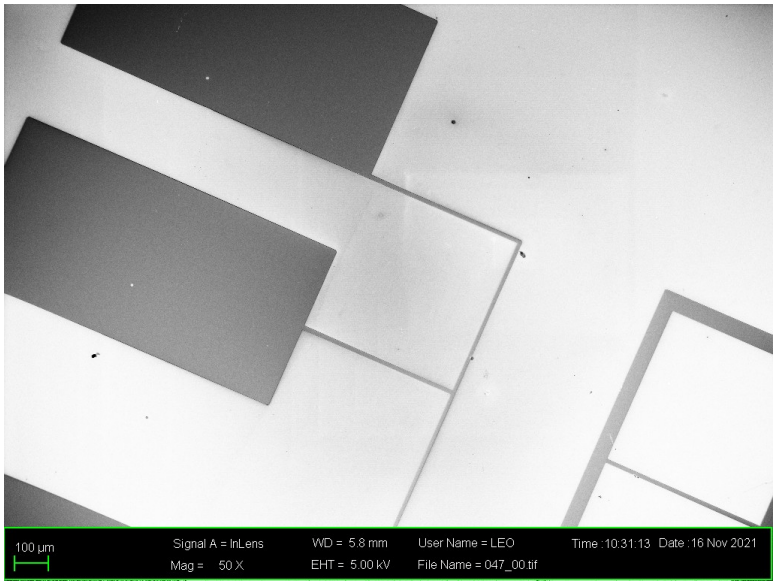

(a)

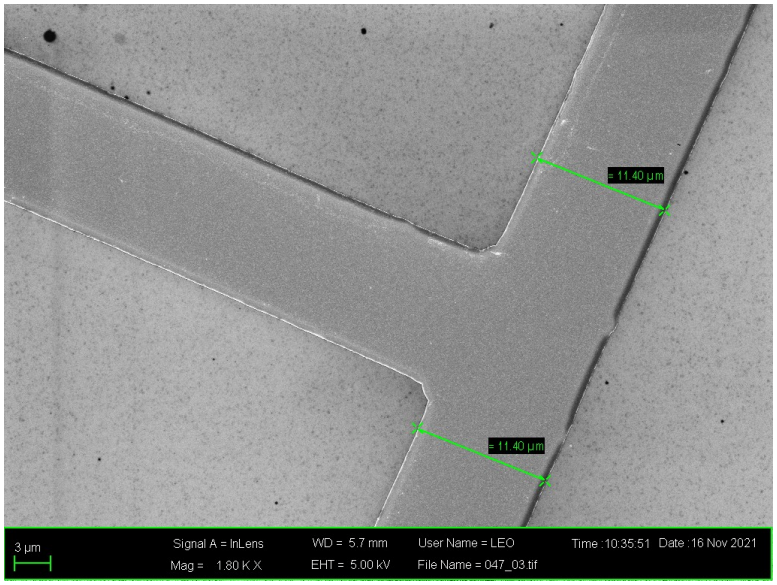

(b)

Fig. 6.3.1: Scanning electron microscopy pictures of the Au/Cr metal element after the lithography lift-off on the $d = 19.9$ nm am-Al_2O_3STO(100) sample with different magnifications. The structure width amounts to $2b$=11.4(1) µm.

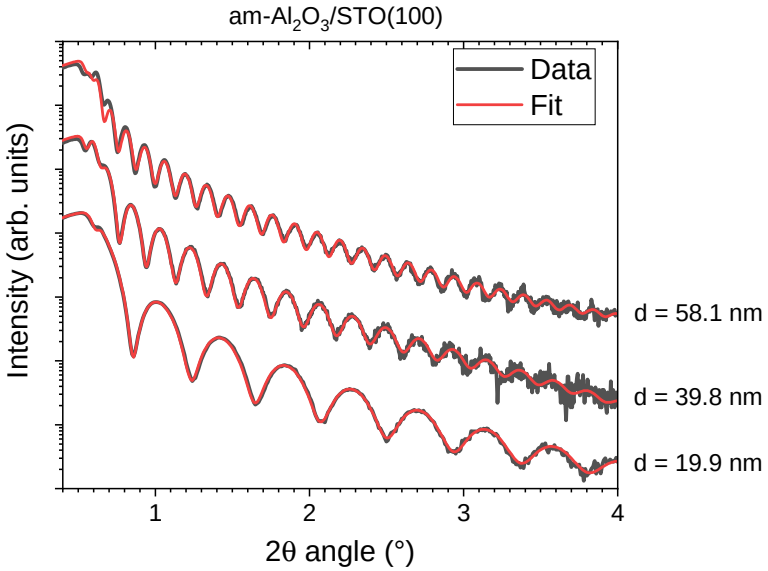

Fig. 6.3.2: X-ray reflectivity measurements of am-Al_2O_3/STO(100) thin films with respective fits by GenX [100] determining the film thicknesses. The thickness error of the fits amounts to $\sigma_d = 0.2$ nm. The curves are shifted in ordinate for clarity.

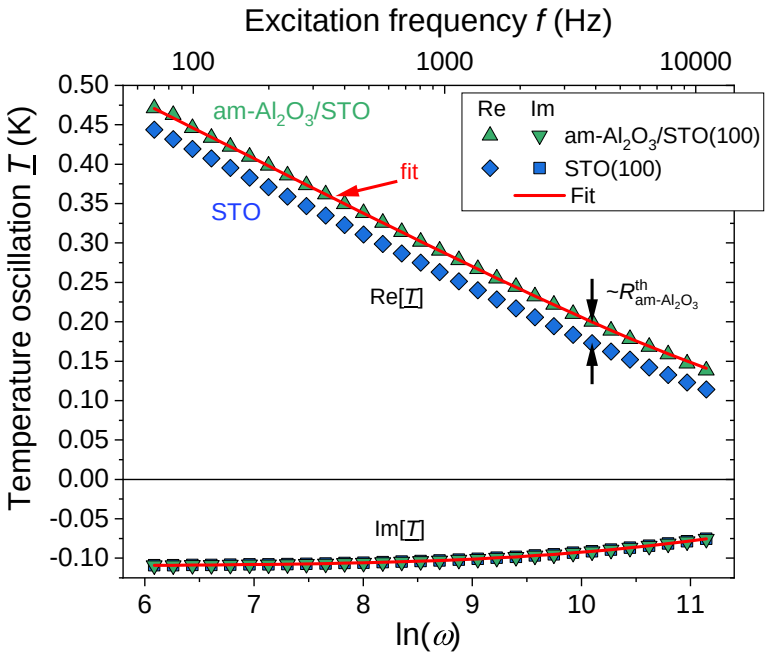

Fig. 6.3.3: 3ω measurement of the temperature oscillation $\underline{T}$ of the heater line element of the d=58.1 nm am-Al_2O_3/STO(100) sample (green triangles) at $T = 300$ K. The temperature oscillation for the STO substrate (blue rectangles) is shown from a separate measurement. The red line represents the fit according to the analytical expression of Eq. (3.2.3). The temperature offset of the real part between the two measurements is proportional to the thermal resistance R_{th} of the film.

Fig. 6.3.3 presents an exemplary 3ω measurement of the temperature oscillation of the heater line element on top of the d=58.1 nm am-Al_2O_3/STO(100) sample near room temperature ($T = 300$ K) along with the calculated temperature oscillation of the STO(100) substrate from its thermal properties using the analytical expression of Eq. (3.2.3). A corresponding fit to the alumina measurement is done according to the thermal series resistance model, Eq. (3.2.8). For the temperature dependent measurements, the continuous temperature sweep method (Sec. A.2) was used to obtain the total thermal resistances of the films shown in Fig. 6.3.4.

Following Eq. (3.2.9), the thickness series allows for distinguishing between the thickness dependent intrinsic thermal resistance of the film R_f, which is connected to the thermal conductivity by $\kappa_f = d_f/R_\mathrm{f}$, as well as the thickness independent thermal boundary resistances summed up as R_tbr. Since the thermal resistance is a linear function of the sample thickness, the thermal boundary resistance can be simply calculated from the y-axis intercept of the linear regression $R_\mathrm{tbr} = R_\mathrm{tot}(d = 0)$ as exemplarily shown in Fig. 6.3.4. The intrinsic thermal conductivity of the film is then given by the reciprocal slope and is shown in Fig. 6.3.5 (this is also known as *differential* 3ω technique, cf. [82]).

All in all, the values of the thermal conductivity of MAD-grown amorphous alumina films are well comparable to literature values of similar thin films [87, 111] on different substrates. The thermal boundary resistances measured here coincide with other literature values for Pt/am-Al_2O_3/sapphire or Au/Ti/am-Al_2O_3/Si thin films [87]. The results for room temperature are additionally summarized in Tab. 6.3.2.

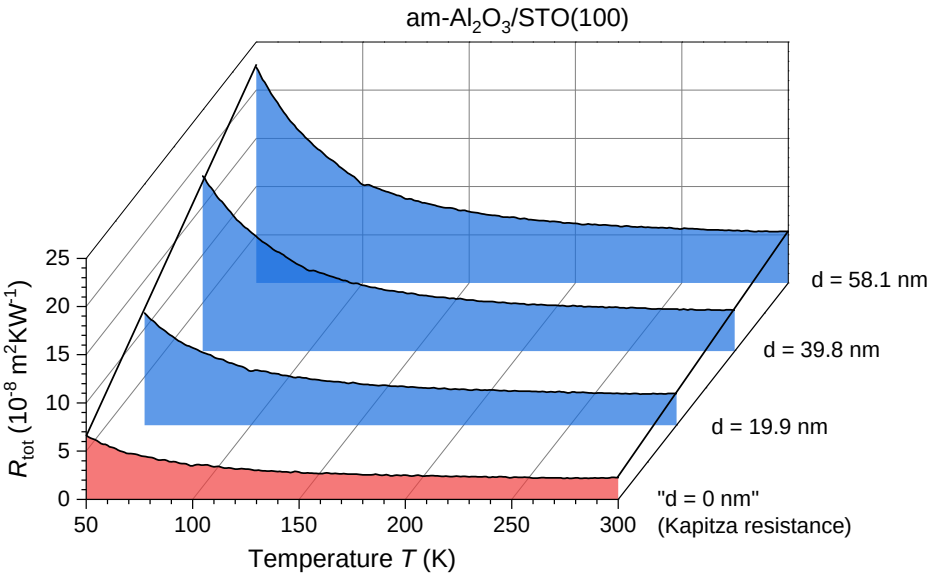

Fig. 6.3.4: Total thermal resistance R_{tot} of am-Al_2O_3/STO(100) thin films with different thicknesses d as function of temperature. The linear interpolation to the ordinate intercept at each temperature, as exemplarily indicated by black lines at T=50 K and T=300 K, lead to the determination of the thickness independent contribution of thermal boundary (Kapitza) resistances R_{tbr} at "$d = 0$".

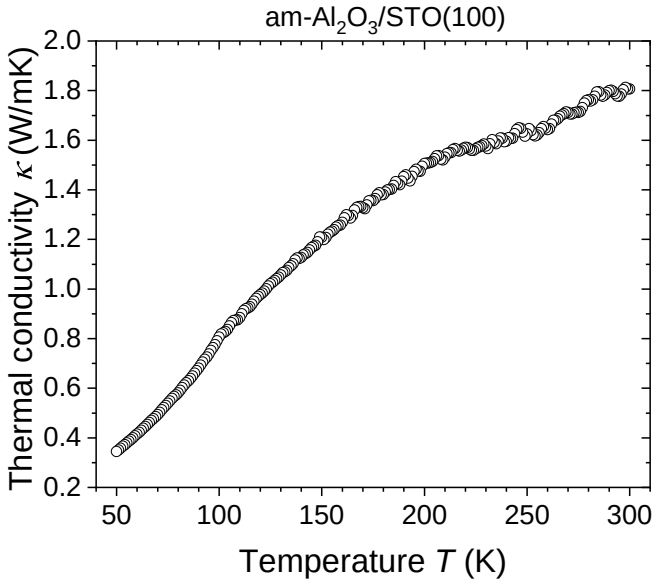

Fig. 6.3.5: Thermal conductivity of MAD-grown am-Al_2O_3/STO(100) thin films calculated from the reciprocal slope of the thickness dependent thermal resistance measurements.

Tab. 6.3.1: Thermal properties of STO(100) and MgO(100) substrates at T=300 K.

Sample	Reference	Thermal conductivity κ ($\mathrm{Wm^{-1}K^{-1}}$)	Diffusivity D (10^{-6} $\mathrm{m^2s^{-1}}$)
STO(100)	This work	10.0	3.4
	[107]	≈10.5	4.0
MgO(100)	This work	46.3	15.7
	[109]	49.9	15.22

Tab. 6.3.2: Thermal properties of amorphous alumina am-Al_2O_3 thin films at T=300 K compared to literature values. TBR: thermal boundary resistance.

Sample	Reference	Density ϱ ($\mathrm{g\ cm^{-3}}$)	Th. conductivity κ ($\mathrm{Wm^{-1}K^{-1}}$)	TBR R_{tbr} (10^{-8} $\mathrm{m^2KW^{-1}}$)
am-Al_2O_3/STO(100)	This work	3.3 ± 0.2	1.81	2.24
am-Al_2O_3/Si	[111]	3.3 ± 0.1	1.90 ± 0.15	2
am-Al_2O_3/Sapphire	[111]	3.3 ± 0.1	1.99 ± 0.16	0.1

6.4 Discussion on thermal conductivity of substrates and capping layers

The 3ω measurements done on the substrates and capping layers that will be used in subsequent measurements of manganites successfully demonstrate the capability of the developed 3ω-PPMS setup of simultaneously measuring substrate's thermal conductivity along with its thermal diffusivity as well as measuring thermal resistances of nanoscale thin films.

Although being equivalent, the use of Olson-Graham-Chen's surface thermal impedance model instead of Cahill's temperature oscillation model simplifies the data analysis making measurements independent of heating power or heater element dimensions. Additionally, it provides a possibility of distinguishing setup errors if measurements of the same sample at different driving currents do not lead to the same results.

In order to verify that applying a magnetic field does not lead to any spurious contributions to the 3ω signal, e.g., from unwanted Hall voltages, a 3ω measurement of an exemplary am-Al_2O_3/STO(100) thin film was done applying a magnetic field of $B = 5$ T. This did not result in any changes compared to the field-free 3ω measurement (Fig. A.1.3 in Appendix on p. 104), as expected, since the thermal conductivity of a diamagnetic dielectric does not change in an external field.

All together, the measured values of thermal conductivity (and thermal diffusivity of substrates) fit well to literature values supporting the validity of measurements and evaluations.

7 Magneto-thermal conductivity of LPCMO thin films

7.1 Introduction and motivation

The lanthanum-praseodymium-calcium manganite $(La_{0.6}Pr_{0.4})_{0.7}Ca_{0.3}MnO_3$ (LPCMO) is a colossal-magnetoresistive manganite with a distinct insulator-metal transition at the paramagnetic-ferromagnetic transition temperature of around $T_C \approx 195$ K when grown epitaxially on MgO(100) with a strong electron-phonon coupling [49]. The epitaxial strain is released by misfit dislocations near the interface in a region of 2-3 monolayers allowing a subsequent strain-free growth of the film, ibid. Using the $LaAlO_3$ (LAO) buffer layer on a STO(100) substrate instead, allows for reducing the epitaxial stress and enables a homogeneous and nearly unstrained growth of the LPCMO thin film [112]. With such strain engineering it is possible to compare the thermal properties of LPCMO thin films of similar strain states on different substrates.

This chapter provides magnetic field dependent measurements of thermal conductivity of LPCMO thin films grown either on MgO(100) or LAO ($d_{LAO} = 9$ nm) buffered STO(100) (LAO/STO(100)) substrates using the MAD technique. The measurements and the evaluations of thermal conductivity are done analogously to the procedure described in the previous chapter. To the best of my knowledge, there are no reports on magnetic-field dependent thermal conductivity of LPCMO thin films in literature.

7.2 Magnetic field dependent thermal conductivity of LPCMO/MgO(100) thin films

Thermal conductivity of thin LPCMO/MgO(100) films of thicknesses d = 51 nm and 120 nm with a d_{Al2O3} = 60 nm thick am-Al_2O_3 insulating capping layer and with a Au/Cr metal heater element (d_{Au} = 150 nm, d_{Cr} = 5 nm) on top were measured by means of the 3ω technique. The evaluation includes the thermal parameters for the MgO(100) substrate as well as of the am-Al_2O_3 capping film presented in the previous chapter which allows for obtaining the thermal resistance of the LPCMO films. The latter is then converted to thermal conductivity according to the film thickness.

Fig. 7.2.1 presents the temperature dependencies of magnetic moment (external magnetic field in-plane), electrical resistance (current and field in-plane, the amorphous alumina was scraped away with a scalpel for contacting) and the cross-plane thermal conductivity of the LPCMO/MgO(100) thin films at different (in-

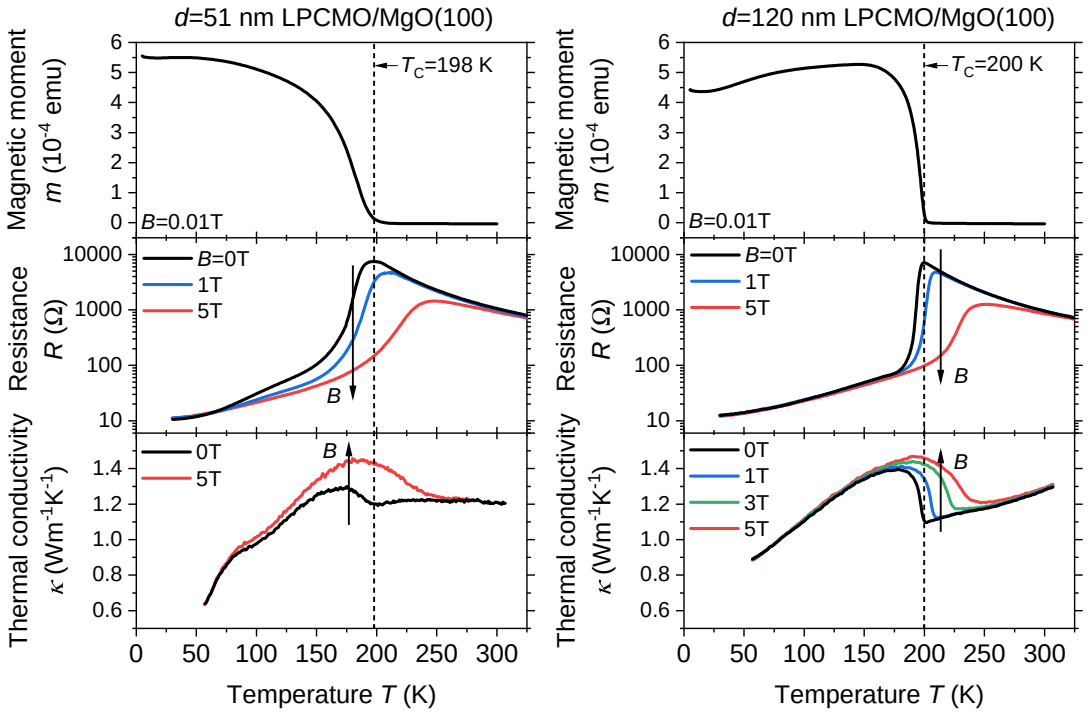

Fig. 7.2.1: Magnetic field cooled measurements of the magnetic moment (top graph), electrical resistance (middle) and thermal conductivity (bottom) of LPCMO/MgO(100) thin films with thicknesses of d = 51 nm (left) and 120 nm (right) respectively.

plane) external magnetic fields up to $B = 5$ T. The overall thermal characteristics of both samples are comparable except for deviations originating from a sharper phase transition of the thicker sample (see for example MR/CMR values in Fig. 7.4.1, p. 70).

The Curie temperature $T_C \approx 200$ K of both samples fits well to literature bulk values of comparable doping level [113] and of similar thin films on MgO(100) [49]. The paramagnetic-to-ferromagnetic phase transition of the thin film is slightly smeared out compared to the thicker sample indicating a coexistence of phases with different Curie temperatures within the sample. The thicker sample additionally shows a decrease of magnetization at low temperatures with $\mathrm{d}m/\mathrm{d}T > 0$ most probably because of a too low external field that is unable to align all magnetic moments as the coercive field of the sample becomes larger than the applied field at low temperatures.

The electrical resistance of LPCMO is known to undergo an insulator-metal transition which is clearly seen in both samples coinciding with the paramagnetic-ferromagnetic transition at the Curie temperature due to the double exchange mechanism, cf. [114]; this has been also reported for similar MAD-grown films, additionally pointing out the importance of phase separation mediated by the correlated polaronic antiferromagnetic coupling of ferromagnetic domains, cf. [49]. Applying a magnetic field leads to a drastic decrease of the electrical resistance in the vicinity of the transition temperature resulting in $CMR \approx 5900\%$ for the 51 nm sample and $CMR \approx 7200\%$ for the 120 nm sample (resistance changes by $MR \approx -98\%$ and -99% respectively). These values are also in line with literature values of bulk and thin films of comparable doping level [49, 114].

The measured thermal conductivities of LPCMO thin films on MgO(100) shown in Fig. 7.2.1 reveal values of $\kappa \lessapprox 1.5$ $\mathrm{Wm^{-1}K^{-1}}$ following a continuous decrease by decreasing temperature except a region around $T = 200$ K in the vicinity of the paramagnetic-ferromagnetic transition, which is also coupled to the insulator-metal transition. Here, the thermal conductivity rises by about 10% (30%) for the $d = 51$ nm (120 nm) sample when the sample undergoes the insulator-metal transition. Usually, thermal conductivity values in the order of magnitude $\kappa \approx 1$ $\mathrm{Wm^{-1}K^{-1}}$ and $\mathrm{d}\kappa/\mathrm{d}T > 0$ are fingerprints of amorphous materials, cf. [75]. In manganites, however, despite crystallinity, this behavior is attributed to the complex unit cell, its distortions like oxygen octahedral tilting and large anharmonic lattice

dynamics due to Jahn-Teller defects, cf. [115, 116]. Additionally, applying an external magnetic field leads to an increase of thermal conductivity in the vicinity of T_C accompanied with magneto-thermal conductivity (MTC) values of up to $MTC = 100\% \cdot \Delta\kappa(H)/\kappa(H = 0) \approx 20\%$ (33%) for a field of $B = 5$ T. Such behavior is also reported for bulk LPCMO with a slightly different composition of $(La_{0.25}Pr_{0.75})_{0.7}Ca_{0.3}MnO_3$, however having a lower transition temperature $T_C \approx 100$ K [117]. Moreover, bulk manganites like $La_{0.2}Nd_{0.4}Pb_{0.4}MnO_3$ (LNPMO) [115] or $La_{1-x}Ca_xMnO_3$ (LCMO) [118] with double-exchange mediated metal-insulator transitions show similar behavior. The transition temperatures of the LPCMO studied here, i.e., the paramagnetic-ferromagnetic and the insulator-metal transitions as well as the onset of the thermal conductivity increase coincide at the same critical temperature, supporting the strong interconnection of magnetic, electronic, and thermal properties of this material. The origin of the thermal conductivity increase at T_C upon cooling as well as the observed MTC shall be discussed in the following.

Since the electrical resistance decreases by several orders of magnitude by decreasing temperature even without an external field (as well as when applying magnetic field in the vicinity of the T_C), it seems to be natural at the first glance to attribute the increase of thermal conductivity to the additional emerging electronic contribution. Using the Wiedemann-Franz (WF) law (Equation (3.1.5)) allows for an estimation of such a contribution which is shown in Fig. 7.2.2. Although the changes seem to directly correlate with the electrical resistance changes, the electronic contribution to thermal conductivity described by the WF law accounts only for approximately one third of the increase of κ below T_C and of the magneto-thermal conductivity (MTC) of LPCMO. An increase of the Lorenz number within the WF law beyond the Sommerfeld value ($L_0 = \frac{\pi^2}{3}\left(\frac{k_B}{e}\right)^2 \approx 2.4453 \cdot 10^{-8}$ V^2/K^2) applicable for a free electron gas seems to be not reasonable in a strongly correlated system like LPCMO, therefore both the increase of thermal conductivity below T_C and the MTC most probably do not originate from the electronic contribution only. As discussed in the literature for similar bulk CMR manganites, the thermal conductivity can be additionally affected by crystal distortions that are also coupled to electron mobility within the double exchange model, like the Jahn-Teller distortions changing the Mn-O-Mn distances and often being accompanied by oxygen octahedral tilts changing the Mn-O-Mn angles, cf. [115–117, 119]. Typically, Jahn-Teller distorted crystals are charge/orbital-ordered and insulating,

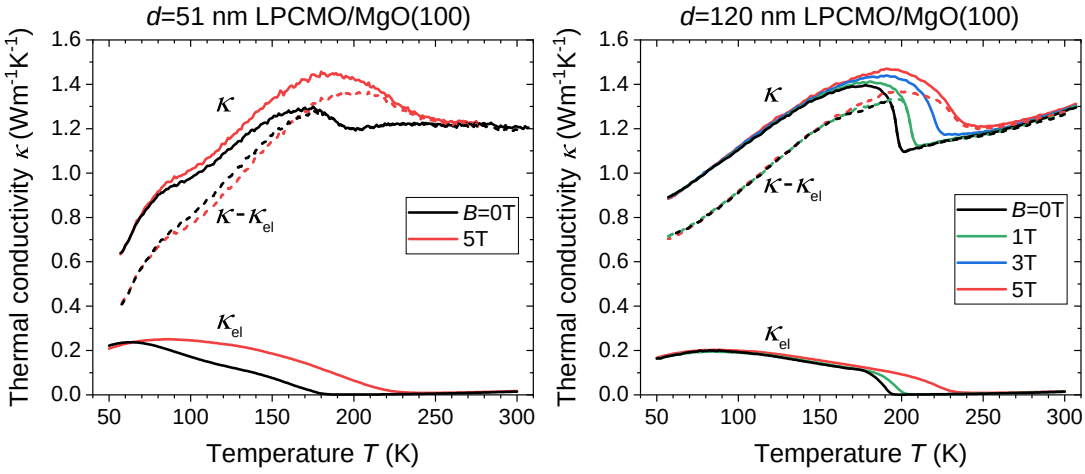

Fig. 7.2.2: Field cooled measurements of the thermal conductivity κ of LPCMO/MgO(100) thin films with thicknesses $d = 51$ nm (left) and 120 nm (right) respectively in different magnetic fields. The calculated electronic contribution to thermal conductivity κ_{el} according to the Wiedemann-Franz law is shown along with its subtraction from the total thermal conductivity (dashed lines).

and octahedral tilting (Mn-O-Mn angle reduction compared to the ideal cubic case of 180°) in electrically conducting manganites results in reduced itinerant electron bandwidth, so that such crystal defects are not only affecting electron mobility but also strongly influence phonon scattering rates and thereby effectively influence thermal conductivity [115, 117]. It was shown theoretically by Fumega et al. [120] for the perovskite STO, that already a change of the oxygen octahedral tilt angle of $\Delta\theta = 0.5°$ results in thermal conductivity changes of as much as $\Delta\kappa \approx 10\%$. Radaelli et al. [119] have also shown experimentally by using neutron powder diffraction that the Mn-O-Mn bond angle of the colossal magnetoresistive LCMO (which is a parent compound of LPCMO) increases by $\Delta\theta = 0.6°$ when the material undergoes the insulator-metal transition by cooling below $T_{\mathrm{C,LCMO}}$. Considering the fact that the $T_{\mathrm{C,LPCMO}}$ of LPCMO used in this work is lower by about 30-50 K than that of LCMO as well as that the insulator-metal transition is much more pronounced, one can expect even larger changes in tilting angles in LPCMO compared to the LCMO. It is therefore very probable that in addition to the electronic contribution within the WF law, also the change of oxygen octahedral tilting and Jahn-Teller defects, i.e., polarons, play a major role in the thermal conductivity increase below T_{C} in LPCMO as well as in explaining its strong MTC.

7.3 Magnetic field dependent thermal conductivity of LPCMO/LAO/STO(100) thin films

Using LAO buffered STO(100) allows for a nearly stress-free homogeneous growth of epitaxial LPCMO, cf. [112]. Thin films of $d = 100$ nm and 200 nm of LPCMO were grown on buffered LAO/STO(100) with a 9 nm thick LAO buffer layer and a 80 nm thick am-Al_2O_3 capping layer on top. The Au/Cr metal heater element dimensions as well as the measurements and evaluations are similar to those of the LPCMO/MgO(100) samples from the previous section.

The temperature dependencies of the magnetic moment, electrical resistance and thermal conductivity (Fig. 7.3.1) follow approximately the same behavior as the samples on MgO(100) (Fig. 7.2.1) with following minor differences: First, the Curie temperature $T_C \approx 205$ K is slightly higher (+5K) than that of the

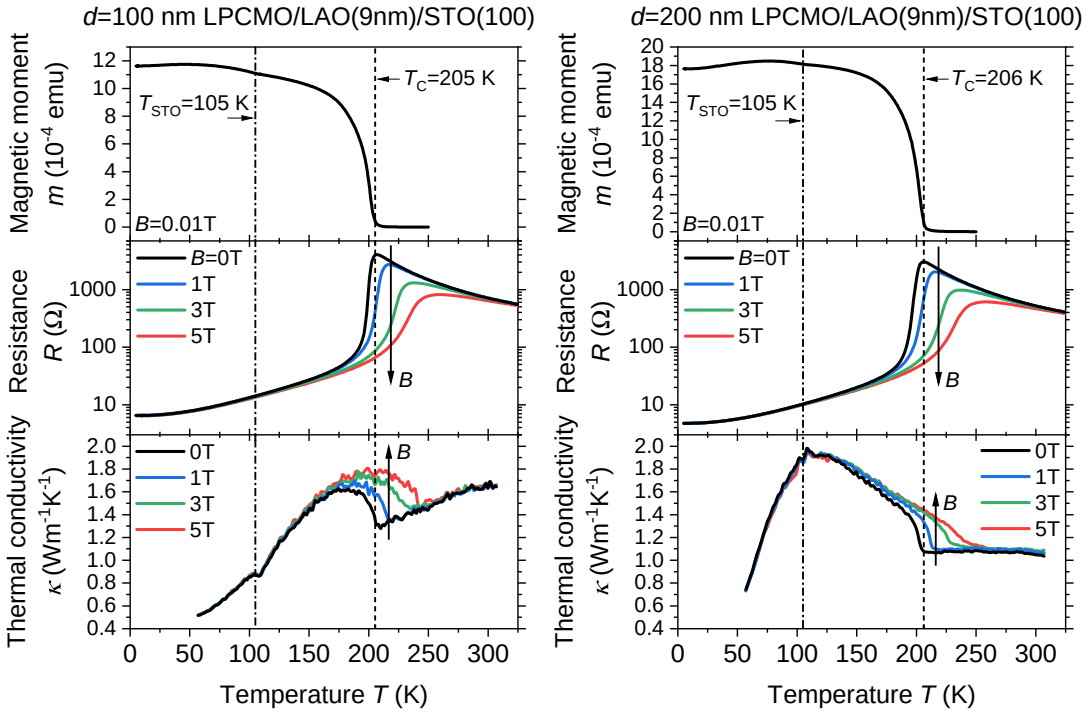

Fig. 7.3.1: Field cooled measurements of magnetic moment, electrical resistance and thermal conductivity of LPCMO/LAO/STO(100) thin films with thicknesses of $d = 100$ nm (left) and 200 nm (right) respectively. The dashed lines mark the Curie temperatures T_C of the films, whereas the dot-dashed lines mark the temperature of the cubic-tetragonal transition of the STO substrate at $T_{STO} = 105$ K.

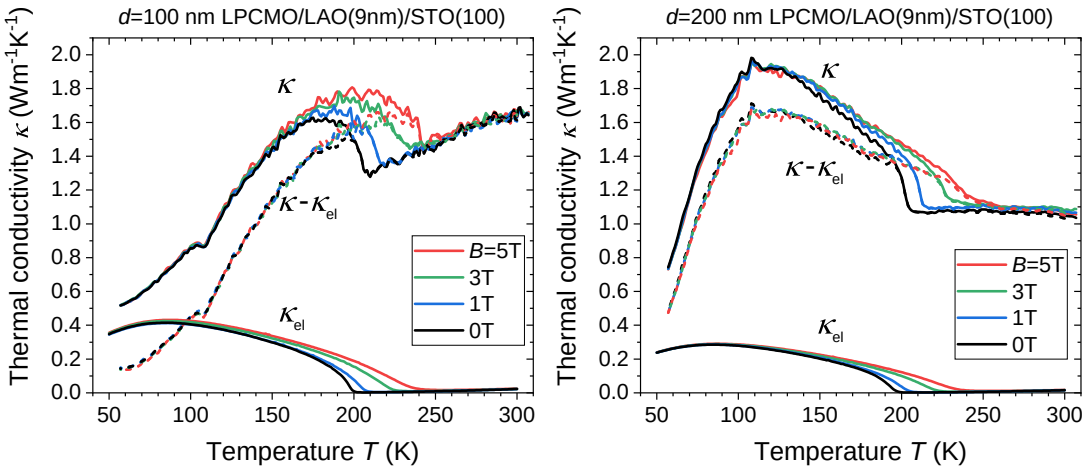

Fig. 7.3.2: Magnetic field cooled measurements of the thermal conductivity of LPCMO/LAO/STO(100) thin films with thicknesses of $d = 100$ nm (left) and 200 nm (right) respectively. The electronic contribution to thermal conductivity κ_{el} according to the Wiedemann-Franz law is shown along with a subtraction from the total measured thermal conductivity κ of the LPCMO films (dashed lines).

samples on MgO(100) which can be related to the stress-free growth without misfit dislocations and possibly slightly different oxygen octahedral tilting as compared to the samples on MgO(100), cf. [112]. Second, the STO substrate undergoes a cubic-tetragonal transition at $T_{\mathrm{STO}} = 105$ K, which marginally affects the magnetic and thermal properties at this temperature manifesting itself in small kinks in the temperature dependencies. This is in line with a report on this structural change of STO that affects the morphology and magnetism of an epitaxially grown CMR manganite LSMO [121]. Third, the 200 nm thick LPCMO sample exhibits a thermal conductivity maximum around $T = 100$ K with a thermal conductivity of $\kappa_{200\mathrm{nm}}(110\,\mathrm{K}) \approx 2\ \mathrm{Wm^{-1}K^{-1}}$ which is much higher than those of other LPCMO samples on both substrates in this temperature region ($\kappa_{<200\mathrm{nm}} \lessapprox 1.2\ \mathrm{Wm^{-1}K^{-1}}$), additionally having a pronounced temperature dependence of $\mathrm{d}\kappa_{200\mathrm{nm}}/\mathrm{d}T < 0$ between 100 K $< T <$ 200 K. The latter is typically found in bulk crystalline materials at high temperatures due to Umklapp scattering, cf. [75]. Indeed, this different thermal conductivity behavior dependent on film thickness can be attributed to the thickness-dependent boundary scattering, as the reduced dimensionality generally leads to reduced thermal conductivity of thinner films, cf. [75, 122, 123]. The 200 nm sample therefore most likely marks the thickness threshold of a transition to bulk-like properties because its thermal conductivity values approach literature values for bulk and the temperature dependence is

similar to bulk LPCMO with comparable doping level reported for example by Kim et al. [124].

Analogously to LPCMO/MgO(100) presented in previous section, the electronic contribution to thermal conductivity within LPCMO/LAO/STO(100) thin films (Fig. 7.3.2) is not sufficient to explain the increase below T_C or the strength of the MTC. Therefore, the same discussion as was made previously for the LPCMO/MgO(100) samples is also applicable here.

7.4 Discussion on magneto-thermal conductivity of LPCMO thin films

General discussion on temperature- and magnetic field-dependent 3ω measurements

The results demonstrate that the developed 3ω-PPMS extension is capable of measuring magnetic field dependent thermal conductivity of thin films in a wide temperature range of approximately 50 K $\leq T \leq$ 400 K. For temperatures below 50 K, a heater element with pronounced temperature dependence of electrical resistance would be necessary to detect a temperature oscillation, since simple metals like gold or platinum, usually used as heater/thermometer for 3ω measurements, approach a constant residual resistance at low temperatures. One possibility to achieve reasonable temperature dependence of resistance at low temperatures would be using a material exhibiting the Kondo-effect ([125]) like iron-alloyed copper [126] or (V-Cr)Fe alloys [127], as this approach was similarly suggested for steady-state measurement techniques [128]. Further, the use of temperatures above $T > 400$ K is restricted here by the PPMS setup arriving at its maximal temperature range. The title of the original publication by Cahill [81] advertises the 3ω method to work up to 750 K. The increase of temperature would only require temperature stability of the sample and the heater/thermometer (as well as the setup itself). Still, at high temperatures one should keep the radiation losses scaling with $\sim T^3$ in mind, cf. [82].

To account for the additional DC Joule heating, the constant temperature rise at the electric power used in this thesis for 3ω measurements ($P_{\mathrm{rms}} \approx 40$ mW

at $I_{1\omega,\mathrm{rms}} = 50$ mA) was estimated from the temperature shift compared to a measurement at a lower power ($P_{\mathrm{rms}} \approx 0.4$ mW at $I_{1\omega,\mathrm{rms}} = 5$ mA). The estimated temperature offset amounts to approximately $\Delta T \approx 7$ K and was taken into account in temperature measurements since the PPMS cryostat only controls the temperature of the sample holder.

Further, the contribution of the LAO buffer within the buffered LAO/STO(100) samples to the measured total thermal resistance can be neglected due to the similarity of its thermal conductivity to the substrate, cf. [129].

Unfortunately, due to water condensation within the cryostat disturbing the 3ω signal, the dataset of $\kappa(T, B = 5\,\mathrm{T})$ measurement of the $d = 51$ nm LPCMO/MgO(100) sample above $T \geq 0$°C needed to be ignored. Further, the measurement noise of the LPCMO electrical resistivity measurements was reduced by smoothing the data with the plot program *Origin*.

Discussion on thermal and magneto-thermal conductivity of LPCMO thin films

All in all, the results on thermal conductivity and MTC of LPCMO thin films on different substrates with different strain states are qualitatively comparable to bulk polycrystalline LPCMO reported in literature by Inyushkin et al. [117] or Kim et al. [124] (and are also qualitatively similar to bulk LCMO reported by Cohn et al. [118]), although the doping levels are slightly different. The main difference lies in the temperature dependence of thermal conductivity at low temperatures with reduced values for thin films below 200 nm measured here as compared to literature polycrystalline bulk values. This behavior occurs most probably due to the boundary scattering of phonons reducing the mean free path when the film thickness is decreased, cf. [75]. This also means that the use of the differential 3ω technique as it was used for measuring thermal conductivity of am-Al_2O_3 thin films (Section 6.3) which allows for distinguishing between interfacial resistances and the intrinsic thermal conductivity of the material, is not applicable in the case of LPCMO, at least within film thicknesses used in this thesis (50 nm $< d <$ 200 nm). For differential 3ω the thermal conductivity needs to scale linearly with film thickness, cf [82]. Due to this, the thermal conductivity measurements of LPCMO in this work include the interfacial resistances which leads to an underestimation of its thermal conductivity compared to the intrinsic value. Still, the values correctly

represent the thermal conductivity of the whole sample as a thermal device. This might explain the slightly higher thermal conductivity of LPCMO/LAO/STO(100) with coherent epitaxy (cf. [112]) compared to LPCMO/MgO(100), because the latter include semi-coherent misfit dislocations at the interface (cf. [49]) and most probably leads to a higher thermal boundary resistance, since for example similar semi-coherent misfit dislocations in GaN/AlN interfaces were theoretically predicted to strongly reduce the thermal boundary conductance [130].

Comparing the LPCMO films on different substrates used here is therefore difficult, also because the thicknesses of the films are not equal, and the properties of the films are apparently strongly thickness dependent. The fact that the interfacial resistances within both strain types of the used substrates are unknown and because they are included in the thermal conductivity measurements makes the comparison even more challenging. In order to address this problem, further (much thicker) samples should be measured to get a linear correlation of the thermal properties with the thickness in order to use the differential 3ω evaluation.

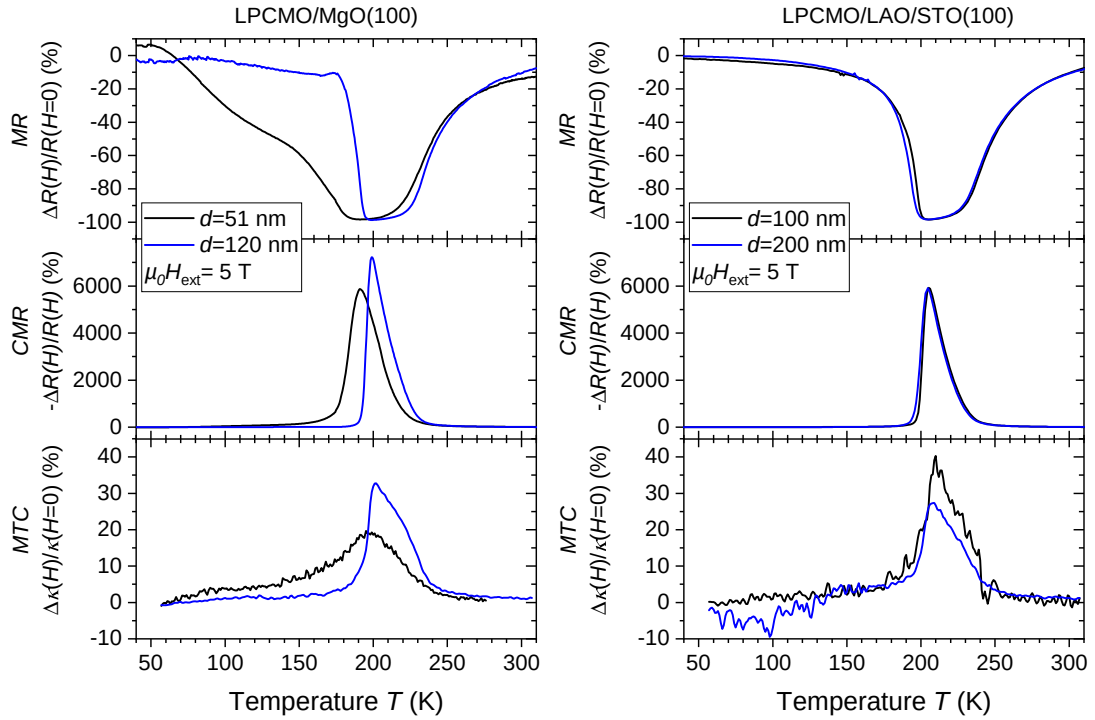

Fig. 7.4.1: Magnetic field dependent changes of electrical resistivity (within different definitions of magnetoresistance MR and colossal magnetoresistance CMR) as well as magneto-thermal conductivity (MTC) of LPCMO/MgO(100) (left) and LPCMO/LAO/STO(100) (right) thin films when applying an external magnetic field of $B = 5$ T.

Fig. 7.4.1 shows an overall comparison of the external magnetic field induced changes of the electrical resistance (MR and CMR) and thermal conductivity (MTC) after applying a field of $B = 5$ T. All films measured here show strong interconnections between the magnetic field dependencies of thermal and electronic properties with maximum changes in the vicinity of $T_C \approx 200$ K. Such behavior is discussed in literature to originate from changes of the static crystal defects like Jahn-Teller and oxygen octahedral distortions affected by magnetic fields or the paramagnetic-ferromagnetic transition which in turn is coupled to electrical mobility, cf. [115, 116, 118, 119, 131].

The extended occurrence of MTC at low temperatures within the $d = 51$ nm LPCMO/MgO(100) sample (that can also be seen in the temperature dependent thermal conductivity measurements of Fig. 7.2.1) falls together with the pronounced magnetoresistance at lower temperatures which is not present in thicker samples. This is most likely because the thinner sample exhibits a lower-T_C phase within the sample probably due to the stress relief region at the interface to the highly mismatched MgO(100) substrate. For thicker sample on MgO(100) this effect might become negligible due to the higher volume ratio of the predominant unstressed film with bulk-like electric properties.

The different field dependencies of thermal conductivity of the samples on MgO(100) with $MTC(d_{\mathrm{LPCMO}} = 51\ \mathrm{nm}) \leq 20\,\%$ and $MTC(d_{\mathrm{LPCMO}} = 120\ \mathrm{nm}) \leq 33\,\%$ coincide with the different CMR values of the films ($CMR(d_{\mathrm{LPCMO}} = 51\ \mathrm{nm}) \leq 5800\,\%$ vs. $CMR(d_{\mathrm{LPCMO}} = 120\ \mathrm{nm}) \leq 7200\,\%$) and the respective onset temperatures indicating their strong interconnection.

Regarding the samples on buffered LAO/STO(100) substrates, the percentual electrical resistivity changes after applying an external magnetic field are almost the same ($CMR(d_{\mathrm{LPCMO}} = 100\ \mathrm{nm}) \approx CMR(d_{\mathrm{LPCMO}} = 200\ \mathrm{nm}) \leq 5900\,\%$), whereas thermal conductivity changes are slightly different ($MTC(d_{\mathrm{LPCMO}} = 100\ \mathrm{nm}) \leq 40\,\%$ vs. $MTC(d_{\mathrm{LPCMO}} = 200\ \mathrm{nm}) \leq 27\,\%$). This might be caused by different boundary scattering and different defect densities of the films that influence electrical and thermal properties differently. Also the temperature dependence of thermal conductivities of both films strongly differ (Fig. 7.3.1), which can be another reason for the difference in MTC.

Still, the order of magnitude and the values of MTC of LPCMO thin films studied here are comparable to other reports of bulk manganites in literature being in the range of $MTC \approx 15\,\% - 50\,\%$ [115, 132].

Concluding, the measured magnetic field dependent thermal conductivity of LPCMO showed a strong interconnection with electrical transport and magnetism with a pronounced magneto-thermal conductivity up to $\Delta\kappa(\mu_0 H{=}5\text{ T})/\kappa(0) \approx 40\%$ for the d=100 nm LPCMO/LAO/STO(100) sample in the vicinity of the Curie temperature $T_\mathrm{C} \approx 205$ K. This can be explained by the reduction of crystal symmetry both below T_C or after applying a magnetic field in the vicinity of T_C, in addition to the electronic contribution according to the WF law within the framework of colossal magnetoresistance. The structural change most likely involves the reduction of local or extended crystal defects like Jahn-Teller defects and oxygen octahedral distortions (cf. [115, 116, 118, 119, 131, 133]) which can effectively reduce phonon scattering rates by affecting the acoustic modes of the phonon dispersion (main heat transport channel of the lattice) of perovskite oxides, cf. [120]. Raman measurements by Merten et al. [134] on similar LPCMO/MgO(100) thin films prepared similarly by metalorganic aerosol deposition additionally support the role of the involved structural polaronic Jahn-Teller vibrational distortions that are suppressed by decreasing temperature below T_C or by magnetic fields in the vicinity of T_C leading to a temperature or magnetic field-induced disorder-order transition.

8 Magnetism and magneto-thermal conductivity in exchange-spring-coupled manganites

This chapter consists of the published manuscript "Magnetism and Thermal Transport of Exchange-Spring-Coupled $La_{2/3}Sr_{1/3}MnO_3/La_2MnCoO_6$ Superlattices with Perpendicular Magnetic Anisotropy" [135] by Vitaly Bruchmann-Bamberg[1)], Isabell Weimer[1)], Vladimir Roddatis[2)], Ulrich Ross[3)], Leonard Schüler[1)], Karen P. Stroh[1)] and Vasily Moshnyaga[1)], *Nanomaterials* 13(21), 2897, 2023.

Affiliations: 1) Erstes Physikalisches Institut, Georg-August-University Göttingen, Friedrich-Hund-Platz 1, 37077 Göttingen, Germany;
2) Helmholtz Centre Potsdam, GFZ German Research Centre for Geosciences, Telegrafenberg, 14473 Potsdam, Germany;
3) IV. Physikalisches Institut, Georg-August-University Göttingen, Friedrich-Hund-Platz 1, 37077 Göttingen, Germany.

The manuscript bibliography was integrated into the current bibliography. Supplementary materials (SM) can be found in Appendix A.3 from p. 107 onwards. The listing of author contributions can be found at the end of the chapter. Some minor layout changes were made and remarks were added.

Abstract

Superlattices (SLs) comprising layers of a soft ferromagnetic metal $La_{2/3}Sr_{1/3}MnO_3$ (LSMO) with in-plane (IP) magnetic easy axis and a hard ferromagnetic insulator La_2MnCoO_6 (LMCO, out-of-plane anisotropy) were grown on $SrTiO_3$ (100)(STO) substrates by a metalorganic aerosol deposition technique. Exchange spring magnetic (ESM) behavior between LSMO and LMCO, manifested by a spin reorientation transition of the LSMO layers towards perpendicular magnetic anisotropy below $T_{SR} = 260$ K, was observed. Further, 3ω measurements of the $[(LMCO)_9/(LSMO)_9]_{11}$/ STO(100) superlattices revealed extremely low values of the cross-plane thermal conductivity $\kappa(300\ K) = 0.32\ Wm^{-1}K^{-1}$. Additionally, the thermal conductivity shows a peculiar dependence on the applied IP magnetic field, either decreasing or increasing in accordance with the magnetic disorder induced by ESM. Furthermore, both positive and negative magnetoresistance were observed in the SL in the respective temperature regions due to the formation of 90°-Néel domain walls within the ESM, when applying IP magnetic fields. The results are discussed in the framework of electronic contribution to thermal conductivity originating from the LSMO layers.

8.1 Introduction

Mixed valence perovskite manganites with general chemical formula $A_{1-x}A'_xMnO_3$ and double perovskites $A_2BB'O_6$ (here, A = La, Sr; B = Mn, Co) belong to the family of strongly correlated transition metal oxides. Their hallmark is a strong coupling between charge, spin, and lattice degrees of freedom, which results in super- and double-exchange (SE and DE) mechanisms of orbital interactions [29, 54]. The variety of magnetic ordering, i.e., para-(PM), ferro-(FM), and anti-ferromagnetic (AFM) accompanied by metal-insulator and/or charge ordering transitions, can be effectively influenced via bandwidth or band-filling controls, i.e., by means of chemical pressure or hole doping. Moreover, the external control parameters, like temperature, hydrostatic pressure as well as applied magnetic and electric fields were found to strongly influence the phase transitions [136]. A unique field-induced phenomenon found in this material class is colossal magnetoresistance (CMR) or a magnetic field-induced insulator-metal transition [52–54]. Perovskite manganites have drawn great and continuous interest for basic

and applied research in spintronics, multiferroics, catalysis, optoelectronics, and thermoelectricity [137–141].

Combining materials in superlattices (SL) has proven to be a fruitful pathway in the search for advanced functionality, leading to the discovery of a wide range of novel material properties not akin to the parent systems [67–69]. Magnetic SLs exhibit remarkable phenomena such as giant magnetoresistance (GMR) or tunnel magnetoresistance (TMR) and are nowadays widely used in sensing and information storage technologies. Perpendicular magnetic anisotropy (PMA) plays a crucial role in the increase of storage density in hard drives [18, 142]. To achieve PMA in manganites, like LSMO, orbital and strain engineering approaches via the choice of appropriate substrates [58], buffer layers [64], or interfaces [63] have been suggested. These strategies are based on the promotion of a preferred occupation of the $3z^2$-r^2 orbital, which favors PMA through spin-orbit coupling [60].

Another possibility to realize PMA in a soft FM with in-plane (IP) magnetic anisotropy is a direct-exchange coupling to a hard FM-possessing PMA [72]. Generally, exchange-coupled heterostructures or SLs of hard and soft FMs form the magnetic exchange spring (ESM) [21, 70, 71, 143, 144], which enables a gradual rotation or torsion of magnetic moments within the soft FM layers under applied small/moderate magnetic fields. The magnetic moments of the hard FM remain unchanged, thereby creating a spring-like reversible twist of the soft magnetic moments. This phenomenon occurs as long as the applied fields do not exceed the coercive field of the hard FM, ensuring its remanence. The interface spins of the soft FM remain effectively pinned by exchange coupling to the hard layers form a magnetic spring with a spin structure that resembles a domain wall [145, 146]. It was shown that magnetoresistance (MR) can originate from the field-induced domain-wall-like twisted spin disorder in ESM NiFe/CoSm bilayers [145], and it was also found in intrinsic domain walls in LSMO nanowires [147].

However, knowledge of the electronic and thermal properties of ESM-coupled layers in manganite-based SLs is scarce [63]. Moreover, to the best of our knowledge, the thermal conductivity of ESM-coupled SLs and the influence of magnetic fields on it have not been studied. In general, thermal conductivity in isolating crystals is mainly based on phononic heat transport, which is affected by crystal symmetry, impurities, and other structural defects or distortions. The additional contribution of free-charge carriers to thermal conductivity in metals and highly

doped semiconductors can be calculated using the Wiedemann-Franz (WF) law $\kappa_{el} = \sigma_{el} \times L \times T$ [79], with electrical conductivity σ_{el}, temperature T, and the Lorenz number $L = \pi^2/3(k_B/e)^2 = 2.45 \times 10^{-8}$ Ω W/K^2. However, in non-degenerate semiconductors as well as in strongly correlated or otherwise complex systems, the Lorenz number is not constant and can vary with temperature [148]. This makes the precise disentanglement of lattice and electronic contributions to thermal transport challenging. Still, the change of thermal conductivity in an external magnetic field, dubbed as "magneto-thermal conductivity" [132] and denoted as $MTC = [\kappa(B \neq 0) - \kappa(B = 0)]/\kappa(B = 0)$, can be observed in magnetoresistive materials due to the variation of their electrical conductivity dependent on a magnetic field [115, 149–153].

Here we report an ESM coupling between LSMO and LMCO within $[(LMCO)_n/(LSMO)_n]_m$ SLs epitaxially grown on STO(100) substrates via a metalorganic aerosol deposition (MAD) technique (see Methods section for details). Such an exchange spring with PMA, dictated by the hard magnetic LMCO layers, strongly impacts the electrical and thermal transport properties of SLs through magnetic field control of spin order/disorder. The results obtained highlight an attractive opportunity to study the spin-dependent scattering of charge carriers at domain-wall-hosting interfaces as well as to control the electromagnetic and thermal properties of SLs with a magnetic field.

8.2 Materials and Methods

8.2.1 Sample Preparation and Characterization

All oxide film samples were prepared by means of the metalorganic aerosol deposition (MAD) technique. Aerosols of the metalorganic precursor solution (acetylacetonates of the desired metals solved in N,N-dimethylformamide) have been sprayed through compressed air on a heated substrate. By using precise dosing units for liquid precursors as well as in situ growth control by means of optical ellipsometry [93], the single oxide films and heterostructures can be grown with monolayer accuracy. The substrate temperatures for growth of the crystalline oxide films were $T_{dep,cryst}$ = 900-950 °C and the deposition rate was v_{dep} = 0.1 nm/s. For amorphous growth, a temperature of $T_{dep,amorph}$ = 360

℃ with a deposition rate of $v_{dep} = 0.05$ nm/s was used. The STO substrates (*Crystal GmbH,* $10 \times 5 \times 0.5$ mm^3) were TiO_2 terminated based on an etching procedure [154] using an ammonium fluoride buffered hydrofluoric acid etchant and tempering for 1 h at $T = 965$ ℃ in the air to obtain a flat terrace morphology. The $[(LMCO)_n/(LSMO)_n]_m$/STO(100) SLs were grown with an overall thickness of around d ≈ 75 nm by varying the superlattice repetition number "m".

Four-probe electrical conductivity and magnetization measurements were carried out by Quantum Design GmbH (Darmstadt, Germany) PPMS and SQUID magnetometers MPMS XL and MPMS 3. The latter has been used for the rotator measurements (Standard rotator sample holder with $\alpha = 0°$ corresponding to the in-plane direction ($\alpha = 90°$ out-of-plane), samples were cut to 3×3 mm^2 to fit the holder).

The heater (150 nm thick Au layer grown on 5 nm thick Cr adhesion layer) for thermal conductivity measurements by the 3ω method was deposited by thermal evaporation (Cr) and magnetron sputtering (Au) followed by structuring with an optical lithography lift-off (Karl SUSS MJB4 (SÜSS MicroTec, Garching bei München) exposure unit, Allresist AR-P 5350 photoresist (Micro Materials Pty Ltd, Malvern Victoria, Australia). The dimensions of the heater line (width 2b = 25 µm, the length between the voltage leads l ≈ 1 mm) were measured by optical microscopy and additionally confirmed by scanning electron microscopy. To electrically decouple the metal heater from the analyzed and potentially conductive samples, insulating capping layers of amorphous alumina (am-Al_2O_3) were used.

X-ray measurements were conducted with the Bruker Advance D8 (Ettlingen, Germany) diffractometer. X-ray reflectivity (XRR) was used to obtain the film thicknesses as well as the density of amorphous am-Al_2O_3 capping layers $\rho_{\text{am-Al2O3}}$ = 3.3(2) g·cm^{-3} from single film measurements after fitting with the *GenX* program [100].

Scanning Transmission Electron Microscopy (STEM) was performed using a Thermo Fisher Scientific (TFS) (Thermo Fisher Scientific, Waltham, MA, USA) Themis Z 80-300 (S)TEM operated at 300 kV, equipped with a TFS SuperX Energy Dispersive X-ray (EDX) detector and a Gatan Imaging Filter (GIF) Continuum 1065. The microscope was tuned for a sub-Angstrom resolution with a beam convergence angle of 21.4 mrad. Specimens for STEM were prepared with a lift-out

Focused Ion Beam technique using a TFS Helios G4UC dual-beam instrument. The octahedral tilt within the Mn-O layers was measured from iDPC-STEM images using the Atomap library for Python [155], by fitting 2D Gaussians to individual atom contrast features and evaluating the collection of atom positions regarding the tilt of the Mn-O bonds within the zone axis projection.

8.2.2 Measurements of Thermal Conductivity by the 3ω Method

The 3ω method is a well-established technique for measuring thermal conductivity, especially of thin films [81]. The home-built setup used here was built based on the original setup by Cahill. A metal stripe on top of the sample acts both as a heater and a thermometer. Sourcing AC (here using the Keithley 6221 (Tektronix UK Ltd., Berkshire, UK) current source) provides Joule heating of the metal line such that its temperature oscillates at a doubled frequency. Detecting the temperature oscillation via the calibrated temperature-dependent electrical resistance oscillation of the heater element is achieved by measuring the 3rd harmonic (3ω) AC voltage by lock-in amplification (here by Stanford Research Systems SR830, Sunnyvale, CA, USA). To suppress the dominant ohmic voltage drop, an in-situ hardware subtraction of a reference resistor with a low-temperature coefficient of resistance (Vishay Z201 foil resistor, Vishay Electronic GmbH, Selb, Germany) is realized by a voltage divider and instrumentation amplifiers (Texas Instruments INA103, Freising, Germany). The measured in-phase and out-of-phase 3ω voltage oscillations are then used to calculate the complex temperature oscillation of the metal heater.

The 3ω measurements have been carried out using the PPMS cryostat for temperature control. Continuous measurements of temperature-dependent temperature oscillations were performed at a cooling rate of 1 K/s with 3 s lock-in integration time at excitation angular frequencies of $\ln(\omega) = 5.5$ and 6, respectively.

Using an analytical expression for frequency-dependent temperature oscillation of a metal heater/thin film/substrate system derived by Borca-Tasciuc et al. [91], which was subsequently improved by the Olson, Graham, and Chen's thermal impedance model [92], allows for fitting the data to obtain both thermal diffusivity and thermal conductivity of the substrate as well as the thermal resistance of a film on

the substrate. Additional statistical evaluation for an estimation of the noise level of the raw 3-omega (voltage) signal has been also performed. Converting the signal to the temperature oscillation and subsequently calculating thermal resistance within the standard 3-omega evaluation procedure, results in an uncertainty of the thermal resistance of σ(R, thermal) = 2 × 10^{-10} m^2K/W. Using the LSMO sample as an example, the error propagation leads to a statistical random error for thermal conductivity of σ(kappa) = 0.02 $Wm^{-1}K^{-1}$, which corresponds to a 2-sigma limit of ~2%.

8.3 Results and Discussion

8.3.1 Structure and Microstructure of LSMO/LMCO Superlattices

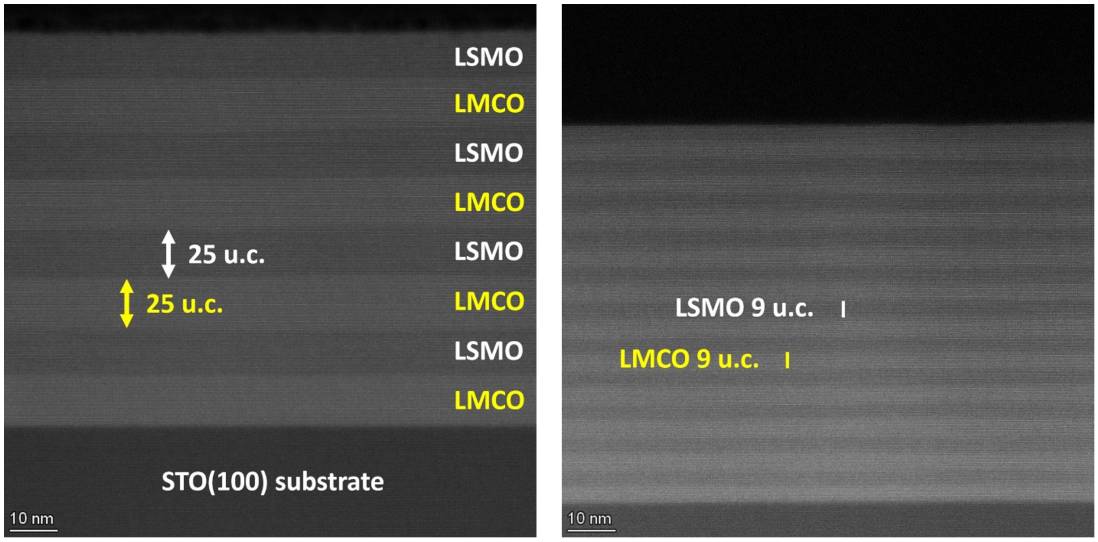

Fig. 8.3.1: High angular annular dark field (HAADF) scanning transmission electron microscopy (STEM) images of the representative $[(LMCO)_{24}/(LSMO)_{24}]_4$/STO(100) (**left**) and $[(LMCO)_9/(LSMO)_9]_{11}$/STO(100) (**right**) SLs.

The SL samples composed of LMCO and LSMO, i.e., $[(LMCO)_n/(LSMO)_n]_m$/STO(100), with layer thicknesses ranging from n = 1–24 unit cells (u.c.), were grown with SL repetition numbers m between 4 and 96 to ensure an overall thickness of d ≈ 75 nm for all samples. The structure and microstructure of the representative SLs with n = 9, 24 u.c. and m = 11, 4 are shown in Fig. 8.3.1. The

HAADF-STEM images reveal an epitaxial growth of LSMO and LMCO layers with regular repetition of the layers, each showing thicknesses close to the nominal ones. Moreover, the interfaces look sharp and flat in good agreement with the root-mean-square roughness of $S_q \approx 0.2$ nm for the n = 9 u.c. SL and $S_q \approx 0.5$ nm for the n = 24 u.c. SL, determined at the SL surfaces by means of atomic force microscopy (Fig. A.3.1, in Supplemental Material (SM). The small angle X-ray reflection (XRR) (see Fig. A.3.2 in SM) additionally confirms the thickness of individual layers to be close to the nominal values. Finally, X-ray diffraction (XRD) patterns evidence an out-of-plane epitaxy with c-axis lattice parameters within the range of $c \approx 0.3849$–0.3855 nm for both LMCO and LSMO layers (see Fig. A.3.2, SM) This is not very surprising given the similarity in pseudocubic bulk lattice parameters of LMCO and LSMO, both having values close to c ≈ 0.388 nm [30, 119] and sharing the same tensile stress state induced by the STO(100) substrate as well. One has to point out weak HAADF-STEM contrast between the LMCO and LSMO layers, having slightly differing composition at A-sites ($La/La_{0.7}Sr_{0.3}$) as well as very similar atomic masses of B-site cations, i.e., Co(59) and Mn(54). This makes the analysis of interfacial sharpness and intermixing at the atomic scale difficult. The additionally performed TEM chemical analysis of the $[(LMCO)_9/(LSMO)_9]_{11}$/STO(100) SL by using energy dispersive X-ray microanalysis (EDX) (see Fig. A.3.3, SM) has revealed a clear chemical contrast between LMCO and LSMO as well as detected Co/Mn intermixing at the interfaces with a thickness ~2 u.c. This is in line with XRR results.

8.3.2 Magnetic Exchange Spring in LSMO/LMCO Superlattices

In order to elaborate on the magnetic properties of $[(LMCO)_n/(LSMO)_n]_m$/ STO(100) SLs, we first introduce single films of LSMO/STO(100) and LMCO/STO(100). The optimally doped perovskite manganite $La_{0.7}Sr_{0.3}MnO_3$ (LSMO) is a well-known soft FM metal with an in-plane (IP) magnetic easy axis and magnetotransport properties governed by the DE interaction [156]. An almost 100% spin polarization at the Fermi level in the ground state [157] makes LSMO promising for spintronic applications. In Fig. 8.3.2(a), field-cooled IP and out-of-plane (OOP) magnetization measurements of a MAD-grown LSMO/STO(100) thin film with a thickness of d = 25 nm are shown, exhibiting a Curie temperature of $T_{C,LSMO} = 355$ K. Together with the rotator measurements of the

remanent magnetization (Fig. 8.3.2(b)) and measurements of magnetic hysteresis (Fig. A.3.4, SM), we conclude a soft FM behavior with an IP easy axis and a small coercive field $\mu_0 H_c(5\ \mathrm{K}) \approx 3$ mT in agreement with previous reports on LSMO/STO(100) thin films [158].

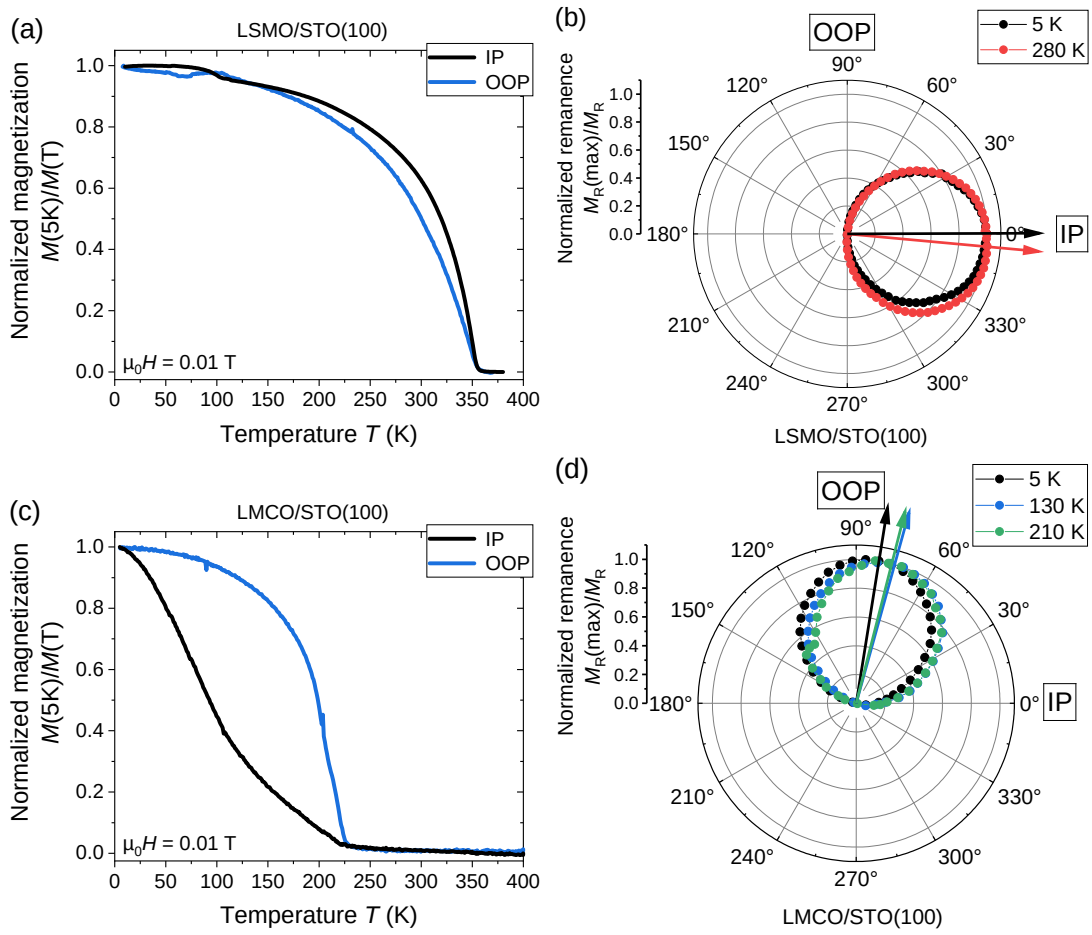

Fig. 8.3.2: Normalized field-cooled IP and OOP magnetization of (**a**) LMCO/STO(100) and (**c**) LSMO/STO(100) single films with thickness d = 25 nm and 40 nm, respectively. The respective polar plots (**b**,**d**) show the angle-resolved measurements of the normalized remanent magnetization. The arrows indicate the position of the easy axis.

The double perovskite La_2MnCoO_6 (LMCO) is an insulating hard FM characterized by an SE mechanism [30]. A MAD-grown LMCO/STO(100) film of d = 40 nm displays a high $T_C = 225$ K (Fig. 8.3.2(c)) and possesses a large coercive field of $\mu_0 H_c(5\ \mathrm{K}) \approx 1.1$ T (see Fig. A.3.3 [Remark by the Author: Fig. A.3.4], SM). These values, being comparable to those measured in the B-site ordered bulk material [30] and previously studied MAD-grown LMCO thin films [28, 159], evidence a right cation stoichiometry and an absence of oxygen deficiency, which

is known to suppress magnetism in rf-sputtered LMCO films [160]. In addition, our LMCO/STO(100) film possesses an OOP magnetic easy axis as verified by the angle-dependent measurements of remanent magnetization shown in Fig. 8.3.2(d). This observation agrees well with previous reports on LMCO/STO(100) films [33, 161]. Small deviations of the easy axes from the pure IP or OOP orientations in the presented measurements can either be explained by the competition between the crystal (OOP) and shape (thin film, IP) anisotropies or, most probably, they originate from an error of angle settings (here typically $\pm 5^\circ$).

Fig. 8.3.3(a) presents measurements of the IP magnetic moment of selected SLs, revealing an unusual magnetic behavior. Namely, the SLs with n = 9–24 u.c. show a spin reorientation (SR) transition at $T_{\mathrm{SR}} \approx 260$ K, at which the magnetic easy axis gradually changes towards PMA at low temperatures as evidenced by the temperature-dependent angle-resolved measurements of remanent magnetization, shown in Fig. 8.3.3(b) representatively for the SL with n = 9 u.c. SLs with very thin layers n = 1–6 u.c. (see Fig. A.3.5, SM) do not reveal the SR transition, which is probably caused by two reasons: (1) very thin LSMO layers become "magnetically dead", implying a significant reduction of $T_{\mathrm{C,LSMO}} < 200$ K when the LSMO thickness is reduced down to few unit cells [121, 162, 163] and (2) the Co/Mn intermixing (see Fig. A.3.3, SM) in very thin layers n = 1–3 u.c. leads to the formation of a mixed (La,Sr)(Co,Mn)O_3 with an unknown composition.

A similar magnetic PMA spin reorientation has been reported in heterostructures of perovskite LSMO and brown-millerite $LaCoO_{2.5}$ (B-LCO), i.e., $[(\mathrm{LSMO})_i/(\mathrm{B\text{-}LCO})_j]_m$/STO(100) heterostructures, by Zhang et al. [63]. They interpreted the SR based on the symmetry-mismatch-driven perovskite/brown-millerite interfacial elongation of the oxygen octahedra, which implies an orbital reconstruction of the Mn ions within the interfacial LSMO. Such reconstruction was suggested to change the magnetic easy axis of LSMO towards a PMA geometry. The magnetic contribution of the B-LCO was neglected due to the very low Curie temperature of a single B-LCO/STO(100) film, $T_{\mathrm{C,B\text{-}LCO}} \ll T_{\mathrm{SR}}$. Thus, they attributed the PMA observed in their SLs to the structural and orbital reconstruction, induced by the symmetry breaking at the perovskite/brown-millerite interface.

We have carried out measurements of both IP and OOP field-cooled magnetization under various external magnetic fields (Fig. 8.3.4) on the SL with n = 9 u.c., which has the highest interface density among the samples that exhibit the SR

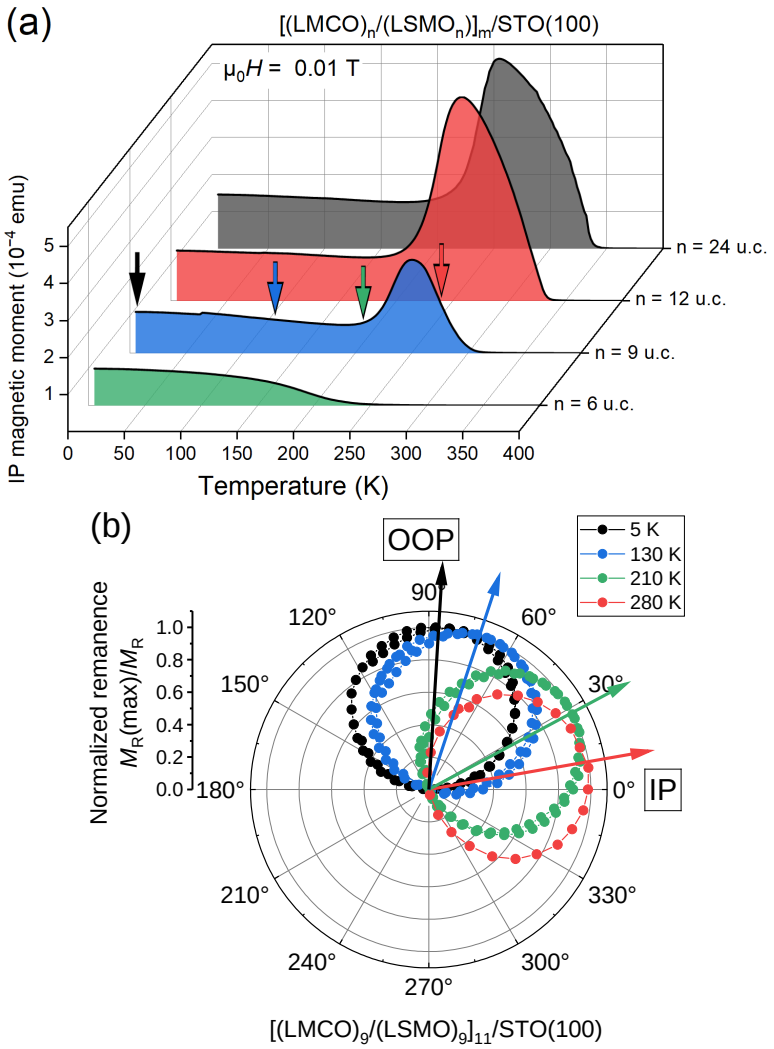

Fig. 8.3.3: (**a**) Field-cooled IP magnetic moment component of $[(LMCO)_n/(LSMO)_n]_m$/STO(100) SLs with different layer thicknesses n = 6, 9, 12 and 24 u.c. and bilayer numbers m = 16, 11, 8, 4, respectively. The arrows mark the temperatures used for the rotator measurements of normalized remanence of the n = 9 u.c. $[(LMCO)_9/(LSMO)_9]_{11}$/STO(100) SL (**b**), showing a change of magnetic anisotropy from an OOP to an IP direction around 250 K upon warming from 5 K to 280 K. Here the arrows indicate the apparent position of the easy axis.

transition. A similar behavior to that reported by Zhang et al. [63] has been observed, i.e., (1) IP spin reorientation for $T < T_{SR} \approx 260$ K; (2) saturation of the OOP magnetization at low temperatures for cooling fields $B \geq 0.2$ T; and (3) an IP-OOP crossover at lower fields and temperatures around 260 K. Note, that in contrast to Zhang et al. [63], our $[(LMCO)_n/(LSMO)_n]_m$/STO(100) SLs possess a perovskite/perovskite heteroepitaxy without any structural symmetry mismatch

at the interface as evidenced by high-resolution HAADF-STEM and iDPC-TEM measurements (see Fig. A.3.6 in SM). Evidently, the interfaces appear coherent and show no visible abrupt changes in the octahedral tilt/rotation angles.

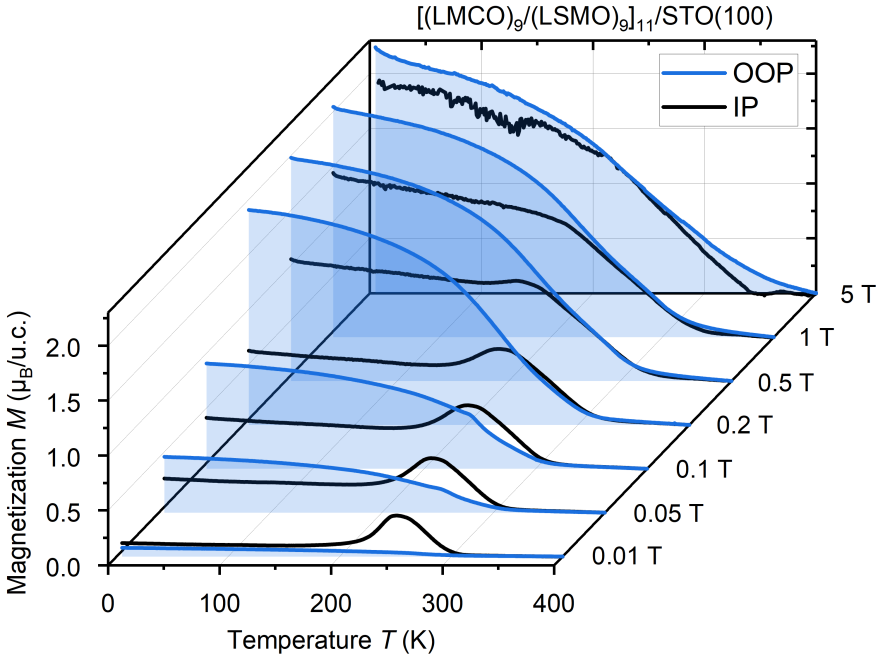

Fig. 8.3.4: IP and OOP field-cooled magnetization measurements of the n = 9 u.c. $[(LMCO)_9/(LSMO)_9]_{11}$/STO(100) SL in different magnetic fields.

According to our magnetization measurements, the observed spin reorientation in our SLs can more likely be explained by the interplay of different magnetic easy axes and strongly different coercive fields of LMCO and LSMO, leading to the formation of a "magnetic exchange spring" (ESM)-coupled heterostructure. The reduction of the IP magnetization of our SLs below T_{SR} would then be attributed to the OOP rotation of magnetic moments within the LSMO due to the exchange coupling to the hard magnetic LMCO with PMA. This would indeed require a slightly increased T_C of either the LMCO layer itself or, at minimum, its interfacial region near the layer LSMO, up to a value of $T_{C,SL\text{-}LMCO} \approx T_{SR} \approx$ 260 K within the SLs. An independent method for estimating the T_C of LMCO layers in SLs is provided by Raman spectroscopy measurements, which allow for measuring the spin-spin correlation induced anomalous shift of Raman lines in FM manganites due to spin-phonon coupling [164]. As one can see in Fig. A.3.7 (SM), the anomalous downshift of the dominating LMCO Raman line around 600 cm^{-1}, induced by the FM transition, indeed starts at $T_C \approx 260$ K, which is significantly larger than the $T_C = 225$ K of single LMCO films determined also by Raman

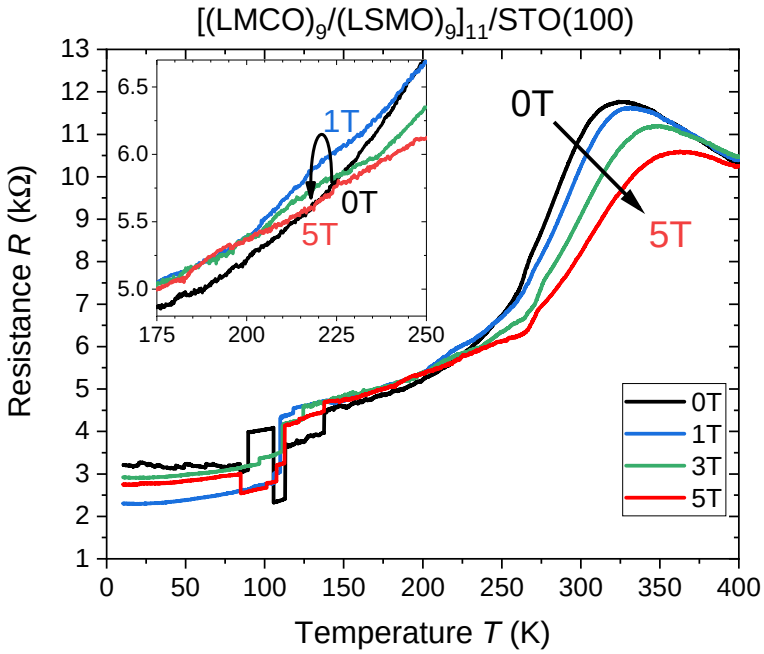

Fig. 8.3.5: Field-cooled electrical resistance vs. temperature of the $[(LMCO)_9/(LSMO)_9]_{11}$/STO(100) SL with both current and field applied in-plane. The inset shows the region with positive magnetoresistance.

spectroscopy [159]. Thus, thin (9–24 u.c.) LMCO layers in LMCO/LSMO SLs do have an enhanced T_C compared to single LMCO/STO films likely because of the reduced dimensionality and optimal interfacing with FM metallic LSMO layers.

Due to the orthogonality of the easy axes of the LSMO and LMCO layers, the formation of 90° Néel-type domain walls at the interfaces between the layers at low temperatures is favored. Such ESM made from the insulating LMCO and metallic/magnetoresistive LSMO counterparts should certainly give rise to a unique field-dependent electrical resistivity behavior. Temperature- and field-dependent electrical resistance measurements (current IP, field-cooled) of the n = 9 u.c. SL are shown in Fig. 8.3.5.

One can see a metal-insulator transition with a peak temperature around T_{MI} ≈ 320 K for $B = 0$ T and a maximal value of $CMR(300\ K)$ = -36%. This can be attributed solely to the LSMO, as current flow takes place only within the metallic LSMO. A similar $R(T)$ behavior is known for single LSMO/STO(100) films of comparable thickness and is reported elsewhere [165]. Below $T < 250$ K, especially in the region around $T \approx 220$ K, the resistance of the SL shows an increase with the magnetic field and magnetoresistance becomes positive

MR(220K, B=1 T) = +4.5 % for $0 < B < 5$ T (see inset in Fig. 8.3.5). This is in clear contradiction with the well-known negative CMR effect. Note, that at $T_{\mathrm{SR}} = 260$ K, the spin reorientation and the ESM formation set in, resulting in the field-induced spin disorder within the emergent Néel domain-wall, which is expected to increase the electron-spin scattering and thus the resistance of the LSMO. When nearly saturated ($B \geq 5$ T), the spin disorder vanishes as all spins are oriented IP, and the LSMO within the SL again follows its intrinsic negative CMR behavior.

Further, a strong decrease of the resistance below $T \approx 275$ K as well as the apparent stochastic resistance jumps below $T < 100$–150 K can be seen in Fig. 8.3.5. The former can be caused by the mutual ferromagnetic proximity, as the magnetic moment of the adjacent LMCO is also the source of an additional magnetic field and thereby able to cause a reduction of LSMO resistance due to CMR. The other aspect of resistance jumps at lower temperatures might be ascribed to domain-wall pinning and movement as well as creation or annihilation of magnetic domain wall boundaries within the ultrathin LSMO in field-cooled measurements, which is known to alter the resistance of nanoscale LSMO [147]. Upon warming, however, the resistance does not show any jumps, most likely indicating domain rotation rather than domain wall movement (see Fig. A.3.8, SM).

The observations mentioned above allow us to model the typical profile of a magnetic exchange spring within the LMCO/LSMO SL as sketched in Fig. 8.3.6. At temperatures $T_{\mathrm{C,LMCO}} < T < T_{\mathrm{C,LSMO}}$, the magnetic moments of the LSMO layers lie along their respective IP easy axis direction (Fig. 8.3.6(a)). As the temperature falls below $T < T_{\mathrm{C,LMCO}}$ and the LMCO becomes OOP ferromagnetic, the exchange coupling at the interface forces the LSMO to rotate OOP, thus favoring Néel-type domain walls at the interfaces (Fig. 8.3.6(b)). By increasing the IP magnetic field, the magnetic moments of the LSMO reorient back to the IP direction (d), followed by saturation of the entire SL when the applied magnetic field exceeds the coercive field of the LMCO (e).

8.3.3 Magneto-Thermal Conductivity of LSMO/LMCO SL

To analyze the temperature and magnetic field behavior of thermal conductivity $\kappa(T, B)$ in LSMO/LMCO SLs, we first measured the cross-plane thermal conduc-

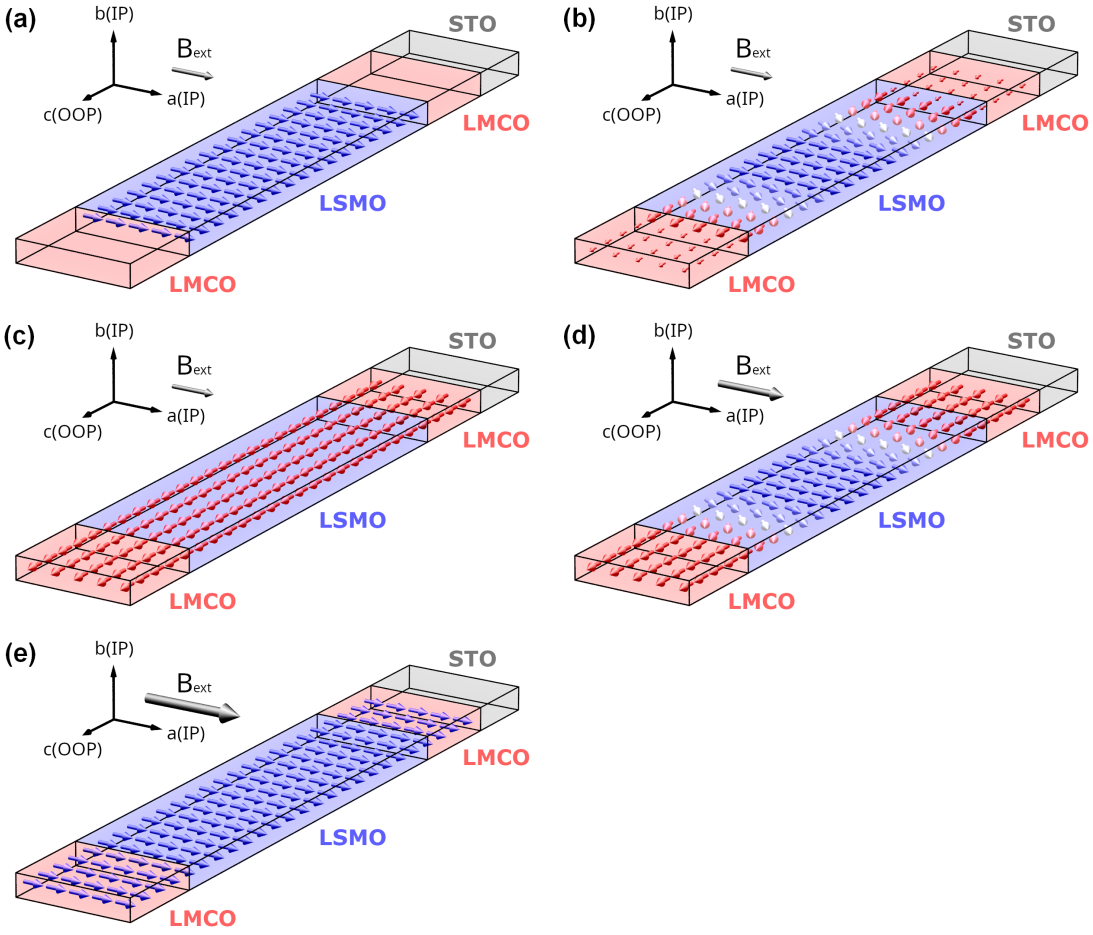

Fig. 8.3.6: Schematic illustrations of the temperature- and magnetic field-dependent magnetic profile within an ESM in $[(LMCO)_n/(LSMO)_n]_m/STO(100)$ SLs: (**a**) $T_{SR} < T < T_{C,\,LSMO}$ (**b**) PMA of the constituent layers leading to the formation of 90° Néel domain walls for $T < T_{SR}$ and low IP fields; (**c**) for $T \ll T_{SR}$ and low IP fields the IP magnetic moment is vanishingly small, and (**d**) reorientation of LSMO spins back to IP for $T \ll T_{SR}$ and increasing IP field; (**e**) Model for SLs in the saturated state, at high IP magnetic fields exceeding the H_C of LMCO.

tivity of the constituting single films LSMO/STO(100) and LMCO/STO(100). The data on $\kappa(T, B)$ are shown in Fig. 8.3.7. One can see that, throughout the measured temperature range, the thermal conductivity of the LSMO film either remains unchanged or increases under an applied magnetic field. This can be quantified by a positive magneto-thermal conductivity (MTC), which can be as large as $MTC(360\ \mathrm{K}) = 100\% \times (\kappa(\mathrm{B}) - \kappa(0))/\kappa(0) = +17\%$ at $B = 5\mathrm{T}$. This value is definitely outside of the 2σ limit of ~2% (see Methods), making the $MTC = 17\%$ reasonable. Note that this MTC is confined to a relatively narrow temperature window close to $T_{\mathrm{C,LSMO}}$ and seems to correlate with the CMR effect: Positive MTC values can be explained by a CMR-related field-induced increase of electrical conductivity in the LSMO film thereby increasing the electronic contribution to thermal conductivity and thus enabling MTC. However, an estimation of the pure electronic part of thermal conductivity by using the WF law accounts only for a small fraction of the total measured MTC (see Fig. A.3.8, ref. [153] [Remark by the author: Fig. A.3.9 (SM)]). Note, that the WF law, more or less satisfactorily describing the behavior of conventional metals and failing already for more complex semiconducting [148] and nanocrystalline metallic [166] systems, must not be applicable for strongly correlated electron systems, i.e., LSMO. This probably indicates that other possible magnetic field-induced changes of (a) heat capacity; (b) magnons; (c) oxygen octahedral tilt angles, and d) Jahn-Teller disorder [115, 116] might contribute to MTC, but they are difficult to disentangle into separate contributions.

Double perovskite LMCO films on STO(100) with a monoclinic structure possess a higher degree of octahedral tilting (Mn-O-Co angle of $\varphi_{\mathrm{LMCO}} = 154°$ (ref. [161]), as compared to that in rhombohedral LSMO/STO(100) (Mn-O-Mn angle $\varphi_{\mathrm{LSMO}} = 168°$ (ref. [163]). In addition, the insulating behavior of the cation-ordered LMCO due to superexchange and the doubled unit cell led to a significantly lower thermal conductivity compared to that in LSMO (Fig. 8.3.7). Further, no influence of magnetic field on thermal transport in LMCO is observable, which fits the absence of the CMR effect in Co/Mn-ordered double perovskites [167]. Finally, one can see in Fig. 8.3.7 a clear peak in the thermal conductivity of LMCO around $T = 105$ K, i.e., close to the temperature of the structural (cubic-tetragonal) phase transition of the STO substrate. Considering the epitaxial character of LMCO/STO films and strong elastic coupling to the substrate, this peak in $\kappa(105\ \mathrm{K})$ can be ascribed

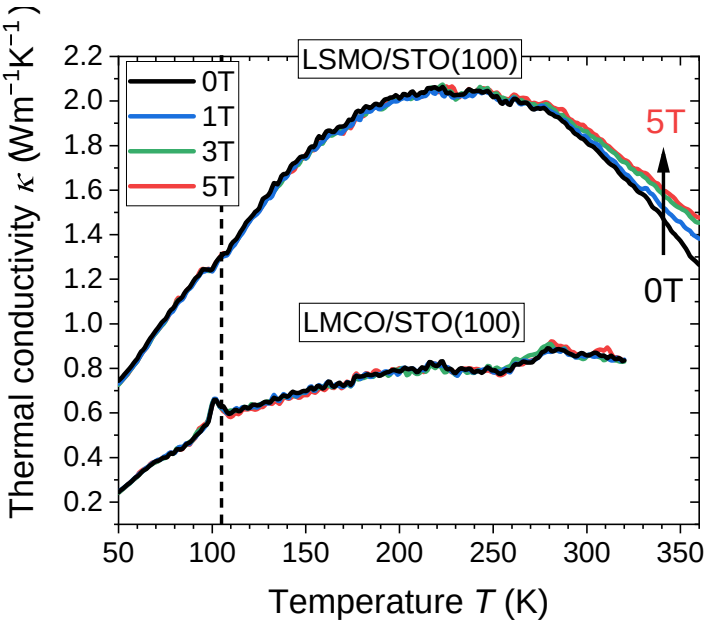

Fig. 8.3.7: Temperature dependencies of the field-cooled cross-plane thermal conductivity of LSMO/STO(100) and LMCO/STO(100) single films with the thicknesses $d = 100$ nm and 25 nm, respectively, in applied in-plane magnetic fields, $B =$ 0–5 T. The dashed line marks the position of the cubic-tetragonal transition of the STO substrate, $T_{\mathrm{STO}} = 105$ K.

to a change in the LMCO strain state due to the structural phase transition in the STO substrate.

The temperature and magnetic field dependence of the cross-plane thermal conductivity of the $[(\mathrm{LMCO}_9)/(\mathrm{LSMO})_9]_{11}$/STO(100) SL is presented in Fig. 8.3.8. Remarkably ultralow thermal conductivity $\kappa_{\mathrm{SL}}(300\ \mathrm{K}) = 0.32\ \mathrm{Wm^{-1}K^{-1}}$ has been obtained in this SL sample in zero field. Similar values were reported in the literature for bulk samples of all-inorganic vacancy-ordered double perovskites (e.g., $\kappa_{\mathrm{Cs2SnI6}}$ (295 K) = 0.29 $\mathrm{Wm^{-1}K^{-1}}$ (ref. [168]), Ruddlesden-Popper perovskites (e.g., $\kappa_{\mathrm{Cs2PbI2Cl2}}$ (295 K) = 0.37 $\mathrm{Wm^{-1}K^{-1}}$ (ref. [169]), or chalcogenides like Ag_2Se (κ_{Ag2Se} (300 K) = 0.29 $\mathrm{Wm^{-1}K^{-1}}$ (ref. [170]).

Considering the SL geometry with thermal resistances of LMCO and LSMO connected in series, the ultralow cross-plane thermal conductivity of the SL could, in principle, originate both from the LMCO and LSMO layers as well as from the LSMO/LMCO interfaces. Note, that both the LMCO and LSMO layers in the SL, being only 9 u.c. thick, could be much less thermally conducting than the LSMO and LMCO single films in Fig. 8.3.7. This is in line with the

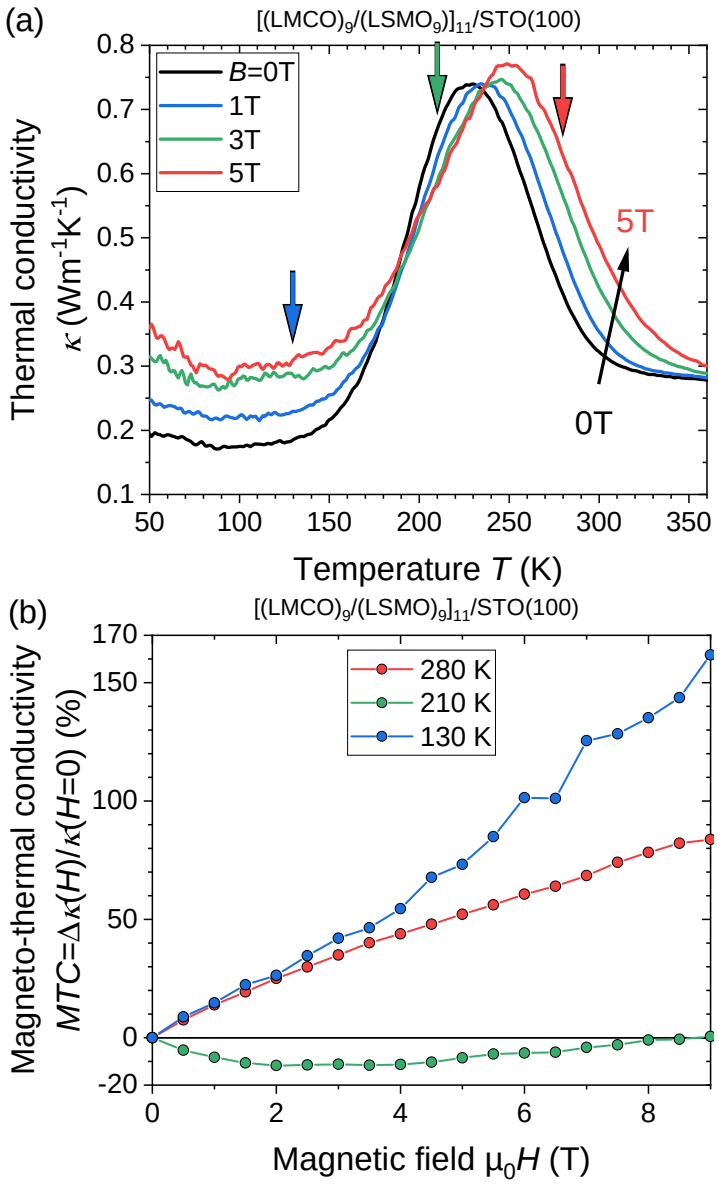

Fig. 8.3.8: (**a**) Field-cooled cross-plane thermal conductivity of the $[(LMCO)_9/(LSMO)_9]_{11}$/STO(100) superlattice in different applied in-plane magnetic fields. The arrows mark the temperatures used for the field-dependent magneto-thermal conductivity (MTC). (**b**) Field-dependent MTC of the $[(LMCO_9)/(LSMO)_9]_{11}$/STO(100) superlattice.

reduction and variation of oxygen octahedral rotation tilt angles determined from high-resolution iDPC images of the $[(LMCO_9)/(LSMO)_9]_{11}$/STO(100) SL shown in Fig. A.3.5 [Remark by the author: Fig. A.3.6] (SM). The obtained values for the Mn-O-Mn(Co) angles φ vary in the range of approximately $154° < \varphi < 160°$. Within the LMCO layers, the angles center at $\varphi_{\text{SL-LMCO}} \approx 154°$ which is similar

to bulk, while within the LSMO layers, the values reach $\varphi_{\text{SL-LSMO}} \approx 160°$, having a stronger tilt compared to the bulk LSMO with $\varphi_{\text{LSMO}} \approx 166°$ (ref. [119]). In between, the values smoothly change across the interfaces. We suspect that the observed modulations of the octahedral tilt angles along the growth direction and the stronger tilting of LSMO oxygen octahedra in the SL compared to bulk LSMO could be the origin of the ultralow thermal conductivity in the LSMO/LMCO SLs.

Two important features appear when applying an external magnetic field (Fig. 8.3.8): (1) A shift of the thermal conductivity peak to higher temperatures and (2) the emergence of an unexpected negative MTC within the temperature region 185 K < T < 235 K (see Fig. 8.3.8(a)). The shift of the thermal conductivity peak of the SL in applied fields towards higher temperatures can likely be explained by the shift of the magnetic (T_{C}) and electric (T_{MI}) transition temperatures towards higher values, which is common for perovskite FM manganites [171]. However, neither of the single manganite films has revealed a negative MTC. The field-dependent MTC of the n = 9 u.c. SL is shown in Fig. 8.3.8(b) for selected temperatures. One can see a minimum negative MTC reaching as low as $MTC(210\ \text{K}, 3\ \text{T}) \approx -11\%$. For stronger fields of 4 T < B < 9 T, the amplitude of the negative MTC decreases and even almost changes sign for $B = 9$ T. A possible explanation for the observed behavior is the field-induced spin disorder within the LSMO layers promoted by the ESM formation. The spin disorder affects the charge carrier mobility due to enhanced spin scattering (cf. Fig. 8.3.5(d) [Remark by the author: Fig. 8.3.6(d)]) and could thus result in a reduction of the electronic contributions to the thermal conductivity of the SL.

8.4 Conclusions

Superlattices of $La_{2/3}Sr_{1/3}MnO_3/La_2CoMnO_6$ (LSMO/LMCO) were epitaxially grown on $SrTiO_3(100)$ substrates using the metalorganic aerosol deposition technique. Their magnetic behavior was shown to be governed by perpendicular magnetic anisotropy, originating from magnetically hard double perovskite LMCO layers. An exchange-spring magnetic coupling between LSMO and LMCO layers was observed, leading to a spin reorientation transition of LSMO at $T_{\text{SR}} = 260$ K. Applied in-plane magnetic fields enable control of the degree of spin disorder through continuous spin rotation within the soft magnetic LSMO layers towards

their natural in-plane easy axis. Such field-controlled spin order/disorder was found to strongly influence both electrical and thermal transport in the SLs via spin-dependent scattering of charge carriers and their contributions to thermal transport in LSMO. The results obtained highlight the suitability of exchange-spring magnetic coupling within perovskite superlattices not only for achieving perpendicular magnetic anisotropy with nanoscale layer thicknesses down to ~9 u.c. (~3.5 nm) but also for controlling both electrical resistance and thermal transport using magnetic fields.

Author Contributions

Lead of the project: V.M. Conceptualization and design of the study: V.M. and V.B.-B. Sample preparation and characterization: V.B.-B., I.W., and K.S. Transmission electron microscopy: V.R. and U.R. Thermal conductivity measurements and evaluation: V.B.-B. Raman spectroscopy: L.S. Manuscript: V.B.-B. with revisions by V.M. and I.W. All authors discussed the results and contributed to the final manuscript. All authors have read and agreed to the published version of the manuscript.

Funding

This research was funded by German Research Foundation (DFG) within the CRC 1073 Projects A02 and Z02; DFG Projects MO-2255-4 and RO-5387/3-1, and International Center for Advanced Studies of Energy Conversion (ICASEC).

Acknowledgments

The authors acknowledge the financial support by the German Research Foundation (DFG) within the CRC 1073 Projects A02 and Z02. We thank D. Steil and T. Titze for fruitful discussions. VB and KS gratefully acknowledge the financial support from the International Center for Advanced Studies of Energy Conversion ICASEC. V.M. and V.R. acknowledge the financial support by the DFG via Projects MO-2255-4 and RO-5387/3-1, respectively. V.R. acknowledges the European Regional Development Fund and the State of Brandenburg for the Themis Z TEM (part of the Potsdam Imaging and Spectral Analysis Facility (PISA)). The use of equipment in the “Collaborative Laboratory and User Facility for Electron Microscopy” (CLUE) www.clue.physik.uni-goettingen.de (accessed on 02.11.2023) is gratefully acknowledged.

9 Summary, concluding discussion and outlook

Reports on thermal conductivity of thin manganite films and superlattices [172–174], especially on their magnetic field dependency [151], are scarce. The present thesis attended to this matter by using high quality MAD-grown manganite samples and implementing the 3ω thermal conductivity measurement technique to the *Quantum Design Physical Properties Measurement System* (PPSM) setup. For studying magnetic field dependent thermal conductivity of single thin films, the colossal magnetoresistive lanthanum praseodymium calcium manganite $(La_{0.6}Pr_{0.4})_{0.7}Ca_{0.3}MnO_3$ (LPCMO) was chosen because of already reporded magneto-thermal conductivity of bulk polycrystals in literature (e.g., [117]). For studying superlattices, lanthanum strontium/lanthanum cobalt manganite $La_{2/3}Sr_{1/3}MnO_3/La_2MnCoO_6$ (LSMO/LMCO) superlattices (SLs) were used because of their intriguing exchange-spring Néel-like magnetic behavior. To the best of my knowledge, such emerging spin structure was not yet studied in literature regarding its impact on thermal conductivity of strongly correlated materials.

Method developement for thin film thermal conductivity measurements in magnetic fields

Within this thesis, the 3ω method by Cahill [81] for thermal conductivity measurements of both bulk materials and thin films was successfully implemented into the PPMS setup allowing a temperature regulation from 2 to 400 K and external magnetic fields of up to 9 Tesla. The method involves the use of a metal heater element on the sample, which was patterned by an optical lithography lift-off technique using thermal evaporation of a chromium adhesion layer, followed by magnetron sputtering of gold. Using gold heater/thermometer element restricts the temperature range to only work above approximately $30 - 50$ K due to the

low temperature sensitivity of electrical resistance of gold (or metals in general) approaching a constant residual value at low temperatures. Moreover, when using electrically conducting samples, an insulating dielectric needed to be used to electrically separate the metal heater from the sample. Instead of using strontium titanate $SrTiO_3$ (STO) as it was used in a similar report on 3ω measurements on manganites by Thiessen et al. [173], the use of amorphous alumina am-Al_2O_3 was elaborated here using the metalorganic aerosol deposition technique (MAD). This capping choice ensures that the heat is not spread in-plane within the capping layer due to a higher thermal conductivity of STO ($\kappa_{\mathrm{STO}} \approx 10-20\ \mathrm{Wm^{-1}K^{-1}}$) compared to manganites, whereas the am-Al_2O_3 has comparable thermal conductivity values in the same order of magnitude like manganite thin films ($\kappa_{\mathrm{am\text{-}Al2O3}} \approx 0.4 - 2\ \mathrm{Wm^{-1}K^{-1}}$) in the measured temperature range.

For precise thermal conductivity measurements of thin films, also the used substrates and capping layers were measured by the same 3ω setup using the same parameters to ensure an appropriate subtraction not relying on literature values that might differ from the used materials due to different instrumentation or sample quality. Nevertheless, measured values are very similar to literature values. The deviations of the measured values listed in Tabs. 6.3.1 and 6.3.2 amounted to $\Delta\kappa(\mathrm{STO_{meas.}}/\mathrm{STO_{lit.}}) \approx -5\%$; $\Delta\kappa(\mathrm{MgO_{meas.}}/\mathrm{MgO_{lit.}}) \approx -7\%$ and $\Delta\kappa(\text{am-}\mathrm{Al_2O_{3meas.}}/\text{am-}\mathrm{Al_2O_{3lit.}}) \approx -9\%$ respectively, slightly underestimating the literature values.

Magneto-thermal conductivity of LPCMO thin films

The measured thermal conductivity of LPCMO thin films prepared by MAD on different substrates of unbuffered MgO(100) as well as $LaAlO_3$ (LAO) buffered STO(100) revealed a remarkable interconnected behavior of thermal conductivity with magnetism and electrical conductivity. The choise of the MgO substrate results in stress release by misfit dislocations whereas the LAO/STO enables an unstrained growth, cf. [49, 112]. A strong correlation of magnetism and electrical conductivity being highly dependent on external magnetic fields, also known as the colossal magnetoresistance CMR, is well known in literature and is explained by the double exchange model, additionally involving the phase separation of antiferromagnetically coupled ferromagnetic domains by correlated polarons in the case of LPCMO, cf. [49, 114]. Reports on thermal and magneto-thermal

conductivity of bulk polycrystalline LPCMO and similar magnetoresistive mixed-valence manganites in literature ([116, 117, 124, 131, 133], etc.) hold the static structural, e.g., Jahn-Teller and oxygen octahedral distortions responsible for both the low thermal conductivity values as well as the temperature and magnetic field dependencies coupled to electrical mobility and magnetism by the double exchange physics.

The results on thin LPCMO films obtained here are for the most part in line with reports on polycrystalline bulk LPCMO or similar manganite systems with only slight deviations that are generally attributable to the thin film geometry and epitaxy. Corresponding relevant effects include the interfacial Kapitza thermal resistances which become important when dealing with thin films as well as additional boundary scattering of low energy acoustic phonons when lowering the film thickness which affects thermal conductivity at low temperatures, cf. [75, 175]. All LPCMO samples measured here, except of the $d = 200$ nm sample on LAO/STO(100), showed reduced thermal conductivity values, especially deviating strongly at low temperatures, compared to reports on bulk polycrystalline LPCMO. Still, the $d = 200$ nm sample on LAO/STO(100) showed bulk-like thermal conductivity behavior, which fits to the reduced boundary scattering due to the increased dimensions most probably marking the thickness crossover to bulk-like thermal properties.

In order to experimentally support the hypothesis that the (magneto-)thermal conductivity of LPCMO is influenced by extended crystal defects like oxygen octahedral tilts (B-O-B angles) in LPCMO, temperature-dependent measurements of these angles would be necessary, which could be achieved by using high-resolution transmission electron microscopy (HR-TEM) with oxygen resolution via integrated differential phase contrast (iDPC) method at different temperatures. Furthermore, ab-initio molecular dynamic (aiMD) simulations and density functional theory (DFT) calculations in analogy to the report on theoretical calculations of thermal conductivity in STO [120] could provide a corroboration for the impact of the oxygen octahedral tilting on thermal conductivity in LPCMO from a theoretical point of view.

Magnetism and thermal transport in LSMO/LMCO superlattices

Regarding the LSMO/LMCO superlattices (SLs) grown by the MAD technique on STO(100) substrates as $[\mathrm{LSMO}_n/\mathrm{LMCO}_n]_m$/STO(100), two main results emerged, involving the magnetic structure and the (magneto-) thermal conductivity:

First, such superlattices (with $n \geq 9$ u.c.) form exchange-spring magnets (ESM) due to the strong difference in coercive fields of LSMO (soft magnet, $H_{C,\mathrm{LSMO}} = (30 \pm 10)$ Oe) and LMCO (hard magnet, $H_{C,\mathrm{LMCO}} = (17.6 \pm 0.1)$ kOe) as it was shown by SQUID magnetometry measurements. Further, since the easy axis of the hard magnetic LMCO is OOP when grown on STO(100), it forces the magnetization of LSMO (with IP anisotropy) to rotate OOP within the SLs. Moreover, different Curie temperatures ($T_{\mathrm{C,LMCO}} < T_{\mathrm{C,LSMO}}$) of both compounds result in an IP magnetic easy axis of the SL at temperatures $T > T_{\mathrm{C,LSMO}}$ where only LSMO is ferromagnetic, which start to reorient OOP as LMCO becomes ferromagnetic when lowering the temperature below $T < T_{\mathrm{C,LMCO}}$. This reorientation leads to an apparent reduction of the IP magnetic moment of the SLs below $T_{\mathrm{C,LMCO}}$. However, increasing IP external magnetic fields up to $\mu_0 H = 5$ T, gradually rotates the reoriented OOP magnetization back IP. A further consequence of the different easy axes of both compounds (IP & OOP) is the formation of Néel domain wall-like spin structure at the interfaces which is most likely the origin of the measured positive electrical magnetoresistance due to an increased electron-spin scattering on such structure (schematic illustration in Fig. 8.3.6(b), p. 87). The real magnetic profile may look different. For modeling the interfacial spin distribution in LSMO/LMCO SLs, a micromagnetic simulation of the spatial distribution of magnetization in exchange spring magnets with orthogonal anisotropies could be used as presented by Xiang at al. [176] for similar ESM. Another minor but still important observation was the enhanced $T_{\mathrm{C,LMCO(SL)}} \approx 260$ K of the LMCO within the SLs, a value that is 35 K higher than that of bulk or of a single film LMCO/STO(100) ($T_{\mathrm{C,LMCO}} = 225$ K), which was also confirmed by Raman spectroscopy. This behavior of increased T_{C} was attributed to reduced dimensionality and coherent growth within the SLs and cannot be related to any changes of the oxygen octahedral tilting, as the tilt angles of LMCO in the SLs measured by HR-TEM using iDPC revealed tilting similar to bulk. The magnetic proximity (induced by the ferromagnetic LSMO) could also be the reason of the increased $T_{\mathrm{C,LMCO(SL)}}$ as such effects can be of a long range in low dimensional heterostructures, cf. [65].

The second main result for LSMO/LMCO SLs is that despite the general homogeneous crystalline structure and coherent interfaces, the measured thermal conductivity of the n=9 u.c. LSMO/LMCO SL was found to be ultra-low and strongly susceptible to magnetic fields in the whole temperature range used. The value at room temperature ($\kappa_{\mathrm{SL,n=9}}(300\ \mathrm{K}) = 0.32\ \mathrm{Wm^{-1}K^{-1}}$) is surprisingly much lower than that for typical amorphous materials (e.g., fused silica glass: $\kappa_{\mathrm{a\text{-}SiO2}}(300\ \mathrm{K}) = 1.35\ \mathrm{Wm^{-1}K^{-1}}$ [81]), but still in line with other reports on ultra-low thermal conductivity materials like Ruddlesden-Popper perovskites or chalcogenides [168–170] and is only slightly lower than literature values for bulk composites ($\kappa_{\mathrm{LSMO/SBTO}} = 0.39\ \mathrm{Wm^{-1}K^{-1}}$ [177]) or superlattices ($\kappa_{\mathrm{LSMO/LMO}} = 0.89\ \mathrm{Wm^{-1}K^{-1}}$ [172], $\kappa_{\mathrm{LSMO/STO}} = 0.8(1)\ \mathrm{Wm^{-1}K^{-1}}$ [173]) containing LSMO. For the SL studied here, the primary origin of such ultra-low values cannot be determined with certainty, because many different effects can lead to thermal conductivity reduction. Superlattice design can strongly decrease thermal conductivity by introducing thermal boundary resistances and other scattering mechanisms caused by the acoustic/diffuse mismatch between different materials (cf. [128]) , i.e., leading to phonon reflection and interference forming phonon band gaps (cf. [178]), or due to the so-called mini-Umklapp scattering corresponding to the reduced mini-Brillouin zone of the SL superstructure (cf. [179]). A theoretical modeling of the phonon band structure of LSMO/LMCO SLs by DFT calculations could provide insight in the phononic heat transport of such materials from a theoretical point of view. Oxygen octahedral tilting is also an effective way of strongly affecting thermal conductivity without affecting the general crystallinity of the material, cf. [120]. Meyer et al. [174, 180] measured thermal conductivity of MAD-grown $LaMnO_3/SrMnO_3$ superlattices $[(\mathrm{LMO})_{2n}/(\mathrm{SMO})_n]_m$/STO(100) by optical transient thermal reflectivity technique and found a significant interfacial thermal resistance increase due to the mismatched oxygen octahedral tilting of SMO ($\theta_{\mathrm{SMO}} \approx 0°$) and LMO ($\theta_{\mathrm{LMO}} \approx 15°$) within such SLs leading to a thermal conductivity reduction by approximately a factor of four at room temperature ($\kappa_{\mathrm{LMO2n/SMOn}} \approx 0.5\ \mathrm{Wm^{-1}K^{-1}}$) as compared to the samples with the same interface density but coherent interfaces with no tilting ($[(\mathrm{LMO})_n/(\mathrm{SMO})_n]_m$, $\kappa_{\mathrm{LMOn/SMOn}} \approx 2\ \mathrm{Wm^{-1}K^{-1}}$). The octahedral tilting of the LSMO/LMCO SL studied here showed an oscillatory behavior of the tilt angles across the films between $\theta_{\mathrm{LSMO}} \approx 10°$ and $\theta_{\mathrm{LMCO}} \approx 13°$ as revealed by the HR-TEM analysis (see Fig. A.3.6, p. 111). The higher degree of average tilting and its angle oscillation across the film together with the lower bulk thermal conductivity of LSMO and

LMCO compared to LMO and SMO could be the reason for the lower thermal conductivity of LSMO/LMCO SL.

Regarding the magnetic field dependency of the SL (Fig. 8.3.8, p. 90), the change of the thermal conductivity was found to be both negative and positive at different temperatures (up to $MTC(210\ \mathrm{K}, 3\ \mathrm{T}) = \Delta\kappa(H = 3\ \mathrm{T})/\kappa(H = 0) \approx -11\,\%$ and $MTC(130\ \mathrm{K}, 9\ \mathrm{T}) \approx +160\,\%$ respectively), which was associated with the spin order/disorder provided by the emerging exchange-spring magnetic 90° Néel domain wall-like structure. As it was discussed for the case of thin LPCMO films, colossal magnetoresistive (CMR) manganites possess strong interconnection of magnetism (spin), electrical conductivity (double exchange model) and structure (Jahn-Teller and oxygen octahedral distortions) which can lead to thermal conductivity changes coupled to external magnetic fields. For the single films of LPCMO or LSMO measured in this work, the change of thermal conductivity in external magnetic fields was found to be positive in the vicinity of T_C which corresponds to an the increase of magnetic (thus the connected structural) ordering leading to increased electron mobility and subsequent increase of thermal conductivity. In contrast, in the case of the LSMO/LMCO SL below the spin reorientation transition temperature $T_\mathrm{SR} \approx T_\mathrm{C,LMCO}$, an external magnetic field in the range of $\mu_0 H \leq 3$ T induced spin disorder due to the emergence of the domain wall-like magnetic structure (the spin distribution model schematically represented in Figs. 8.3.6(c)-(d), p. 87). Therefore, due to the strong coupling of magnetism, electrical and thermal conductivities of the LSMO, this spin disorder leads to a decrease of both electrical and thermal conductivity of the SL. On the other hand, a further increase of the magnetic field $\mu_0 H \geq 3$ induces ferromagnetic ordering (cf. Fig. 8.3.6(d)-(e), p. 87), which makes the change of magneto-thermal conductivity positive again, as expected from the spin distribution model.

For a better corroboration, it would be beneficial to extend and provide theoretical aiMD and DFT calculations like those presented by Fumega et al. [120] for analysis of the impact of homogeneous oxygen octahedral tilting and Jahn-Teller distortions on thermal conductivity to an inhomogeneous oscillatory angle distribution such as the one of the LSMO/LMCO SLs in the present work (Fig. A.3.6, p. 111).

As a further outlook, other superlattices containing soft/hard magnetic materials with non-collinear easy axes could possibly lead to even stronger MTC changes. Preliminary results on double perovskite/double perovskite La_2NiMnO_6/LMCO

grown on STO(100) by K. P. Stroh already showed a similar spin reorientation transition (see Fig. A.1.4 on p. 105) like in LSMO/LMCO, supporting the emergence of the ESM in LMCO-based SLs. Further SL combinations of for example LPCMO/LMCO might lead to increased MTC, too, since the CMR manganite LPCMO exhibits a much stronger thermal conductivity change induced by external magnetic fields than LSMO, though at lower temperatures. Also other non-perovskite thin films like 2D materials would be interesting to study, especially the magnetic field-dependent thermal conductivity of mono/multi/twisted layers of graphene or transition metal dichalcogenides, since such 2D materials were already successfully measured by the 3ω method in literature (e.g., [181]) and show remarkable thermal properties like twist angle dependency of thermal conductivity [182], thermal electromechanical switching [183] or ultra-high thermal conductivity [184].

All in all, this work demonstrated a new pathway of achieving active control of energy dissipation (here thermal transport) within nanoscale magnetic superlattices by external magnetic fields.

Part IV

Appendix

A Appendix

A.1 Additional measurements

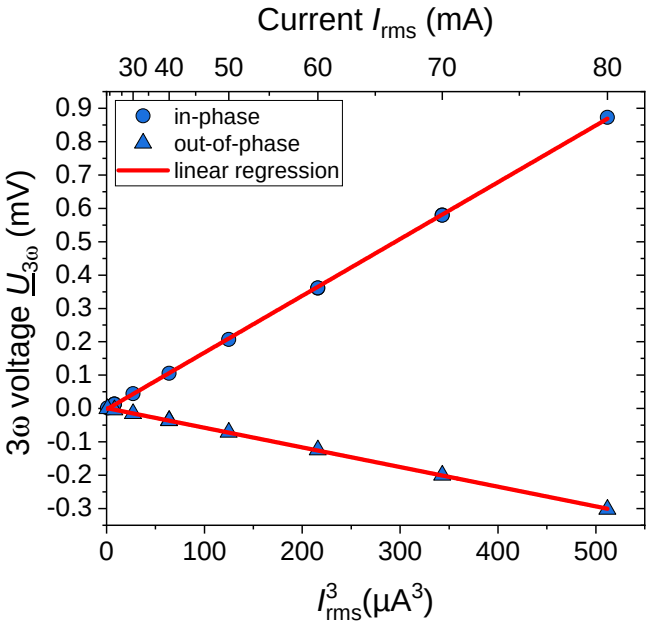

Fig. A.1.1: 3ω voltage vs. current cube characteristics $\underline{U}_{3\omega}(I^3)$ of the gold heater element (200 nm Au on 5 nm Cr adhesion layer, width $2b$=10.5 µm, length l=1 mm) on top of the STO(100) substrate at T = 300 K.

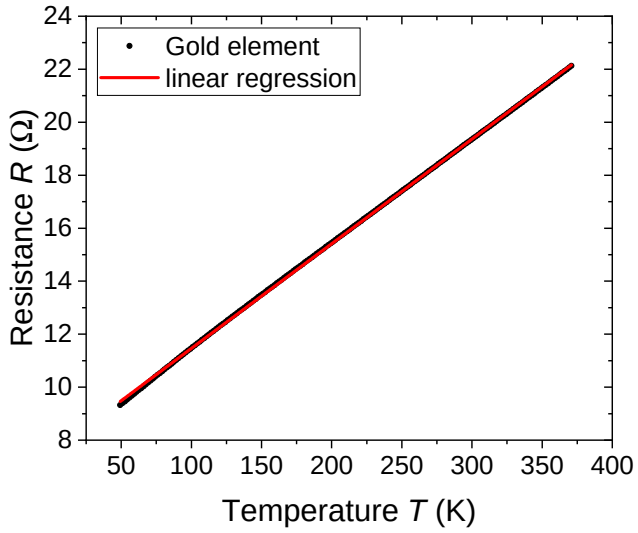

Fig. A.1.2: Electrical resistance of the gold heater element (200 nm Au on 5 nm Cr adhesion layer, width $2b$=10.5 µm, length l=1 mm) on top of the STO(100) substrate at T = 300 K.

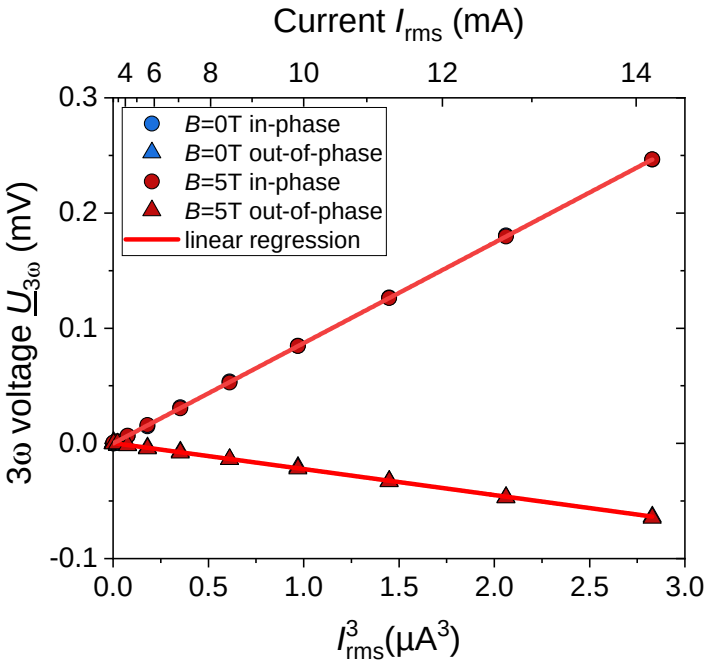

Fig. A.1.3: 3ω voltage vs. current cube characteristics $\underline{U}_{3\omega}(I^3)$ of the gold element on the d=19.9 nm am-Al_2O_3 sample at different magnetic fields (B=0 T and B=5 T) at T = 300 K showing no field dependence (data points lie approx. on top of each other).

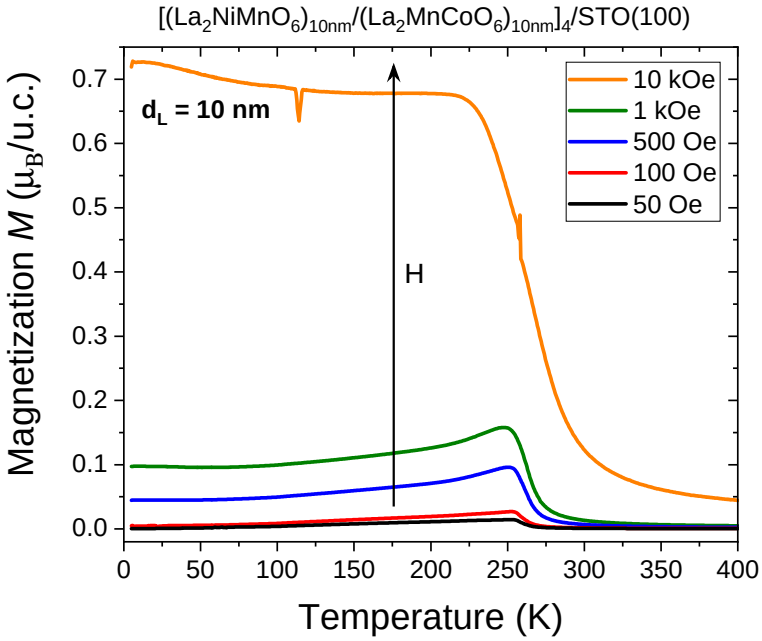

Fig. A.1.4: Field-cooled in-plane magnetization of a $[(\mathrm{LNMO})_{10\mathrm{nm}}/(\mathrm{LMCO})_{10\mathrm{nm}}]_4$/STO(100) SL in different external magnetic fields. Sample and measurement done by K. P. Stroh.

A.2 Continious temperature sweep 3ω measurement

Usually, the 3ω measurement is done in constant temperature mode by sweeping the excitation current frequency. The duration of one measurement to obtain thermal conductance or thermal resistance of a sample using the classical setup by Cahill [81] as used in this thesis is strongly dependent on the measured frequency range defining the lock-in time constants, the amount of measured frequencies as well as as other setup-related delays like the temperature stabilization time of the cryostat if temperature dependent measurements are done.

For the *Quantum Design PPMS* system used in this thesis, a temperature stabilization takes up to 10 minutes. At the minimal exitation frequency used ($f = 40$ Hz), the *SR*830 lock-in needs an integration time constant extending at least over 10 periods of the oscillating signal ($\tau = 10/f = 0.25$ s giving next possible setting of $\tau = 0.3$ s) resulting in a settling time of $10\tau = 3$ s at a 24 dB/oct attenuation according to the manual. Nevertheless, such measurements have poor signal-to-noise ratios compared to a higher integration time of, e.g., $\tau = 100/f \approx 3$ s along with a settling time of $20\tau = 60$ s, therefore, the latter setting was preferably used in measurements within this thesis.

Given the temperature stabilization duration and the lock-in settling time, a full temperature dependent thermal conductivity measurement of a sample at one magnetic field and 10 different frequencies in a temperature range of 50 K $< T <$ 350 K takes approximately 7.5 hours if the temperature step is $\Delta T = 10$ K. Reducing the temperature step to $\Delta T = 1$ K in order to better resolve the temperature dependence extends the measurement time easily to more than 3 days.

A reasonable data reduction can be achieved by discarding the high frequency measurements (which have the lowest signal to noise ratio due to the negative slope of the 3ω voltage as a function of frequency). Using either only one measurement at the lowest measurable frequency for thermal resistance measurements of a film on a substrate (thermal offset due to a thermal resistance arising from a thin film is frequency independent, cf. [82], see for example Fig. 6.3.3 on p. 56) or using two frequencies for thermal conductivity measurements of substrates (as for the slope method), cf. [82]. The only trade-off is the reduced statistics resulting in a higher measurement uncertainty. A comparison of such reduced data set with an evaluation of a full set of frequencies for a STO(100) substrate measurement resulted in thermal conductivity errors below $\pm 3\%$ at any measured temperature.

The advantage of using only one excitation current frequency is that a continious temperature sweep can be used. Given a settling time of the lock-in of $20\tau = 60$ s, a cooling/heating rate of 1 K/min is an appropriate compromise to ensure a temperature resolution of 1 K. With this rate, a measurement of a thin film on a substrate over a 300 K sweep takes only 5 hours, whereas it is slightly above 10 hours for a substrate measurement due to the need of an additional second frequency sweep.

A.3 Supplementary Materials: Magnetism and magneto-thermal conductivity in exchange-spring-coupled manganites

This chapter consists of the published manuscript of the Supplementary Materials for "Magnetism and Thermal Transport of Exchange-Spring-Coupled $La_{2/3}Sr_{1/3}MnO_3$/ La_2MnCoO_6 Superlattices with Perpendicular Magnetic Anisotropy" [135] by Vitaly Bruchmann-Bamberg[1)], Isabell Weimer[1)], Vladimir Roddatis[2)], Ulrich Ross[3)], Leonard Schüler[1)], Karen P. Stroh[1)] and Vasily Moshnyaga[1)], *Nanomaterials* 13(21), 2897, 2023.

Affiliations: 1) Erstes Physikalisches Institut, Georg-August-University Göttingen, Friedrich-Hund-Platz 1, 37077 Göttingen, Germany;
2) Helmholtz Centre Potsdam, GFZ German Research Centre for Geosciences, Telegrafenberg, 14473 Potsdam, Germany;
3) IV. Physikalisches Institut, Georg-August-University Göttingen, Friedrich-Hund-Platz 1, 37077 Göttingen, Germany.

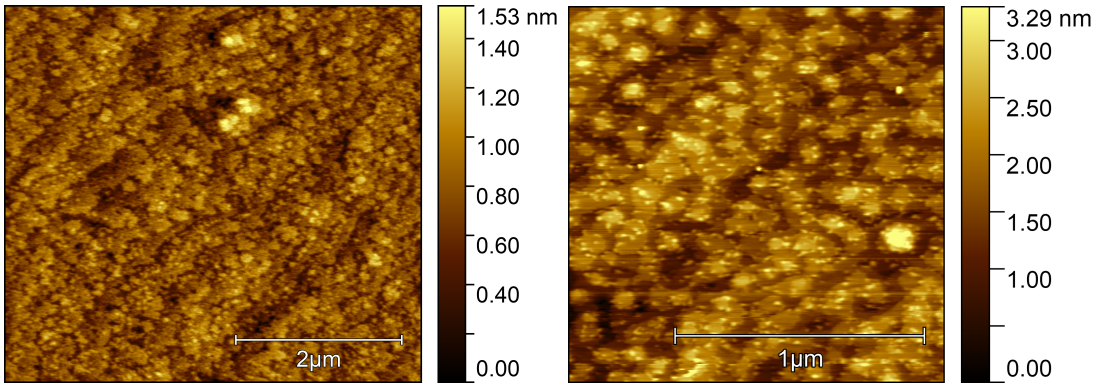

Fig. A.3.1: Left: Atomic force microscope topography of the $[(LMCO)_n/(LSMO_n)]_m$/STO(100) n=9 u.c. SL (RMS roughness S_q=0.2(1) nm); Right: SL n=24 u.c. (S_q=0.5(1) nm).

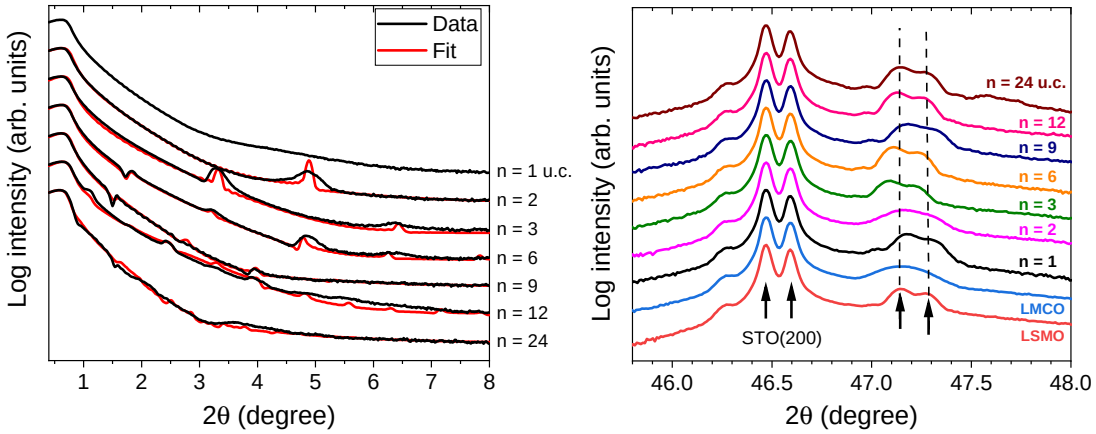

Fig. A.3.2: Left: XRR patterns (black curves) and fitting curves using the program *GenX3* [100] of $[LSMO_n/LMCO_n]_m$/STO(100) SLs revealing superstructure peaks of the bilayers. The fit parameters are listed in Tab. 1. Right: X-Ray diffraction patterns of the SLs reveal a very similar out-of-plane lattice parameter $c \approx 3.852 \pm 0.004$ Å for all SLs and single LSMO and LMCO films. The arrows indicate the $k_{\alpha 1}/k_{\alpha 2}$ spliting of the STO(200) peak and of the (002) peak of most SLs.

[100] A. Glavic and M. Björck, "GenX 3: the latest generation of an established tool", J. Appl. Cryst. 55, 1063 (2022)

Tab. A.3.1: *GenX*3 fit parameters for $[LSMO_n/LMCO_n]_m$/STO(100) SLs

n (u.c.)	Targeted bilayer thickness d_{2n} (nm)	Measured d_{2n} (nm)	Deviation per bilayer	Average interfacial roughness σ_{RMS} (nm)
2	1.54	1.85	+ 1 u.c.	0.4
3	2.31	2.75	+ 1 u.c.	0.5
6	4.62	5.68	+ 3 u.c.	0.5
9	6.93	7.06	< 1 u.c.	0.9
12	9.24	11.5	+ 6 u.c.	0.6
24	18.49	21.1	+ 7 u.c.	1.1

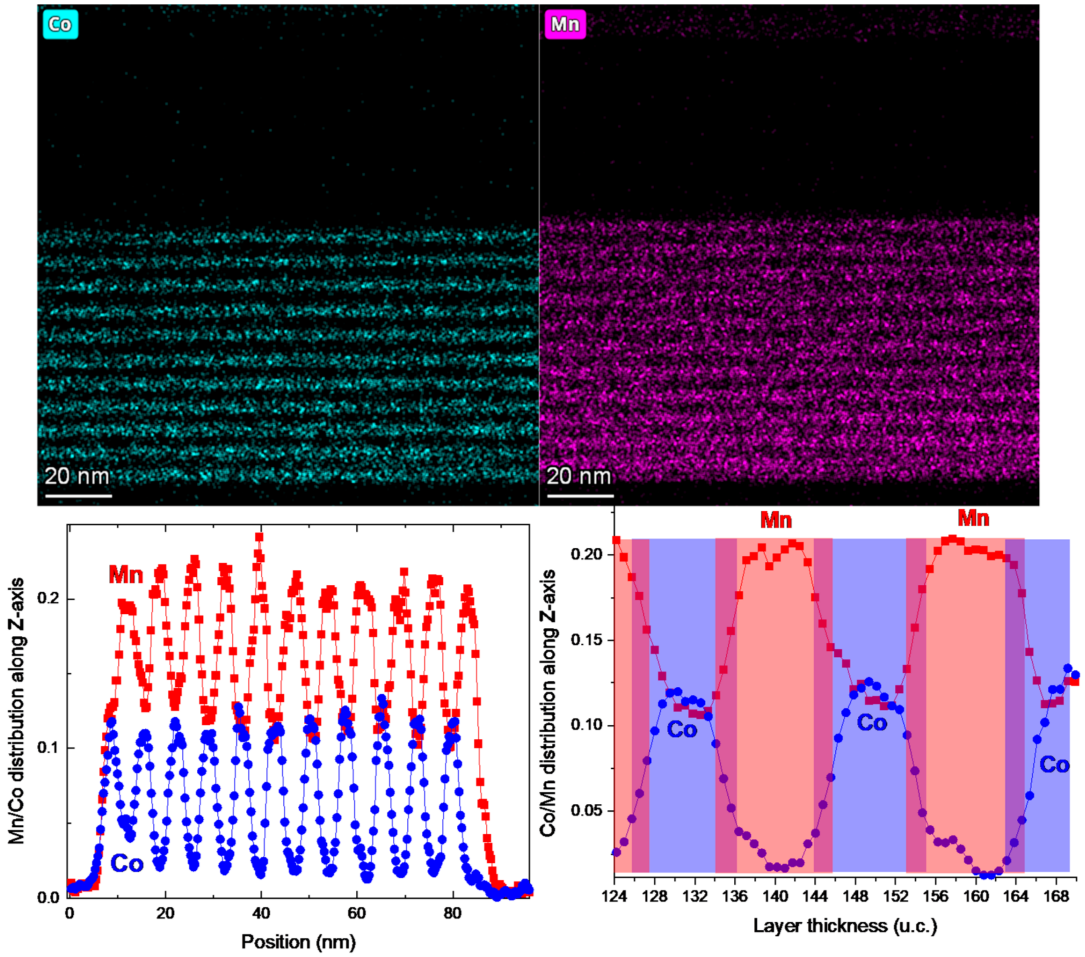

Fig. A.3.3: Distribution of Co (top, left) and Mn (top, right) atoms within the $[(LMCO)_9(LSMO)_9]_{11}$ SL obtained by using energy dispersive X-ray micro-analysis (EDX) (left panels) shows a clear chemical contrast between the LMCO and the LSMO layers. A linear scan along the growth direction of the whole SL (bottom, left) and along the selected layers in the middle of SL (bottom, right), from which a (Co/Mn) intermixing at the LSMO/LMCO interfaces with a thickness ~2 u.c. can be deduced.

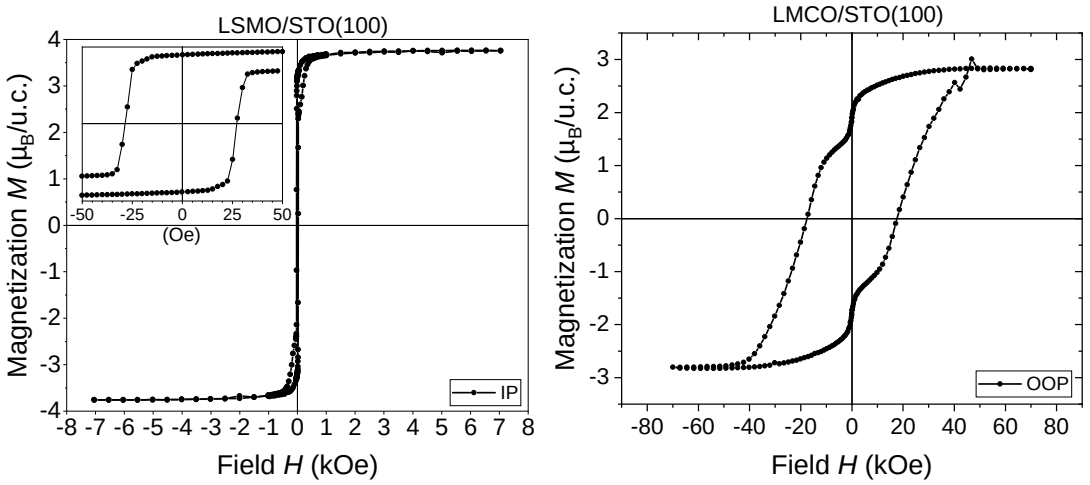

Fig. A.3.4: Magnetic hysteresis loops for LSMO/STO(100) (left) and LMCO/STO(100) (right) at 5K along their respective easy axis.

Tab. A.3.2: Saturation magnetization and coercive field of LSMO/STO(100) and LMCO/STO(100) along their easy axis.

	M_{sat} [μ_{B}/u.c.]	H_{C} [Oe]
LSMO/STO(100) IP	3.8(1) (theory: 3.7)	30(10)
LMCO/STO(100) OOP	2.8(1) (theory: 3)	17600(100)

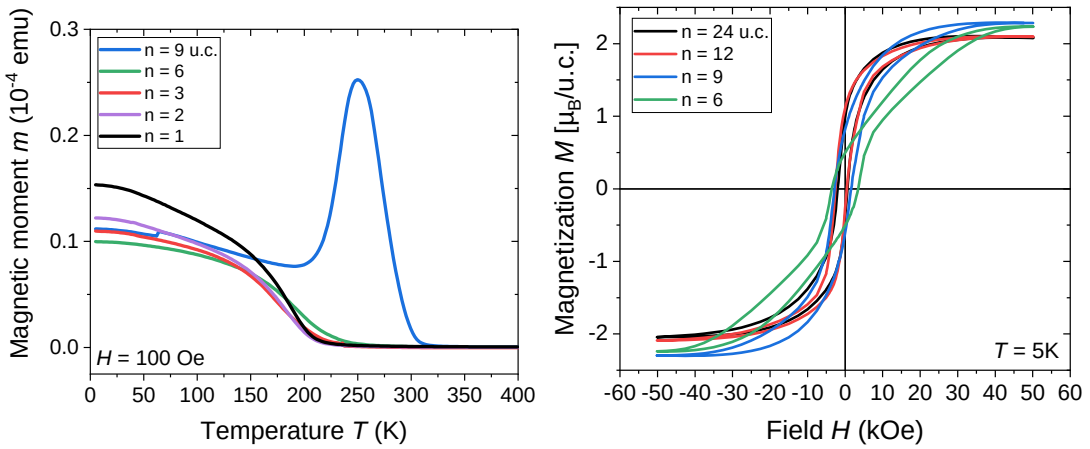

Fig. A.3.5: Left: Field-cooled IP magnetic moment of the $[(\mathrm{LMCO})_{\mathrm{n}}/(\mathrm{LSMO}_{\mathrm{n}})]_{\mathrm{m}}$/STO(100) (n = 1-9 u.c.) superlattices at low magnetic field. Spin reorientation transition is missing in SLs with very thin LSMO and LMCO layers. Right: IP Magnetic hysteresis loops of selected $[(\mathrm{LMCO})_{\mathrm{n}}/(\mathrm{LSMO}_{\mathrm{n}})]_{\mathrm{m}}$/STO(100) superlattices.

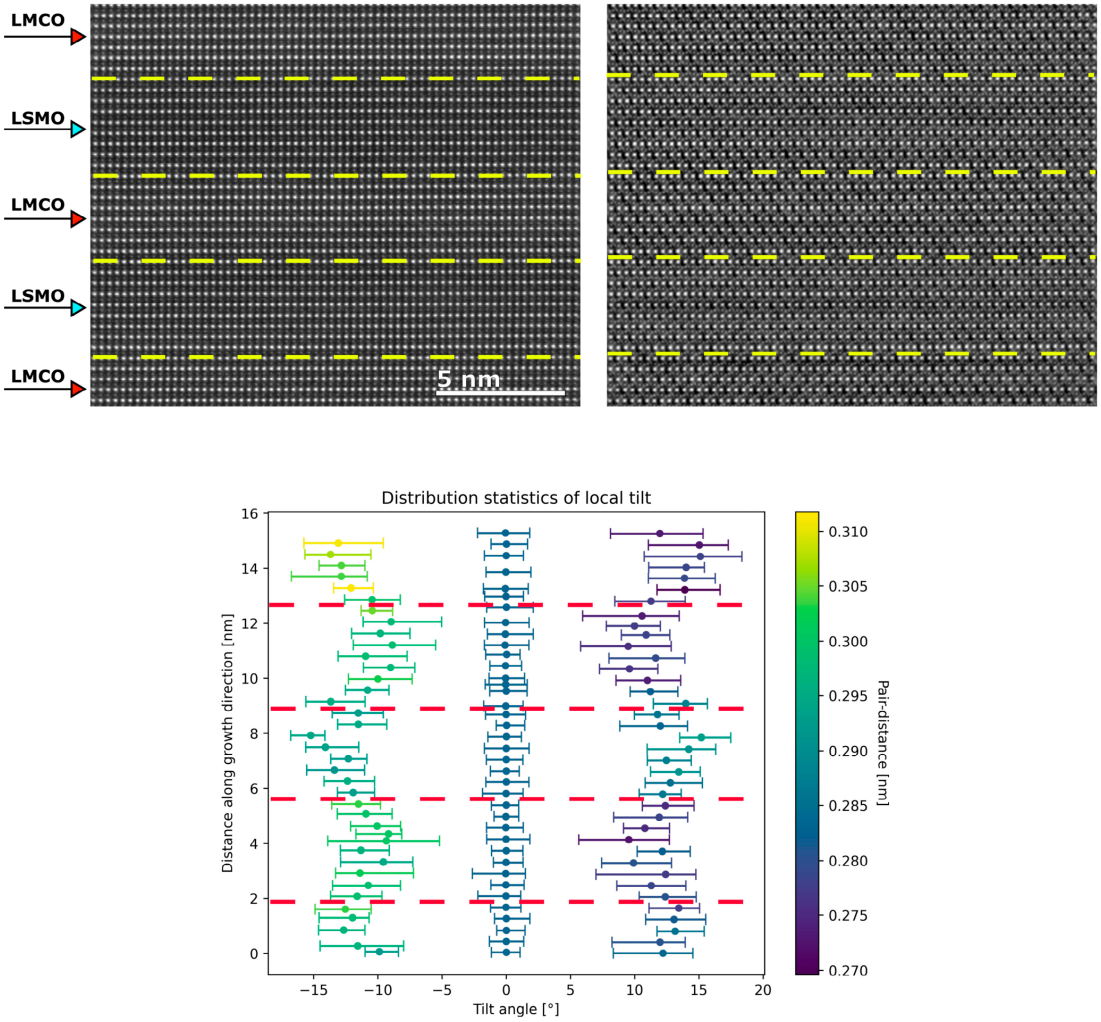

Fig. A.3.6: ADF-STEM (top, left), iDPC (top, right) images of the $[LSMO_9/LMCO_9]_{11}/STO(100)$ superlattice, with the corresponding evaluation of octahedral tilt angles θ within the image plane (bottom). Connection to the Mn-O-Mn(Co) angle in the main text is done via $\varphi_{\text{B-O-B}} = 180°\text{-}2\theta$. The central cluster around $\theta = 0°$ (on the right panel) corresponds to the Mn-Mn pairs, while the datapoints around $\theta = \pm 12°$ correspond to the Mn-O-Mn(Co) bond chains. The analysis reveals continuous change of the octahedral tilt angle at the interfaces between LMCO ($\theta_{\text{LMCO}} \approx 13°$) and LSMO ($\theta_{\text{LSMO}} \approx 10°$). Error bars indicate the maximum scattering of the angles within one layer, while the standard deviation for all layers lies in the range of $\sigma(\theta)$=0.5-1.5°.

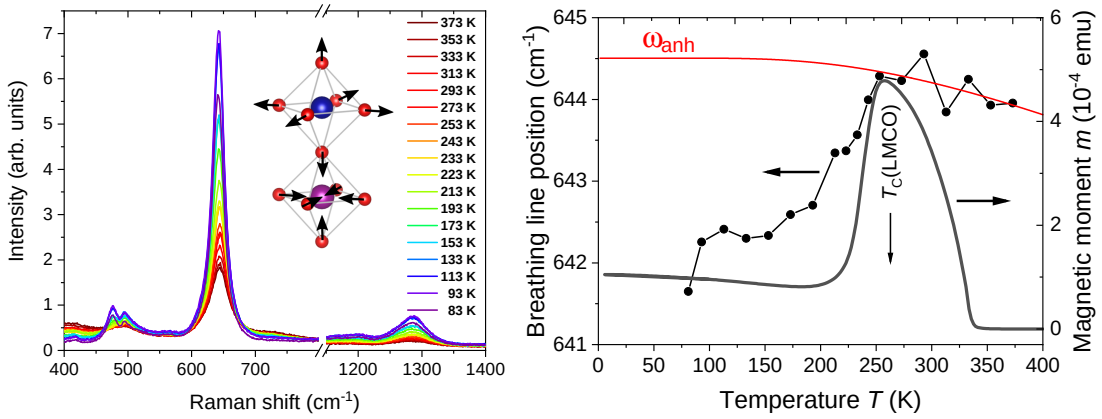

Fig. A.3.7: Left: Raman spectra of the n = 24 u.c. SL $[(\mathrm{LSMO})_{24}/(\mathrm{LMCO})_{24}]_4$/STO(100) measured for different temperatures in the range $T \approx$ 100-400 K and an illustration of the 644 cm^{-1} breathing mode vibration; Right: Temperature dependence of the position of the breathing line (left scale) and IP magnetic moment (right scale) indicates a significant increase of the Curie temperature of the LMCO layers within the SL up to about $T_{\mathrm{C,LMCO}} \approx 260$ K. The red line is a fit to the anharmonic line shift $\omega(T) = \omega_0 + C\left(1 + 2/\left(e^{\hbar\omega_0/2k_BT} - 1\right)\right)$ [185] for temperatures $T > T_{\mathrm{C,LMCO}}$.

[185] Balkanski, M., Wallis, R. F.& Haro, E. Anharmonic effects in light scattering due to optical phonons in silicon. *Phys. Rev. B* **28**, 1928 (1983).

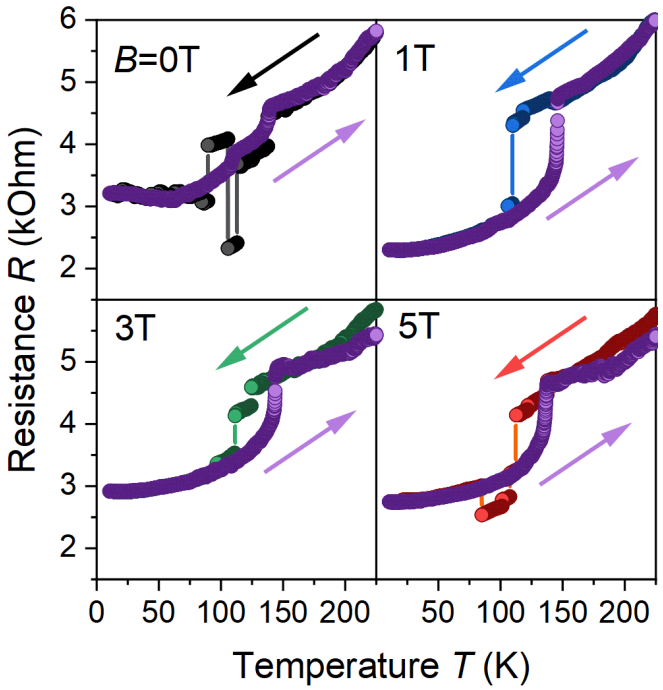

Fig. A.3.8: Electrical resistance vs temperature (both current and magnetic field applied in-plane) in the vicinity of structural phase transition in STO at T*=105 K for the $[(LMCO)_9/(LSMO_9)]_{11}$/STO(100) SL at different magnetic fields. The arrows indicate the direction of the temperature scan.

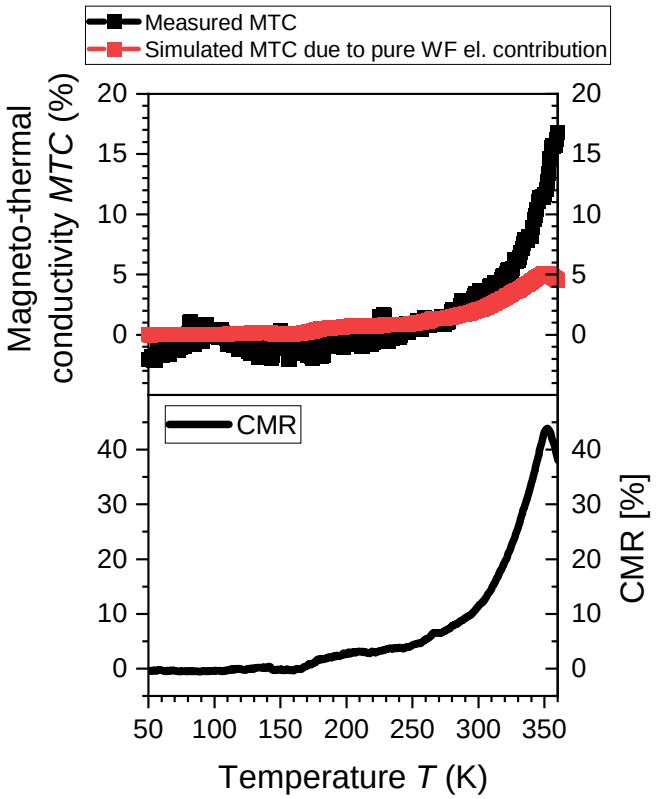

Fig. A.3.9: Top panel: measured magneto-thermal conductivity, MTC=100%*[κ(5 T)-κ(0)]/κ(0), (black points) and the estimated from the Wiedemann-Franz (WF) law for electronic contricbution to MTC due to CMR (red points) of the single LSMO/STO(100). Bottom panel: colossal magnetoresistance CMR=100%*[R(0)-R(5 T)]/R(0) of the LSMO/STO(100) thin film shows a typical behaviour with a peak close to T_C≈350 K.

List of abbreviations

_ (Underline): Complex value

˜ (Tilde): Analytical quantity

ALE: Aatomic layer epitaxy

b: Heater element half-width

CC BY 3.0: Creative commons license, see details under https://creativecommons.org/licenses/by/3.0

CC BY-NC-ND 4.0: Creative commons license, see details under https://creativecommons.org/licenses/by-nc-nd/4.0

CMR: Colossal magnetoresistance, $CMR = -100\% \cdot [\rho(H) - \rho(0)]/\rho(0)$

D: Thermal diffusivity

DE: Double exchange

f: Current excitation frequency

IP: In-plane

κ: Thermal conductivity

l: Heater element length between the voltage probes

LPCMO: $(La_{0.6}Pr_{0.4})_{0.7}Ca_{0.3}MnO_3$

MAD: Metalorganic Aerosol Deposition

ESM: Exchange-spring magnet

PMA: Perpendicular magnetic anisotropy

MR: Magnetoresistance, $MR = [\rho(H) - \rho(0)]/\rho(0)$

MTC: Magneto-thermal conductivity, $MTC = [\kappa(\mathrm{B} \neq 0)$ - $\kappa(\mathrm{B} = 0)]/\kappa(\mathrm{B} = 0)$

R: Electrical resistance

R_{th}: Thermal resistance

RMS: Root mean square

$\underline{T}$: Complex temperature oscillation

TMO: Transition metal oxide

ω: Current excitation angular frequency $\omega = 2\pi f$

OOP: Out-of-plane

PPMS: *Quantum Design Physical Properties Measurement System*

XRD: X-ray diffraction

XRR: X-ray reflectometry

$\underline{Z}$: Complex surface thermal impedance

List of publications

Articles related to this thesis:

1. **V. Bruchmann-Bamberg**, I. Weimer, V. Roddatis, U. Ross, L. Schüler, K. P. Stroh and V. Moshnyaga, "Magnetism and Thermal Transport of Exchange-Spring-Coupled $La_{2/3}Sr_{1/3}MnO_3/La_2MnCoO_6$ Superlattices with Perpendicular Magnetic Anisotropy", *Nanomaterials* 13(21), 2897, 2023.

2. P. Henning, R. Gruhl, U. Ross, V. Roddatis, **V. Bruchmann-Bamberg**, K. P. Stroh, M. Seibt, P. Gegenwart and V. Moshnyaga, "Tailoring of magnetism & electron transport of manganite thin films by controlling the Mn-O-Mn bond angles via strain engineering", *Sci. Rep.* 14, 3253, 2024.

Other publications:

3. S. Merten, **V. Bruchmann-Bamberg**, B. Damaschke, K. Samwer, and V. Moshnyaga, "Jahn-Teller reconstructed surface of the doped manganites shown by means of surface-enhanced Raman spectroscopy", *Phys. Rev. Materials* 3, 060401(R), 2019.

4. D. Meyer, D. Metternich, P. Henning, J. P. Bange, R. Gruhl, **V. Bruchmann-Bamberg**, V. Moshnyaga, H. Ulrichs, "Coherent phonon transport and minimum of thermal conductivity in $LaMnO_3/SrMnO_3$ superlattices", *arXiv*:2108.05860, 2021.

5. J. P. Bange, V. Roddatis, L. Schüler, F. Lyzwa, M. Keunecke, S. Lopatin, **V. Bruchmann-Bamberg**, V. Moshnyaga, "Charge Transfer Control of Emergent Magnetism at $SrMnO_3/LaMnO_3$ Interfaces", *Adv. Mater. Interfaces* 9, 2201282, 2022.

6. C. Seick, K. Stroh, T. Titze, **V. Bruchmann-Bamberg**, A. Weisser, S. Mathias, V. Moshnyaga, H. Ulrichs, and D. Steil, "Energy relaxation in $(La_{0.6}Pr_{0.4})_{0.7}Ca_{0.3}MnO_3$ films across the metal-insulator transition", *Phys. Rev. B* 107, 085115, 2023.

Conference contributions (poster presentations):

1. "Reduction of dead layer in $La_{0.7}Sr_{0.3}MnO_3$ at the $(SrO)_2$ buffered interface with $SrTiO_3$", DPG Spring Meeting, Regensburg 2019.

2. "Emergent phases in manganite-based heterostructures", International Workshop on Correlated Dynamics in Energy Conversion IWCE, Göttingen 2019.

3. "Magnetic Field-Dependent Thermal Conductivity in Manganite Thin Films", DPG Spring Meeting, Regensburg 2022.

4. "Magnetic Field-Dependent Thermal Conductivity in $(La_{0.6}Pr_{0.4})_{0.7}Ca_{0.3}MnO_3$ Thin Films", 67th Annual Conference on Magnetism and Magnetic Materials (MMM 2022), Minneapolis USA 2022.

Bibliography

[1] G. Rose, "Beschreibung einiger neuen Mineralien des Urals," *Annalen der Physik und Chemie*, vol. 124, no. 12, pp. 551–573, 1839.

[2] H.-R. Wenk and A. Bulakh, *Minerals: Their Constitution and Origin*. Cambridge University Press, 2004.

[3] W.-J. Yin, B. Weng, J. Ge, Q. Sun, Z. Li, and Y. Yan, "Oxide perovskites, double perovskites and derivatives for electrocatalysis, photocatalysis, and photovoltaics," *Energy & Environmental Science*, vol. 12, no. 2, pp. 442–462, 2019.

[4] N. F. Atta, A. Galal, and E. H. El-Ads, "Perovskite Nanomaterials – Synthesis, Characterization, and Applications," in *Perovskite Materials - Synthesis, Characterisation, Properties, and Applications* (L. Pan and G. Zhu, eds.), InTech, 2016.

[5] F. Zhang, B. Yang, K. Zheng, S. Yang, Y. Li, W. Deng, and R. He, "Formamidinium Lead Bromide ($FAPbBr_3$) Perovskite Microcrystals for Sensitive and Fast Photodetectors," *Nano-micro letters*, vol. 10, no. 3, p. 43, 2018.

[6] Q. Chen, J. Wu, X. Ou, B. Huang, J. Almutlaq, A. A. Zhumekenov, X. Guan, S. Han, L. Liang, Z. Yi, J. Li, X. Xie, Y. Wang, Y. Li, D. Fan, D. B. L. Teh, A. H. All, O. F. Mohammed, O. M. Bakr, T. Wu, M. Bettinelli, H. Yang, W. Huang, and X. Liu, "All-inorganic perovskite nanocrystal scintillators," *Nature*, vol. 561, no. 7721, pp. 88–93, 2018.

[7] S. D. Stranks and H. J. Snaith, "Metal-halide perovskites for photovoltaic and light-emitting devices," *Nature nanotechnology*, vol. 10, no. 5, pp. 391–402, 2015.

[8] A. Noculak, V. Morad, K. M. McCall, S. Yakunin, Y. Shynkarenko, M. Wörle, and M. V. Kovalenko, "Bright Blue and Green Luminescence of Sb(III) in Double Perovskite Cs_2MInCl_6 (M = Na, K) Matrices," *Chemistry of Materials*, vol. 32, no. 12, pp. 5118–5124, 2020.

[9] H. Zhu, Y. Fu, F. Meng, X. Wu, Z. Gong, Q. Ding, M. V. Gustafsson, M. T. Trinh, S. Jin, and X.-Y. Zhu, "Lead halide perovskite nanowire lasers with low lasing thresholds and high quality factors," *Nature materials*, vol. 14, no. 6, pp. 636–642, 2015.

[10] G. E. Eperon, T. Leijtens, K. A. Bush, R. Prasanna, T. Green, J. T.-W. Wang, D. P. McMeekin, G. Volonakis, R. L. Milot, R. May, A. Palmstrom, D. J. Slotcavage, R. A. Belisle, J. B. Patel, E. S. Parrott, R. J. Sutton, W. Ma, F. Moghadam, B. Conings, A. Babayigit, H.-G. Boyen, S. Bent, F. Giustino, L. M. Herz, M. B. Johnston, M. D. McGehee, and H. J. Snaith, "Perovskite-perovskite tandem photovoltaics with optimized band gaps," *Science (New York, N.Y.)*, vol. 354, no. 6314, pp. 861–865, 2016.

[11] J. Park, J. Kim, H.-S. Yun, M. J. Paik, E. Noh, H. J. Mun, M. G. Kim, T. J. Shin, and S. I. Seok, "Controlled growth of perovskite layers with volatile alkylammonium chlorides," *Nature*, vol. 616, no. 7958, pp. 724–730, 2023.

[12] L. Zhou, Y.-F. Xu, B.-X. Chen, D.-B. Kuang, and C.-Y. Su, "Synthesis and Photocatalytic Application of Stable Lead-Free $Cs_2AgBiBr_6$ Perovskite Nanocrystals," *Small (Weinheim an der Bergstrasse, Germany)*, vol. 14, no. 11, p. e1703762, 2018.

[13] A. Filippetti, C. Caddeo, P. Delugas, and A. Mattoni, "Appealing Perspectives of Hybrid Lead–Iodide Perovskites as Thermoelectric Materials," *The Journal of Physical Chemistry C*, vol. 120, no. 50, pp. 28472–28479, 2016.

[14] M. A. Amin, G. Nazir, Q. Mahmood, J. Alzahrani, N. A. Kattan, A. Mera, H. Mirza, A. Mezni, M. S. Refat, A. A. Gobouri, and T. Altalhi, "Study of double perovskites X_2InSbO_6 (X = Sr, Ba) for renewable energy; alternative of organic-inorganic perovskites," *Journal of Materials Research and Technology*, vol. 18, pp. 4403–4412, 2022.

[15] L. Chu, W. Ahmad, W. Liu, J. Yang, R. Zhang, Y. Sun, J. Yang, and X. Li, "Lead-Free Halide Double Perovskite Materials: A New Superstar Toward Green and Stable Optoelectronic Applications," *Nano-micro letters*, vol. 11, no. 1, p. 16, 2019.

[16] D. I. Khomskii, *Transition Metal Compounds*. Cambridge University Press, 2014.

[17] F. Büttner, I. Lemesh, and G. S. D. Beach, "Theory of isolated magnetic skyrmions: From fundamentals to room temperature applications," *Scientific reports*, vol. 8, no. 1, p. 4464, 2018.

[18] Y. Xu, D. D. Awschalom, and J. Nitta, *Handbook of spintronics*. Springer reference, Dordrecht: Springer, 2016.

[19] M. N. Baibich, J. M. Broto, A. Fert, D. F. van Nguyen, F. Petroff, P. Etienne, G. Creuzet, A. Friederich, and J. Chazelas, "Giant magnetoresistance of (001)Fe/(001)Cr magnetic superlattices," *Physical review letters*, vol. 61, no. 21, pp. 2472–2475, 1988.

[20] G. Binasch, P. Grünberg, F. Saurenbach, and W. Zinn, "Enhanced magnetoresistance in layered magnetic structures with antiferromagnetic interlayer exchange," *Physical review. B, Condensed matter*, vol. 39, no. 7, pp. 4828–4830, 1989.

[21] E. F. Kneller and R. Hawig, "The exchange-spring magnet: a new material principle for permanent magnets," *IEEE Transactions on Magnetics*, vol. 27, no. 4, pp. 3588–3560, 1991.

[22] D. Suess, T. Schrefl, R. Dittrich, M. Kirschner, F. Dorfbauer, G. Hrkac, and J. Fidler, "Exchange spring recording media for areal densities up to 10Tbit/in^2," *Journal of Magnetism and Magnetic Materials*, vol. 290-291, pp. 551–554, 2005.

[23] D. Suess, T. Schrefl, S. Fähler, M. Kirschner, G. Hrkac, F. Dorfbauer, and J. Fidler, "Exchange spring media for perpendicular recording," *Applied Physics Letters*, vol. 87, no. 1, 2005.

[24] N. P. Padture, M. Gell, and E. H. Jordan, "Thermal barrier coatings for gas-turbine engine applications," *Science (New York, N.Y.)*, vol. 296, no. 5566, pp. 280–284, 2002.

[25] C. U. Hardwicke and Y.-C. Lau, "Advances in Thermal Spray Coatings for Gas Turbines and Energy Generation: A Review," *Journal of Thermal Spray Technology*, vol. 22, no. 5, pp. 564–576, 2013.

[26] M. Grätzel, "The light and shade of perovskite solar cells," *Nature materials*, vol. 13, no. 9, pp. 838–842, 2014.

[27] V. M. Goldschmidt, "Die Gesetze der Krystallochemie," *Die Naturwissenschaften*, vol. 14, no. 21, pp. 477–485, 1926.

[28] P. Ksoll, *Kationordnung und Grenzflächeneffekte in stark korrelierten Elektronensystemen*. Dissertation, DOI: 10.53846/goediss-8863, Georg August University of Goettingen, 2021.

[29] K.-I. Kobayashi, T. Kimura, H. Sawada, K. Terakura, and Y. Tokura, "Room-temperature magnetoresistance in an oxide material with an ordered double-perovskite structure," *Nature*, vol. 395, no. 6703, pp. 677–680, 1998.

[30] R. I. Dass and J. B. Goodenough, "Multiple magnetic phases of $La_2CoMnO_{6-\delta}(0<\sim \delta <\sim 0.05)$," *Physical review. B, Condensed matter*, vol. 67, no. 1, 2003.

[31] D. Serrate, J. M. de Teresa, and M. R. Ibarra, "Double perovskites with ferromagnetism above room temperature," *Journal of Physics: Condensed Matter*, vol. 19, no. 2, p. 023201, 2007.

[32] K. Leng, Q. Tang, Y. Wei, L. Yang, Y. Xie, Z. Wu, and X. Zhu, "Recent advances in Re-based double perovskites: Synthesis, structural characterization, physical properties, advanced applications, and theoretical studies," *AIP Advances*, vol. 10, no. 12, 2020.

[33] R. Galceran, L. López-Mir, B. Bozzo, J. Cisneros-Fernández, J. Santiso, L. Balcells, C. Frontera, and B. Martínez, "Strain-induced perpendicular magnetic anisotropy in $La_2CoMnO_{6-\epsilon}$ thin films and its dependence on film thickness," *Physical Review B*, vol. 93, no. 14, 2016.

[34] M. Jungbauer, *Gestaltung der elektronischen Korrelationen in Perowskit-Heterostrukturen auf atomarer Skala.* Dissertation, DOI: 10.53846/goediss-5462, Georg August University of Goettingen, 2016.

[35] H. A. Jahn, E. Teller, "Stability of polyatomic molecules in degenerate electronic states - I-Orbital degeneracy," *Proc. R. Soc. Lond. A*, vol. 161, no. 905, pp. 220–235, 1937.

[36] T. Chatterji, ed., *Colossal magnetoresistive manganites.* Dordrecht, The Netherlands and Boston and London: Kluwer Academic Publishers, 2004.

[37] Y. Tokura, ed., *Colossal magnetoresistive oxides*, vol. 2 of *Advances in condensed matter science.* Amsterdam: Gordon & Breach, 2000.

[38] M.-C. Wang and C.-R. Chang, "Goodenough-Kanamori-Anderson Rules in $CrI_3/MoTe_2/CrI_3$ Van der Waals Heterostructure," *Journal of The Electrochemical Society*, vol. 169, no. 5, p. 053507, 2022.

[39] H. Kramers, "L'interaction Entre les Atomes Magnétogènes dans un Cristal Paramagnétique," *Physica*, vol. 1, no. 1-6, pp. 182–192, 1934.

[40] P. W. Anderson, "Antiferromagnetism. Theory of Superexchange Interaction," *Physical Review*, vol. 79, no. 2, pp. 350–356, 1950.

[41] J. B. Goodenough, "Theory of the Role of Covalence in the Perovskite-Type Manganites [La, M(II)]MnO_3," *Physical Review*, vol. 100, no. 2, pp. 564–573, 1955.

[42] J. B. Goodenough, "An interpretation of the magnetic properties of the perovskite-type mixed crystals $La_{1-x}Sr_xCoO_{3-\lambda}$," *Journal of Physics and Chemistry of Solids*, vol. 6, no. 2-3, pp. 287–297, 1958.

[43] J. Kanamori, "Superexchange interaction and symmetry properties of electron orbitals," *Journal of Physics and Chemistry of Solids*, vol. 10, no. 2-3, pp. 87–98, 1959.

[44] R. Gross and A. Marx, *Spinelektronik.* Lecture notes, Walther-Meissner-Institut, 2004.

[45] C. Zener, "Interaction Between the d Shells in the Transition Metals," *Physical Review*, vol. 81, no. 3, pp. 440–444, 1951.

[46] C. Zener, "Interaction between the d -Shells in the Transition Metals. II. Ferromagnetic Compounds of Manganese with Perovskite Structure," *Physical Review*, vol. 82, no. 3, pp. 403–405, 1951.

[47] P. W. Anderson and H. Hasegawa, "Considerations on Double Exchange," *Physical Review*, vol. 100, no. 2, pp. 675–681, 1955.

[48] P.-G. de Gennes, "Effects of Double Exchange in Magnetic Crystals," *Physical Review*, vol. 118, no. 1, pp. 141–154, 1960.

[49] V. Moshnyaga, A. Belenchuk, S. Hühn, C. Kalkert, M. Jungbauer, O. I. Lebedev, S. Merten, K.-Y. Choi, P. Lemmens, B. Damaschke, and K. Samwer, "Intrinsic antiferromagnetic coupling underlies colossal magnetoresistance effect: Role of correlated polarons," *Physical Review B*, vol. 89, no. 2, 2014.

[50] M. Medarde, J. Mesot, P. Lacorre, S. Rosenkranz, P. Fischer, and K. Gobrecht, "High-pressure neutron-diffraction study of the metallization process in $PrNiO_3$," *Physical review. B, Condensed matter*, vol. 52, no. 13, pp. 9248–9258, 1995.

[51] W. A. Harrison, *Electronic structure and the properties of solids: The physics of the chemical bond*. San Francisco: Freeman, 1980.

[52] K.-i. Chahara, T. Ohno, M. Kasai, and Y. Kozono, "Magnetoresistance in magnetic manganese oxide with intrinsic antiferromagnetic spin structure," *Applied Physics Letters*, vol. 63, no. 14, pp. 1990–1992, 1993.

[53] R. von Helmolt, J. Wecker, B. Holzapfel, L. Schultz, and K. Samwer, "Giant negative magnetoresistance in perovskitelike $La_{2/3}Ba_{1/3}MnO_x$ ferromagnetic films," *Physical review letters*, vol. 71, no. 14, pp. 2331–2333, 1993.

[54] Y. Tokura and Y. Tomioka, "Colossal magnetoresistive manganites," *Journal of Magnetism and Magnetic Materials*, vol. 200, no. 1-3, pp. 1–23, 1999.

[55] E. Dagotto, T. Hotta, and A. Moreo, "Colossal magnetoresistant materials: the key role of phase separation," *Physics Reports*, vol. 344, no. 1-3, pp. 1–153, 2001.

[56] A. Tebano, C. Aruta, S. Sanna, P. G. Medaglia, G. Balestrino, A. A. Sidorenko, R. de Renzi, G. Ghiringhelli, L. Braicovich, V. Bisogni, and N. B. Brookes, "Evidence of orbital reconstruction at interfaces in ultrathin $La_{0.67}Sr_{0.33}MnO_3$ films," *Physical review letters*, vol. 100, no. 13, p. 137401, 2008.

[57] B. R. K. Nanda and S. Satpathy, "Effects of strain on orbital ordering and magnetism at perovskite oxide interfaces: $LaMnO_3/SrMnO_3$," *Physical Review B*, vol. 78, no. 5, 2008.

[58] C. Kwon, M. C. Robson, K.-C. Kim, J. Y. Gu, S. E. Lofland, S. M. Bhagat, Z. Trajanovic, M. Rajeswari, T. Venkatesan, A. R. Kratz, R. D. Gomez, and R. Ramesh, "Stress-induced effects in epitaxial $(La_{0.7}Sr_{0.3})MnO_3$ films," *Journal of Magnetism and Magnetic Materials*, vol. 172, no. 3, pp. 229–236, 1997.

[59] K. Steenbeck, T. Habisreuther, C. Dubourdieu, and J. P. Sénateur, "Magnetic anisotropy of ferromagnetic $La_{0.7}Sr_{0.3}MnO_3$ epitaxial thin films: Dependence on temperature and film thickness," *Applied Physics Letters*, vol. 80, no. 18, pp. 3361–3363, 2002.

[60] Z. Xiao, F. Zhang, M. A. Farrukh, R. Wang, G. Zhou, Z. Quan, and X. Xu, "Perpendicular magnetic anisotropy in compressive strained $La_{0.67}Sr_{0.33}MnO_3$ films," *Journal of Materials Science*, vol. 54, no. 12, pp. 9017–9024, 2019.

[61] M. Mathews, F. M. Postma, J. C. Lodder, R. Jansen, G. Rijnders, and D. H. A. Blank, "Step-induced uniaxial magnetic anisotropy of $La_{:67}Sr_{:33}MnO_3$ thin films," *Applied Physics Letters*, vol. 87, no. 24, 2005.

[62] B. Zhang, L. Wu, J. Zheng, P. Yang, X. Yu, J. Ding, S. M. Heald, R. A. Rosenberg, T. V. Venkatesan, J. Chen, C.-J. Sun, Y. Zhu, and G. M. Chow, "Control of magnetic anisotropy by orbital hybridization with charge transfer in $(La_{0.67}Sr_{0.33}MnO_3)_n/(SrTiO_3)_n$ superlattice," *NPG Asia Materials*, vol. 10, no. 9, pp. 931–942, 2018.

[63] J. Zhang, Z. Zhong, X. Guan, X. Shen, J. Zhang, F. Han, H. Zhang, H. Zhang, X. Yan, Q. Zhang, L. Gu, F. Hu, R. Yu, B. Shen, and J. Sun, "Symmetry mismatch-driven perpendicular magnetic anisotropy for perovskite/brown-

millerite heterostructures," *Nature communications*, vol. 9, no. 1, p. 1923, 2018.

[64] Z.-H. Wang, G. Cristiani, H.-U. Habermeier, Z.-R. Zhang, and B.-S. Han, "Perpendicular magnetic anisotropy of $La_{0.67}Sr_{0.33}MnO_3$ thin films grown on $CaMnO_3$ buffered $SrTiO_3$," *Journal of Applied Physics*, vol. 94, no. 8, pp. 5417–5419, 2003.

[65] F. Magnus, M. E. Brooks-Bartlett, R. Moubah, R. A. Procter, G. Andersson, T. P. A. Hase, S. T. Banks, and B. Hjörvarsson, "Long-range magnetic interactions and proximity effects in an amorphous exchange-spring magnet," *Nature communications*, vol. 7, p. ncomms11931, 2016.

[66] J. P. Liu, ed., *Nanoscale magnetic materials and applications*. Dordrecht and Heidelberg: Springer, 2009.

[67] H. Y. Hwang, Y. Iwasa, M. Kawasaki, B. Keimer, N. Nagaosa, and Y. Tokura, "Emergent phenomena at oxide interfaces," *Nature materials*, vol. 11, no. 2, pp. 103–113, 2012.

[68] F. Hellman, A. Hoffmann, Y. Tserkovnyak, G. S. D. Beach, E. E. Fullerton, C. Leighton, A. H. MacDonald, D. C. Ralph, D. A. Arena, H. A. Dürr, P. Fischer, J. Grollier, J. P. Heremans, T. Jungwirth, A. V. Kimel, B. Koopmans, I. N. Krivorotov, S. J. May, A. K. Petford-Long, J. M. Rondinelli, N. Samarth, I. K. Schuller, A. N. Slavin, M. D. Stiles, O. Tchernyshyov, A. Thiaville, and B. L. Zink, "Interface-Induced Phenomena in Magnetism," *Reviews of modern physics*, vol. 89, no. 2, 2017.

[69] V. Moshnyaga and K. Samwer, "Polaronic Emergent Phases in Manganite-based Heterostructures," *Crystals*, vol. 9, no. 10, p. 489, 2019.

[70] A. Wüchner, J. Voiron, J. C. Toussaint, and J. J. Préjean, "Observation and computer simulation of magnetization processes in exchange-coupled Sm/Co - Zr/SmCo' sandwiches," *Journal of Magnetism and Magnetic Materials*, vol. 148, no. 1-2, pp. 264–266, 1995.

[71] E. E. Fullerton, J. Jiang, and S. Bader, "Hard/soft magnetic heterostructures: model exchange-spring magnets," *Journal of Magnetism and Magnetic Materials*, vol. 200, no. 1-3, pp. 392–404, 1999.

[72] K. A. Thórarinsdóttir, T. Hase, B. Hjörvarsson, and F. Magnus, "Amorphous exchange-spring magnets with crossed perpendicular and in-plane anisotropies," *Physical Review B*, vol. 103, no. 1, 2021.

[73] W. Demtröder, *Experimentalphysik 1*. Berlin, Heidelberg: Springer Berlin Heidelberg, 2018.

[74] J.-B.-J. Fourier, *Théorie analytique de la chaleur*. Cambridge library collection. Mathematics, Cambridge: Cambridge University Press, 2009.

[75] T. M. Tritt, *Thermal Conductivity*. Springer US, 2004.

[76] U. Grigull and H. Sandner, *Heat conduction*. International series in heat and mass transfer, Berlin and Heidelberg: Springer, 1984.

[77] D. Sundararajan, *Fourier Analysis - A Signal Processing Approach*. Springer eBook Collection Computer Science, Singapore: Springer, 2018.

[78] Y. S. Touloukian and Roger W. Powell and C. Y. Ho and Michael Nicolaou, *Thermophysical properties of matter - the TPRC data series. Volume 10. Thermal diffusivity. (Reannouncement). Data book*, vol. Vol. 10 of *Thermophysical properties of matter*. New York, NY: IFI/Plenum, 1973.

[79] R. Franz and G. Wiedemann, "Ueber die Wärme-Leitungsfähigkeit der Metalle," *Annalen der Physik und Chemie*, vol. 165, no. 8, pp. 497–531, 1853.

[80] D. G. Cahill, H. E. Fischer, T. Klitsner, E. T. Swartz, and R. O. Pohl, "Thermal conductivity of thin films: Measurements and understanding," *Journal of Vacuum Science & Technology A: Vacuum, Surfaces, and Films*, vol. 7, no. 3, pp. 1259–1266, 1989.

[81] D. G. Cahill, "Thermal conductivity measurement from 30 to 750 K: the 3ω method," *Review of Scientific Instruments*, vol. 61, no. 2, pp. 802–808, 1990.

[82] C. Dames, "MEASURING THE THERMAL CONDUCTIVITY OF THIN FILMS: 3 OMEGA AND RELATED ELECTROTHERMAL METHODS," *Annual Review of Heat Transfer*, vol. 16, no. 1, pp. 7–49, 2013.

[83] S. N. Schiffres and J. A. Malen, "Improved 3-omega measurement of thermal conductivity in liquid, gases, and powders using a metal-coated optical fiber," *Review of Scientific Instruments*, vol. 82, no. 6, p. 064903, 2011.

[84] Cahill and Pohl, "Thermal conductivity of amorphous solids above the plateau," *Physical review. B, Condensed matter*, vol. 35, no. 8, pp. 4067–4073, 1987.

[85] D. G. Cahill, M. Katiyar, and Abelson, "Thermal conductivity of a-Si:H thin films," *Physical review. B, Condensed matter*, vol. 50, no. 9, pp. 6077–6081, 1994.

[86] D. G. Cahill, W. K. Ford, K. E. Goodson, G. D. Mahan, A. Majumdar, H. J. Maris, R. Merlin, and S. R. Phillpot, "Nanoscale thermal transport," *Journal of Applied Physics*, vol. 93, no. 2, pp. 793–818, 2003.

[87] J. Paterson, D. Singhal, D. Tainoff, J. Richard, and O. Bourgeois, "Thermal conductivity and thermal boundary resistance of amorphous Al_2O_3 thin films on germanium and sapphire," *Journal of Applied Physics*, vol. 127, no. 24, p. 245105, 2020.

[88] R. G. Bhardwaj and N. Khare, "Review: 3-omega Technique for Thermal Conductivity Measurement-Contemporary and Advancement in Its Methodology," *International Journal of Thermophysics*, vol. 43, no. 9, 2022.

[89] C. Clausen, T. Pedersen, and A. Bentien, "The 3-Omega Method for the Measurement of Fouling Thickness, the Liquid Flow Rate, and Surface Contact," *Sensors (Basel, Switzerland)*, vol. 17, no. 3, 2017.

[90] C. Dames and G. Chen, "1ω, 2ω, and 3ω methods for measurements of thermal properties," *Review of Scientific Instruments*, vol. 76, no. 12, p. 124902, 2005.

[91] T. Borca-Tasciuc, A. R. Kumar, and G. Chen, "Data reduction in 3ω method for thin-film thermal conductivity determination," *Review of Scientific Instruments*, vol. 72, no. 4, pp. 2139–2147, 2001.

[92] B. W. Olson, S. Graham, and K. Chen, "A practical extension of the 3ω method to multilayer structures," *Review of Scientific Instruments*, vol. 76, no. 5, 2005.

[93] M. Jungbauer, S. Hühn, R. Egoavil, H. Tan, J. Verbeeck, G. van Tendeloo, and V. Moshnyaga, "Atomic layer epitaxy of Ruddlesden-Popper $SrO(SrTiO_3)_n$ films by means of metalorganic aerosol deposition," *Applied Physics Letters*, vol. 105, no. 25, p. 251603, 2014.

[94] V. Moshnyaga, I. Khoroshun, A. Sidorenko, P. Petrenko, A. Weidinger, M. Zeitler, B. Rauschenbach, R. Tidecks, and K. Samwer, "Preparation of rare-earth manganite-oxide thin films by metalorganic aerosol deposition technique," *Applied Physics Letters*, vol. 74, no. 19, pp. 2842–2844, 1999.

[95] S. Merten, V. Roddatis, and V. Moshnyaga, "Metalorganic-aerosol-deposited Au nanoparticles for the characterization of ultrathin films by surface-enhanced Raman spectroscopy," *Applied Physics Letters*, vol. 115, no. 15, 2019.

[96] A. Belenchuk, O. Shapoval, V. Roddatis, V. Bruchmann-Bamberg, K. Samwer, and V. Moshnyaga, "Ruddlesden-Popper interface in correlated manganite heterostructures induces magnetic decoupling and dead layer reduction," *Applied Physics Letters*, vol. 109, no. 23, 2016.

[97] Z. Cui, ed., *Nanofabrication: Principles, Capabilities and Limits*. Boston, MA: Springer US, 2008 ed., 2009.

[98] J. Brentano, "Focussing method of crystal powder analysis by X-rays," *Proceedings of the Physical Society of London*, vol. 37, no. 1, pp. 184–193, 1924.

[99] H. Kiessig, "Interferenz von Röntgenstrahlen an dünnen Schichten," *Annalen der Physik und Chemie*, vol. 402, no. 7, pp. 769–788, 1931.

[100] A. Glavic and M. Björck, "GenX 3: the latest generation of an established tool," *Journal of applied crystallography*, vol. 55, no. Pt 4, pp. 1063–1071, 2022.

[101] L. G. Parratt, "Surface Studies of Solids by Total Reflection of X-Rays," *Physical Review*, vol. 95, no. 2, pp. 359–369, 1954.

[102] R. Storn, "On the usage of differential evolution for function optimization," in *Proceedings of North American Fuzzy Information Processing*, pp. 519–523, IEEE, 1996.

[103] R. Storn and K. Price, "Differential Evolution - A Simple and Efficient Heuristic for global Optimization over Continuous Spaces," *Journal of Global Optimization*, vol. 11, no. 4, pp. 341–359, 1997.

[104] C. Suryanarayana, *X-Ray Diffraction: A Practical Approach*. New York, NY: Springer, 1st ed. ed., 1998.

[105] W. Demtröder, *Experimentalphysik 3*. Berlin, Heidelberg: Springer Berlin Heidelberg, 2016.

[106] R. Doering, ed., *Handbook of semiconductor manufacturing technology*. Boca Raton: CRC Press, 2. ed. ed., 2008.

[107] V. Martelli, J. L. Jiménez, M. Continentino, E. Baggio-Saitovitch, and K. Behnia, "Thermal Transport and Phonon Hydrodynamics in Strontium Titanate," *Physical review letters*, vol. 120, no. 12, p. 125901, 2018.

[108] F. El-Mellouhi, E. N. Brothers, M. J. Lucero, and G. E. Scuseria, "Modeling of the cubic and antiferrodistortive phases of $SrTiO_3$ with screened hybrid density functional theory," *Physical Review B*, vol. 84, no. 11, 2011.

[109] A. M. Hofmeister, "Thermal diffusivity and thermal conductivity of single-crystal MgO and $Al2O_3$ and related compounds as a function of temperature," *Physics and Chemistry of Minerals*, vol. 41, no. 5, pp. 361–371, 2014.

[110] E. Langenberg, E. Ferreiro-Vila, V. Leborán, A. O. Fumega, V. Pardo, and F. Rivadulla, "Analysis of the temperature dependence of the thermal conductivity of insulating single crystal oxides," *APL Materials*, vol. 4, no. 10, p. 104815, 2016.

[111] S.-M. Lee, W. Choi, J. Kim, T. Kim, J. Lee, S. Y. Im, J. Y. Kwon, S. Seo, M. Shin, and S. E. Moon, "Thermal Conductivity and Thermal Boundary

Resistances of ALD Al_2O_3 Films on Si and Sapphire," *International Journal of Thermophysics*, vol. 38, no. 12, 2017.

[112] P. Henning, R. Gruhl, U. Ross, V. Roddatis, V. Bruchmann-Bamberg, K. P. Stroh, M. Seibt, P. Gegenwart, and V. Moshnyaga, "Tailoring of magnetism & electron transport of manganate thin films by controlling the Mn-O-Mn bond angles via strain engineering," *Scientific reports*, vol. 14, no. 1, p. 3253, 2024.

[113] H. Fujishiro, M. Ikebe, T. Kikuchi, and H. Ozawa, "First-order-like ferromagnetic transition in $(La_{1-y}Pr_y)_{1-x}(Ca_{1-z}Sr_z)_xMnO_3$ (x∼0.25)," *Physica B: Condensed Matter*, vol. 281-282, pp. 491–493, 2000.

[114] M. Uehara, S. Mori, C. H. Chen, and S.-W. Cheong, "Percolative phase separation underlies colossal magnetoresistance in mixed-valent manganites," *Nature*, vol. 399, no. 6736, pp. 560–563, 1999.

[115] D. W. Visser, A. P. Ramirez, and M. A. Subramanian, "Thermal Conductivity of Manganite Perovskites: Colossal Magnetoresistance as a Lattice-Dynamics Transition," *Physical review letters*, vol. 78, no. 20, pp. 3947–3950, 1997.

[116] A. M. Aliev, S. B. Abdulvagidov, A. B. Batdalov, I. K. Kamilov, O. Y. Gorbenko, V. A. Amelichev, A. R. Kaul', A. I. Kurbakov, and V. A. Trunov, "Effect of a magnetic field on the thermal and kinetic properties of the $Sm_{0.55}Sr_{0.45}MnO_{3.02}$ manganite," *Physics of the Solid State*, vol. 45, no. 1, pp. 130–137, 2003.

[117] A. V. Inyushkin, A. N. Taldenkov, O. Y. Gorbenko, and A. R. Kaul', "Thermal conductivity of $(La_{0.25}Pr_{0.75})_{0.7}Ca_{0.3}MnO_3$ under giant isotope effect conditions," *Journal of Experimental and Theoretical Physics Letters*, vol. 73, no. 11, pp. 609–613, 2001.

[118] J. L. Cohn, J. J. Neumeier, C. P. Popoviciu, K. J. McClellan, and T. Leventouri, "Local lattice distortions and thermal transport in perovskite manganites," *Physical Review B*, vol. 56, no. 14, pp. R8495–R8498, 1997.

[119] P. G. Radaelli, G. Iannone, M. Marezio, H. Y. Hwang, S.-W. Cheong, J. D. Jorgensen, and D. N. Argyriou, "Structural effects on the magnetic and

transport properties of perovskite $A_{1-x}A_x$'MnO_3 (x=0.25, 0.30)," *Physical review. B, Condensed matter*, vol. 56, no. 13, pp. 8265–8276, 1997.

[120] A. O. Fumega, Y. Fu, V. Pardo, and D. J. Singh, "Understanding the lattice thermal conductivity of $SrTiO_3$ from an ab initio perspective," *Physical Review Materials*, vol. 4, no. 3, 2020.

[121] F. Lan, H. Chen, H. Lin, Y. Bai, Y. Yu, T. Miao, Y. Zhu, T. Z. Ward, Z. Gai, W. Wang, L. Yin, E. W. Plummer, and J. Shen, "Observing a previously hidden structural-phase transition onset through heteroepitaxial cap response," *Proceedings of the National Academy of Sciences*, vol. 116, no. 10, pp. 4141–4146, 2019.

[122] S.-M. Lee and D. G. Cahill, "Heat transport in thin dielectric films," *Journal of Applied Physics*, vol. 81, no. 6, pp. 2590–2595, 1997.

[123] A. D. McConnell and K. E. Goodson, "THERMAL CONDUCTION IN SILICON MICRO- AND NANOSTRUCTURES," *Annual Review of Heat Transfer*, vol. 14, no. 14, pp. 129–168, 2005.

[124] K. H. Kim, M. Uehara, C. Hess, P. A. Sharma, and S. W. Cheong, "Thermal and electronic transport properties and two-phase mixtures in $La_{5/8-x}Pr_xCa_{3/8}MnO_3$," *Physical review letters*, vol. 84, no. 13, pp. 2961–2964, 2000.

[125] J. Kondo, "Resistance Minimum in Dilute Magnetic Alloys," *Progress of Theoretical Physics*, vol. 32, no. 1, pp. 37–49, 1964.

[126] J. P. Franck, F. D. Manchester, and Douglas L. Martin, "The specific heat of pure copper and of some dilute copper + iron alloys showing a minimum in the electrical resistance at low temperatures," *Proceedings of the Royal Society of London. Series A - Mathematical and Physical Sciences*, vol. 263, no. 1315, pp. 494–507, 1961.

[127] R. L. Rusby and B. R. Coles, "Resistance minima in (V-Cr)Fe alloys," *Journal of Physics F: Metal Physics*, vol. 4, no. 6, pp. L161–L166, 1974.

[128] E. T. Swartz and R. O. Pohl, "Thermal boundary resistance," *Reviews of Modern Physics*, vol. 61, no. 3, pp. 605–668, 1989.

[129] P. C. Michael, J. U. Trefny, and B. Yarar, "Thermal transport properties of single crystal lanthanum aluminate," *Journal of Applied Physics*, vol. 72, no. 1, pp. 107–109, 1992.

[130] J. Sun, Y. Li, Y. Karaaslan, C. Sevik, and Y. Chen, "Misfit dislocation structure and thermal boundary conductance of GaN/AlN interfaces," *Journal of Applied Physics*, vol. 130, no. 3, 2021.

[131] J. L. Cohn *Journal of Superconductivity: Incorporating Novel Magnetism*, vol. 13, no. 2, pp. 291–304, 2000.

[132] B. Chen, A. G. Rojo, C. Uher, H. L. Ju, and R. L. Greene, "Magnetothermal conductivity of $La_{0.8}Ca_{0.2}MnO_3$," *Physical review. B, Condensed matter*, vol. 55, no. 23, pp. 15471–15474, 1997.

[133] F. Rivadulla, E. Winkler, J.-S. Zhou, and J. B. Goodenough, "Phase competition in $L_{0.5}A_{0.5}MnO_3$ perovskites," *Physical review. B, Condensed matter*, vol. 66, no. 17, 2002.

[134] S. Merten, O. Shapoval, B. Damaschke, K. Samwer, and V. Moshnyaga, "Magnetic-Field-Induced Suppression of Jahn-Teller Phonon Bands in $(La_{0.6}Pr_{0.4})_{0.7}Ca_{0.3}MnO_3$: the Mechanism of Colossal Magnetoresistance shown by Raman Spectroscopy," *Scientific reports*, vol. 9, no. 1, p. 2387, 2019.

[135] V. Bruchmann-Bamberg, I. Weimer, V. Roddatis, U. Ross, L. Schüler, K. P. Stroh, and V. Moshnyaga, "Magnetism and Thermal Transport of Exchange-Spring-Coupled $La_{2/3}Sr_{1/3}MnO_3/La_2MnCoO_6$ Superlattices with Perpendicular Magnetic Anisotropy," *Nanomaterials (Basel, Switzerland)*, vol. 13, no. 21, 2023.

[136] M. B. Salamon and M. Jaime, "The physics of manganites: Structure and transport," *Reviews of Modern Physics*, vol. 73, no. 3, pp. 583–628, 2001.

[137] N. V. Volkov, "Spintronics: manganite-based magnetic tunnel structures," *Physics-Uspekhi*, vol. 55, no. 3, pp. 250–269, 2012.

[138] D. I. Khomskii, "Multiferroics: Different ways to combine magnetism and ferroelectricity," *Journal of Magnetism and Magnetic Materials*, vol. 306, no. 1, pp. 1–8, 2006.

[139] M. Zhang, G. Jeerh, P. Zou, R. Lan, M. Wang, H. Wang, and S. Tao, "Recent development of perovskite oxide-based electrocatalysts and their applications in low to intermediate temperature electrochemical devices," *Materials Today*, vol. 49, pp. 351–377, 2021.

[140] S. Ghosh, H. Shankar, and P. Kar, "Recent developments of lead-free halide double perovskites: a new superstar in the optoelectronic field," *Materials Advances*, vol. 3, no. 9, pp. 3742–3765, 2022.

[141] H. Wang, W. Su, J. Liu, and C. Wang, "Recent development of n-type perovskite thermoelectrics," *Journal of Materiomics*, vol. 2, no. 3, pp. 225–236, 2016.

[142] A. Berger, N. Supper, Y. Ikeda, B. Lengsfield, A. Moser, and E. E. Fullerton, "Improved media performance in optimally coupled exchange spring layer media," *Applied Physics Letters*, vol. 93, no. 12, 2008.

[143] J. Jiang and S. Bader, "Magnetic reversal in thin film exchange-spring magnets," *Scripta Materialia*, vol. 47, no. 8, pp. 563–568, 2002.

[144] S. Das, A. D. Rata, I. V. Maznichenko, S. Agrestini, E. Pippel, N. Gauquelin, J. Verbeeck, K. Chen, S. M. Valvidares, H. Babu Vasili, J. Herrero-Martin, E. Pellegrin, K. Nenkov, A. Herklotz, A. Ernst, I. Mertig, Z. Hu, and K. Dörr, "Low-field switching of noncollinear spin texture at $La_{0.7}Sr_{0.3}MnO_3$-$SrRuO_3$ interfaces," *Physical Review B*, vol. 99, no. 2, 2019.

[145] K. Mibu, T. Nagahama, T. Shinjo, and T. Ono, "Magnetoresistance of Bloch-wall-type magnetic structures induced in NiFe/CoSm exchange-spring bilayers," *Physical review. B, Condensed matter*, vol. 58, no. 10, pp. 6442–6446, 1998.

[146] R. Revathy, N. Kalarikkal, M. R. Varma, and K. P. Surendran, "Exchange-spring mechanism and Griffiths-like phase in room-temperature magnetoelectric Ni–$BaTiO_3$ composites," *Materials Advances*, vol. 2, no. 14, pp. 4702–4720, 2021.

[147] G. Orfila, D. Sanchez-Manzano, A. Arora, F. Cuellar, S. Ruiz-Gómez, S. Rodriguez-Corvillo, S. López, A. Peralta, S. J. Carreira, F. Gallego, J. Tornos, V. Rouco, J. J. Riquelme, C. Munuera, F. J. Mompean, M. Garcia-Hernandez, Z. Sefrioui, J. E. Villegas, L. Perez, A. Rivera-Calzada, C. Leon, S. Valencia, and J. Santamaria, "Large Magnetoresistance of Isolated Domain Walls in $La_{2/3}Sr_{1/3}MnO_3$ Nanowires," *Advanced materials (Deerfield Beach, Fla.)*, vol. 35, no. 33, p. e2211176, 2023.

[148] M. Thesberg, H. Kosina, and N. Neophytou, "On the Lorenz number of multiband materials," *Physical Review B*, vol. 95, no. 12, 2017.

[149] D. V. Maheswar Repaka and R. Mahendiran, "Giant magnetothermopower in charge ordered $Nd_{0.75}Na_{0.25}MnO_3$," *Applied Physics Letters*, vol. 103, no. 16, 2013.

[150] J. Kimling, K. Nielsch, K. Rott, and G. Reiss, "Field-dependent thermal conductivity and Lorenz number in Co/Cu multilayers," *Physical Review B*, vol. 87, no. 13, 2013.

[151] C. Euler, P. Hołuj, A. Talkenberger, and G. Jakob, "Magnetic field dependent thermal conductance in $La_{0.67}Ca_{0.33}MnO_3$," *Journal of Magnetism and Magnetic Materials*, vol. 381, pp. 188–193, 2015.

[152] R. Das, A. Chanda, and R. Mahendiran, "Influence of magnetic field on electrical and thermal transport in the hole doped ferromagnetic manganite: $La_{0.9}Na_{0.1}MnO_3$," *RSC advances*, vol. 9, no. 3, pp. 1726–1733, 2019.

[153] A. Ray and T. Dey, "Thermal conductivity of $La_{0.67}(Ca_xSr_{1-x})_{0.33}MnO_3$ (x=0, 0.5, 1) and $La_{0.6}Y_{0.07}Ca_{0.33}MnO_3$ pellets between 10 and 300K," *Solid State Communications*, vol. 126, no. 3, pp. 147–152, 2003.

[154] M. Kawasaki, K. Takahashi, T. Maeda, R. Tsuchiya, M. Shinohara, O. Ishiyama, T. Yonezawa, M. Yoshimoto, and H. Koinuma, "Atomic Control of the $SrTiO_3$ Crystal Surface," *Science (New York, N.Y.)*, vol. 266, no. 5190, pp. 1540–1542, 1994.

[155] M. Nord, P. E. Vullum, I. MacLaren, T. Tybell, and R. Holmestad, "Atomap: a new software tool for the automated analysis of atomic resolution images

using two-dimensional Gaussian fitting," *Advanced structural and chemical imaging*, vol. 3, no. 1, p. 9, 2017.

[156] J. Hemberger, A. Krimmel, T. Kurz, H.-A. Krug von Nidda, V. Y. Ivanov, A. A. Mukhin, A. M. Balbashov, and A. Loidl, "Structural, magnetic, and electrical properties of single-crystalline $La_{1-x}Sr_xMnO_3$ (0.4<x<0.85)," *Physical review. B, Condensed matter*, vol. 66, no. 9, 2002.

[157] J.-H. Park, E. Vescovo, H.-J. Kim, C. Kwon, R. Ramesh, and T. Venkatesan, "Direct evidence for a half-metallic ferromagnet," *Nature*, vol. 392, no. 6678, pp. 794–796, 1998.

[158] M. Keunecke, F. Lyzwa, D. Schwarzbach, V. Roddatis, N. Gauquelin, K. Müller-Caspary, J. Verbeeck, S. J. Callori, F. Klose, M. Jungbauer, and V. Moshnyaga, "High-T_C Interfacial Ferromagnetism in $SrMnO_3$/$LaMnO_3$ Superlattices," *Advanced Functional Materials*, p. 1808270, 2019.

[159] C. Meyer, V. Roddatis, P. Ksoll, B. Damaschke, and V. Moshnyaga, "Structure, magnetism, and spin-phonon coupling in heteroepitaxial La_2CoMnO_6/Al_2O_3(0001) films," *Physical Review B*, vol. 98, no. 13, 2018.

[160] R. Galceran, C. Frontera, L. Balcells, J. Cisneros-Fernández, L. López-Mir, J. Roqueta, J. Santiso, N. Bagués, B. Bozzo, A. Pomar, F. Sandiumenge, and B. Martínez, "Engineering the microstructure and magnetism of $La_2CoMnO_{6-\delta}$ thin films by tailoring oxygen stoichiometry," *Applied Physics Letters*, vol. 105, no. 24, 2014.

[161] H. Wang, J. Gazquez, C. Frontera, M. F. Chisholm, A. Pomar, B. Martinez, and N. Mestres, "Spontaneous cationic ordering in chemical-solution-grown La_2CoMnO_6 double perovskite thin films," *NPG Asia Materials*, vol. 11, no. 1, pp. 1–8.

[162] H. Boschker, J. Verbeeck, R. Egoavil, S. Bals, G. van Tendeloo, M. Huijben, E. P. Houwman, G. Koster, D. H. A. Blank, and G. Rijnders, "Preventing the Reconstruction of the Polar Discontinuity at Oxide Heterointerfaces," *Advanced Functional Materials*, vol. 22, no. 11, pp. 2235–2240, 2012.

[163] L. Chen, Z. Wang, G. Wang, H. Guo, M. Saghayezhian, Z. Liao, Y. Zhu, E. W. Plummer, and J. Zhang, "Surface and interface properties of $La_{2/3}Sr_{1/3}MnO_3$ thin films on $SrTiO_3(001)$," *Physical Review Materials*, vol. 3, no. 4, 2019.

[164] E. Granado, A. García, J. A. Sanjurjo, C. Rettori, I. Torriani, F. Prado, R. D. Sánchez, A. Caneiro, and S. B. Oseroff, "Magnetic ordering effects in the Raman spectra of $La_{1-x}Mn_{1-x}O_3$," *Physical review. B, Condensed matter*, vol. 60, no. 17, pp. 11879–11882, 1999.

[165] Z. Liao, F. Li, P. Gao, L. Li, J. Guo, X. Pan, R. Jin, E. W. Plummer, and J. Zhang, "Origin of the metal-insulator transition in ultrathin films of $La_{2/3}Sr_{1/3}MnO_3$," *Physical Review B*, vol. 92, no. 12, 2015.

[166] Q. G. Zhang, B. Y. Cao, X. Zhang, M. Fujii, and K. Takahashi, "Influence of grain boundary scattering on the electrical and thermal conductivities of polycrystalline gold nanofilms," *Physical Review B*, vol. 74, no. 13, 2006.

[167] R. Mandal, M. Chandra, V. Roddatis, P. Ksoll, M. Tripathi, R. Rawat, R. J. Choudhary, and V. Moshnyaga, "Magneto-dielectric effect in relaxor superparaelectric Tb_2CoMnO_6 film," *Physical Review B*, vol. 101, no. 9, 2020.

[168] A. Bhui, T. Ghosh, K. Pal, K. Singh Rana, K. Kundu, A. Soni, and K. Biswas, "Intrinsically Low Thermal Conductivity in the n-Type Vacancy-Ordered Double Perovskite Cs_2SnI_6: Octahedral Rotation and Anharmonic Rattling," *Chemistry of Materials*, vol. 34, no. 7, pp. 3301–3310, 2022.

[169] P. Acharyya, T. Ghosh, K. Pal, K. Kundu, K. Singh Rana, J. Pandey, A. Soni, U. V. Waghmare, and K. Biswas, "Intrinsically Ultralow Thermal Conductivity in Ruddlesden-Popper 2D Perovskite $Cs_2PbI_2Cl_2$: Localized Anharmonic Vibrations and Dynamic Octahedral Distortions," *Journal of the American Chemical Society*, vol. 142, no. 36, pp. 15595–15603, 2020.

[170] M. Jin, J. Liang, P. Qiu, H. Huang, Z. Yue, L. Zhou, R. Li, L. Chen, and X. Shi, "Investigation on Low-Temperature Thermoelectric Properties of Ag_2Se Polycrystal Fabricated by Using Zone-Melting Method," *The journal of physical chemistry letters*, vol. 12, no. 34, pp. 8246–8255, 2021.

[171] C. Seick, K. Stroh, T. Titze, V. Bruchmann-Bamberg, A. Weisser, S. Mathias, V. Moshnyaga, H. Ulrichs, and D. Steil, "Energy relaxation in $(La_{0.6}Pr_{0.4})_{0.7}Ca_{0.3}MnO_3$ films across the metal-insulator transition," *Physical Review B*, vol. 107, no. 8, 2023.

[172] P. Jha, T. D. Sands, L. Cassels, P. Jackson, T. Favaloro, B. Kirk, J. Zide, X. Xu, and A. Shakouri, "Cross-plane electronic and thermal transport properties of p-type $La_{0.67}Sr_{0.33}MnO_3/LaMnO_3$ perovskite oxide metal/semiconductor superlattices," *Journal of Applied Physics*, vol. 112, no. 6, 2012.

[173] P. Thiessen, V. Roddatis, F. Rieger, A. Belenchuk, M. Keunecke, V. Moshnyaga, and C. Jooss, "Effect of charge ordering on crossplane thermal conductivity in correlated perovskite oxide superlattices," *Physical Review B*, vol. 98, no. 19, 2018.

[174] D. Meyer, V. Roddatis, J. P. Bange, S. Lopatin, M. Keunecke, D. Metternich, U. Roß, I. V. Maznichenko, S. Ostanin, I. Mertig, V. Radisch, R. Egoavil, I. Lazić, V. Moshnyaga, and H. Ulrichs, "Atomic scale spectral control of thermal transport in phononic crystal superlattices," *arXiv:2009.14532*, DOI: 10.48550/arXiv.2009.14532, 2020.

[175] A. D. McConnell, S. Uma, and K. E. Goodson, "Thermal conductivity of doped polysilicon layers," *Journal of Microelectromechanical Systems*, vol. 10, no. 3, pp. 360–369, 2001.

[176] Y. Xiang and C. W. Chen, "Spatial distribution characteristics of magnetization in exchange-coupled bilayers with mutually orthogonal anisotropies," *Journal of Magnetism and Magnetic Materials*, vol. 430, pp. 1–5, 2017.

[177] A. Kumar, A. Kosonowski, P. Wyzga, and K. T. Wojciechowski, "Effective thermal conductivity of $SrBi_4Ti_4O_{15}$-$La_{0.7}Sr_{0.3}MnO_3$ oxide composite: Role of particle size and interface thermal resistance," *Journal of the European Ceramic Society*, vol. 41, no. 1, pp. 451–458, 2021.

[178] M. V. Simkin and G. D. Mahan, "Minimum thermal conductivity of superlattices," *Physical review letters*, vol. 84, no. 5, pp. 927–930, 2000.

[179] S. Y. Ren and J. D. Dow, "Thermal conductivity of superlattices," *Physical review. B, Condensed matter*, vol. 25, no. 6, pp. 3750–3755, 1982.

[180] D. Meyer, *Spektrale Kontrolle von elastischer Dynamik und Wärmetransport in periodischen Nanostrukturen.* Dissertation, DOI: 10.53846/goediss-8969, Georg August University of Goettingen, 2021.

[181] Z. Chen, W. Jang, W. Bao, C. N. Lau, and C. Dames, "Thermal contact resistance between graphene and silicon dioxide," *Applied Physics Letters*, vol. 95, no. 16, p. 161910, 2009.

[182] W. Ouyang, H. Qin, M. Urbakh, and O. Hod, "Controllable Thermal Conductivity in Twisted Homogeneous Interfaces of Graphene and Hexagonal Boron Nitride," *Nano letters*, vol. 20, no. 10, pp. 7513–7518, 2020.

[183] M. E. Chen, M. M. Rojo, F. Lian, J. Koeln, A. Sood, S. M. Bohaichuk, C. M. Neumann, S. G. Garrow, K. E. Goodson, A. G. Alleyne, and E. Pop, "Graphene-based electromechanical thermal switches," *2D Materials*, vol. 8, no. 3, p. 035055, 2021.

[184] A. A. Balandin, S. Ghosh, W. Bao, I. Calizo, D. Teweldebrhan, F. Miao, and C. N. Lau, "Superior thermal conductivity of single-layer graphene," *Nano letters*, vol. 8, no. 3, pp. 902–907, 2008.

[185] M. Balkanski, R. F. Wallis, and E. Haro, "Anharmonic effects in light scattering due to optical phonons in silicon," *Physical review. B, Condensed matter*, vol. 28, no. 4, pp. 1928–1934, 1983.

Acknowledgements

At this point I would like to take the opportunity to thank for all the help, no matter whether big or small, of all the people who contributed to the success and completion of this work and who accompanied me during my studies.

First of all, I thank my supervisor Prof. Dr. V. Moshnyaga for all the years of constructive and pragmatic help, all the ordinary and extraordinary manganite seminars and a steadily friendly atmosphere. You always treated science like a passion and taught us not to simply follow equations and recepies but to step out the borders and to think critically on our own.

I thank Prof. Dr. C. Jooß for being the second reviewer of this work and for organizing and leading numerous interesting and fruitful SFB events.

Many thanks to Prof. Dr. S. Mathias for belonging to my thesis advisory committee and for various discussions.

I would further like to give many thanks to the members of the examination board, Prof. Dr. H. C. Hofsäss, Prof. Dr. J. P. Palakkal, Prof. Dr. M. Seibt, and Dr. D. Steil, for critically reviewing this thesis and the defense.

The I. Physical Institute has some extraordinarily important members: Uta F., Carsten M., Hartmut E., Katrin G., Michaela M., Finn K. and Miriam M.-R. whom I must give my biggest respect and thanks, because they always keep the institute running like a Swiss clockwork. Further I thank all our outstanding technicians, Simon S., Kai D., Bastian B. and Florian F. for all the support and for helping us (students) with our everyday annoying simplest technical requests even though their capabilities could be used to build a fusion reactor. I further thank Serhij D. for all the expertise in SQUID and help with the fascinating chemistry.

V. Roddatis and U. Ross I thank for providing the beautiful atomic scale TEM insights in our condensed matter as nobody else could do it better.

Many thanks go to D. Wagner and J. Verhoeven from the electronics workshop and F. Rieger from AG Jooß for helping me with the 3ω basics and the electronics and ingeniously testing it on a light bulb.

I would like to thank the whole I. Physical Institute and especially the MAD group both present and retired, for the many years of a friendly and humorous atmosphere as well as all the fruitful discussions and nice retreats. Thanks to Philipp K. for everything, especially for making our group so exciting, Leonard S. for his nice Raman measurements and excellent pool shots, Pia H. for her nice work on buffer layers and the groovy chords and Tim T. for great reflectivity measurements and for catching the biggest fish I have ever seen. I thank Isabell W. for her excellent superlattices and all the precise revisions. Thanks a lot to Alex B. and Oleg S. for teaching me the alchemistry of the MAD. Many thanks to Marius K., Dennis M. and Karen S. for proofreading and for the nostalgic memories of our time at university. One special thank I owe to Karen S. who found path not only to our research group but also to my life, for brightening up both of them with warmth.

I gratefully acknowledge financial support of the German Research Foundation DFG within the CRC 1073 and the International Center for Advanced Studies of Energy Conversion ICASEC.

One big thanks goes to Ivan R., for being the best friend and for all the support from the very beginning.

Last but not least, I would like to give my biggest thanks to my family for all the help, support and encouragement, for both keeping company and leaving undisturbed when needed, as well as for being the best family I could possibly have.